BRNO UNIVERSITY OF TECHNOLOGY

VYSOKÉ UČENÍ TECHNICKÉ V BRNĚ

FACULTY OF MECHANICAL ENGINEERING

FAKULTA STROJNÍHO INŽENÝRSTVÍ

INSTITUTE OF AEROSPACE ENGINEERING

LETECKÝ ÚSTAV

TECHNOLOGIES FOR SAFE UAS OPERATIONS UNDER BAD WEATHER CONDITIONS

TECHNOLOGIE PRO BEZPEČNÝ PROVOZ BEZPILOTNÍCH PROSTŘEDKŮ ZA ZTÍŽENÝCH POVĚTRNOSTNÍCH PODMÍNEK

DOCTORAL THESIS

DIZERTAČNÍ PRÁCE

AUTHOR AUTOR PRÁCE	Ing. Renáta Balážová, MSc
SUPERVISOR ŠKOLITEL	doc. Ing. Jiří Hlinka, Ph.D.

BRNO 2024

Abstrakt

Táto dizertačná práca sa zaoberá problematikou bezpečnej prevádzky bezpilotných lietadiel (UAV) v náročných poveternostných podmienkach, najmä s ohľadom na turbulencie v nízkych výškach nad terénom. Práca sa zameriava na využitie metódy výpočtu miery rozptylu vírov (EDR) na detekciu turbulencií a navrhuje novú metodiku výpočtu EDR pre multikoptéry.

Súčasťou výskumu boli numerické simulácie v prostredí STAR-CCM+ a ENVI-met, ktoré umožnili identifikovať oblasti so zvýšeným výskytom turbulencií v okolí budov a prekážok. Na základe týchto simulácií boli odvodené empirické vzorce pre predikciu veľkosti nebezpečných zón pre prevádzku UAV.

Praktická časť práce zahŕňala testovacie lety s využitím UAV DJI M100 vybaveného ultrazvukovým anemometrom Calypso. Namerané údaje boli použité na validáciu numerických simulácií a taktiež výpočet EDR pomocou prispôsobenej metódy štruktúrnych funkcií.

Výsledky práce prispievajú k zlepšeniu bezpečnosti prevádzky UAV v náročných poveternostných podmienkach a ponúkajú nové možnosti pre ich využitie v rôznych oblastiach.

Kľúčové slová: bezpilotné lietadlo, turbulencie, nízke nadmorské výšky, meteorologické predpovede, bezpečnosť leteckej prevádzky, Eddy Dissipation Rate (EDR), numerické simulácie.

Abstract

This dissertation addresses the issue of safe operation of unmanned aerial vehicles (UAVs) in challenging weather conditions, particularly with respect to low-altitude turbulence. The work focuses on utilizing the Eddy Dissipation Rate (EDR) calculation method for turbulence detection and proposes a new methodology for calculating EDR for multicopters.

The research included numerical simulations in STAR-CCM+ and ENVI-met environments, which allowed for the identification of areas with increased turbulence occurrence near buildings and obstacles. Based on these simulations, empirical formulas were derived to predict the size of dangerous zones for UAV operation.

The experimental part of the research involved test flights using a DJI M100 UAV equipped with a Calypso ultrasonic anemometer. The measured data were used to validate the numerical simulations and also to calculate EDR using an adapted structural functions method.

The results of the work contribute to improving the safety of UAV operation in demanding weather conditions and offer new possibilities for their use in various areas.

Keywords: unmanned aerial vehicle, turbulence, low altitude, weather forecasting, aviation safety, Eddy Dissipation Rate (EDR), numerical simulations.

Bibliographic Citation

Citation of a printed work:

BALÁŽOVÁ, Renáta. *Technologie pro bezpečný provoz bezpilotních prostředků za ztížených povětrnostních podmínek.* Brno, 2025. Dostupné také z: https://www.vut.cz/studenti/zav-prace/detail/163116. Dizertační práce. Vysoké učení technické v Brně, Fakulta strojního inženýrství, Letecký ústav. Vedoucí práce Jiří Hlinka.

Citation of an electronic source:

BALÁŽOVÁ, Renáta. *Technologie pro bezpečný provoz bezpilotních prostředků za ztížených povětrnostních podmínek* [online]. Brno, 2025 [cit. 2024-09-17]. Dostupné z: https://www.vut.cz/studenti/zav-prace/detail/163116. Dizertační práce. Vysoké učení technické v Brně, Fakulta strojního inženýrství, Letecký ústav. Vedoucí práce Jiří Hlinka.

Declaration

I declare that I have independently written this doctoral thesis titled "TECHNOLOGIES FOR SAFE UAS OPERATIONS UNDER BAD WEATHER CONDITIONS" under the supervision of my university. I have exclusively used sources of information that are properly cited and listed in the comprehensive bibliography at the end of the thesis.

Brno, September 18th, 2024

Ing. Renáta Balážová, MSc

Acknowledgment

The path to this dissertation was not always smooth, but rather a winding journey with its share of challenges. Without the support and encouragement of those around me, reaching this destination would not have been possible.

I extend my deepest gratitude to my supervisor, Assoc. Prof. Hlinka, whose guidance and expertise were invaluable. You were like a beacon, guided me through the stormiest seas. Your unwavering support and insightful feedback illuminated my path and helped me navigate the complexities of this research. I am eternally grateful for your mentorship and the privilege of learning at your side.

Finally, I want to acknowledge my own perseverance and determination. Despite the obstacles, I never lost sight of the goal, and I am proud to have completed this dissertation.

Contents

1 INTRODUCTION 9
2 STATE OF THE ART 12
  2.1 HYPERLOCAL METEOROLOGICAL FORECASTS 12
  2.2 Deficiencies of current meteorological information for UAV operations 15
  2.3 DEMONSTRATION MISSION - RZESZOW 20
    2.3.1 Physical components used in conjunction with directly measured data 20
    2.3.2 Data acquisition approach 22
    2.3.3 Data exploitation methodology 23
    2.3.4 Deviations of measured metrological parameters at very low altitudes 24
  2.4 TURBULENCE 26
    2.4.1 Basic Classification of Turbulence Based on Origin 27
    2.4.2 Basic Classification of Turbulence Based on Intensity 28
    2.4.3 Limitations of PIREPs and the Rise of In-Situ Data in Aviation Meteorology 28
    2.4.4 The Eddy Dissipation Rate (EDR) Method 29
  2.5 Low-level turbulence (LLT) 34
    2.5.1 Technologies for Low-Altitude Turbulence Detection 34
    2.5.2 Previous Research on Low-Altitude Turbulence Detection Using UAVs 37
3 AIM AND OBJECTIVES 38
4 THEORY 40
  4.1 Eddy Dissipation Rate – Review 40
  4.2 NCAR algorithm not applicable for multicopters 41
  4.3 EDR calculation possibilities 41
    4.3.1 Fluctuating velocity gradients 41
    4.3.2 Smagorinsky closure method 43
    4.3.3 Dimensional analysis 44
    4.3.4 Structure function 47
    4.3.5 Energy spectrum 48
    4.3.6 Forced balance of the TKE equation 48
  4.4 Wind measurement techniques for multi-rotor UAV 49
5 EXPERIMENTAL WORK 56
  5.1 PRELIMINARY NUMERICAL SIMULATION STAR-CCM+ 56
    5.1.1 Initial results 61
  5.2 PRELIMINARY TEST FLIGHTS – BRNO 61

5.2.1 Indoor hover test ... 61
5.2.2 Outdoor hover test ... 65
5.2.3 Initial results ... 69
5.3 NUMERICAL SIMULATION – ENVI-met ... 70
5.3.1 Single building scenario ... 71
5.3.2 AdMaS centre scenario ... 76
5.3.3 Initial results ... 88
5.4 Hardware equipment ... 88
5.4.1 Sonic anemometer ... 89
5.4.2 UAV platform ... 91
5.4.3 Ground meteorological station ... 92
5.4.4 Initial results ... 94
5.5 DEMONSTRATION MISSION AdMaS ... 94
5.5.1 Location ... 94
5.5.2 Concept ... 95
5.5.3 Selection of test days and measurement details ... 96
5.5.4 Data Alignment for Comparative Analysis ... 97
5.5.5 Comparative Analysis of Wind Speed Real-Time Data ... 99
5.5.6 Comparison with numerical simulation ... 100
5.5.7 Initial results ... 103
5.6 EDR formula ... 104
5.6.1 EDR calculation ... 105
5.6.2 EDR results from AdMaS data ... 106
5.6.3 Initial result ... 109
6 SUMMARY OF RESULTS ... 110
6.1 NUMERICAL SIMULATION ... 110
6.2 DEMONSTRATION MISSION AdMaS ... 111
6.3 EDR calculation ... 111
6.4 Definition of Thesis Objectives ... 112
7 CONCLUSION ... 113

1 INTRODUCTION

The operation of Unmanned Aerial Systems (UAS) in airspace is rapidly increasing, and current analyses and forecasts [1],[2],[3] clearly indicate that this trend will continue in the next decade. In response to this growth, regulations are being gradually adjusted to allow wider access to airspace for unmanned aircraft [4],[5],[6]. It is imperative that the UAS system maintains a high level of safety during its expansion to realize its full potential. As always, weather poses a significant risk to all types of aviation.

Over time, meteorological services for manned aviation have evolved to meet user requirements in line with changing trends. The unique characteristics of UAS necessitate the improvement of current aviation meteorological services to provide UAV operators with the information necessary to ensure the required safety [7]. It is important to address the differences between unmanned and manned operations from the perspective of meteorological information requirements. A challenge for the UAS system is the update frequency of current weather forecasts and the flight levels for which these forecasts are provided [8]. Manned aviation weather forecasts are delivered hourly for high-altitude flight levels or for airport areas, which is irrelevant for UAV flights conducted at low altitudes near the Earth's surface and with short flight durations. The successful integration of UAS depends on the ability of future airspace management strategies to remain safe and efficient in various weather conditions.

Most UAVs fly at altitudes below 500 m. Aircraft at these low altitudes, including helicopters, require higher-resolution data than is currently available to avoid flying in isolated areas of fog, for example. It is also crucial to note that urban environments present additional challenges that need to be overcome. The atmospheric boundary layer at these altitudes is significantly influenced by local orography [9]. For instance, in urban environments with complex orography, atmospheric turbulence is characterized by strong spatial inhomogeneity due to the presence of buildings, parks, highways, etc., [10] resulting in very different weather conditions than those considered for traditional manned aviation.

Accurate, real-time knowledge of low-altitude weather information is limited, particularly in urban areas [11]. This limitation hinders the safe implementation of numerous anticipated UAV applications in urban areas, such as photography, mapping, inspection, and package delivery. Current numerical weather prediction models clearly cannot resolve the range of processes occurring in the urban landscape. The spatial and temporal resolution is too coarse.

Insufficient meteorological information for (unmanned) operations at low altitudes is the main topic of this dissertation. The preliminary analysis was oriented on verification of the quality of current weather forecasts for UAV use at low altitudes and to define the gap between existing information used in traditional manned aviation and the needs of the new unmanned aviation to support the safe operation of UAVs at very low levels (VLL), i.e., at altitudes not exceeding 150 meters above ground level in urban environments. To this end, comprehensive research has been conducted to identify gaps between existing aviation information and the meteorological information requirements of UAV operators. These identified shortcomings in meteorological information services for future UAV operations were crucial for achieving safe UAV operation in VLL airspace. Based on precisely identified shortcomings of current meteorological information services, a set of main problems were compiled.

The selected goal of this dissertation is atmospheric boundary layer, where most UAV operations occur and it is characterized by complex and dynamic wind patterns, including turbulence, which can pose significant risks to flight stability and control. The ability to accurately detect and predict turbulence is, therefore, paramount for ensuring the safety and reliability of UAV operations.

Traditional methods for turbulence detection, such as pilot reports (PIREPs) and ground-based remote sensing technologies like lidar, sodar, and radar, have inherent limitations in terms of spatial resolution, accuracy, and real-time applicability, especially in the context of low-altitude UAV flights. The emergence of UAVs as versatile sensor platforms has spurred the development of in-situ turbulence measurement techniques, offering the potential for high-resolution, real-time data acquisition. However, most existing research in this area has focused on high-cost [102],[109],[110], high-frequency sensors, which are often impractical for smaller UAVs due to weight and budget constraints.

This dissertation addresses the pressing need for accessible and cost-effective turbulence detection solutions for UAVs operating in the lower atmosphere. The research focuses on the Eddy Dissipation Rate (EDR), a key turbulence metric recognized by the International Civil Aviation Organization (ICAO) [13] and explores its estimation using a low-cost sonic anemometer integrated onto a UAV platform. The study encompasses a multi-faceted approach, combining sensor validation, numerical modelling, and real-world flight experiments to gain a comprehensive understanding of low-altitude turbulence and its implications for UAV operations.

The research began by validating the accuracy and precision of the selected low-cost sonic anemometer through wind tunnel testing. Subsequently, the sensor was integrated onto a UAV platform, and data logging procedures were established. The UAV was then deployed in a real-world urban environment, the AdMaS centre, to collect in-situ wind measurements in the vicinity of buildings. These measurements were complemented by data from a ground-based meteorological station, providing a reference for comparison and validation.

In parallel, numerical simulations were conducted using the ENVI-met software to model the wind flow patterns and turbulence distribution around buildings. These simulations served two primary purposes: to validate empirically derived formulas for predicting the size of hazardous zones near buildings and to generate a baseline model for comparison with the real-time turbulence data collected during the UAV flights.

The core of the research lies in the adaptation of the structure function method for EDR calculation, specifically tailored to the 1 Hz sampling rate of the low-cost sonic anemometer.

This adaptation enables the estimation of EDR from the UAV's in-situ measurements, providing real-time turbulence information during flight. The analysis of the collected data reveals valuable insights into the relationship between EDR, wind speed, and velocity fluctuations, challenging conventional assumptions and offering a more nuanced understanding of turbulence dynamics in the lower atmosphere.

The findings of this dissertation contribute to the development of practical and accessible turbulence detection solutions for UAVs, promoting safer and more efficient operations in challenging weather conditions. The integration of low-cost sensors, coupled with the adapted EDR calculation methodology and validated numerical models, empowers UAV operators with the tools and knowledge necessary to navigate complex urban environments and mitigate turbulence-related risks. This research paves the way for the seamless integration of UAVs into the airspace of the future, unlocking their full potential for a wide range of applications across various sectors.

2 STATE OF THE ART

2.1 HYPERLOCAL METEOROLOGICAL FORECASTS

Aviation meteorology

The Aviation Meteorological Service provides information about the meteorological phenomena, the state of the weather and its expected development, which are necessary for the safe and efficient operation flights. It is a branch of applied meteorology that specializes in phenomena, processes and meteorological elements that affect flight operations and aeronautical engineering.

The basic standard regarding aviation meteorology is ICAO Annex 3 "Meteorological Service for International Air Navigation" [12], and in the Czech Republic there is a regulation based on the ICAO standard called "L-3 Meteorology" [13]. The given standards and recommendations relate mainly to the following key areas:

- Meteorological observations
- Meteorological forecasts
- Meteorological warnings (for aircraft)
- Weather reports (from airplanes)
- Communication, collection, and distribution of information

The aviation meteorological service is provided within the Czech Republic by the Czech Hydrometeorological Institute, Department of Aviation Meteorology (OLM). OLM is a certified provider of meteorological information for civil aviation in accordance with Common requirements according to Regulation (EC) No. 550/2004 and Regulation (EC) 2096/2005 of the European Parliament and Council. OLM supplies information for civil aviation in accordance with Annex No. 3 to the Treaty on Civil Aviation (in the Czech language, the regulation of the Ministry of the Czech Republic L3-METEOROLOGY) and subsequent ICAO regulations and thus contributes to the safety, regularity and economy of air traffic.

The Department of Aviation Meteorology mainly provides for civil aviation:

- warning service for the LKAA flight area (Czech Republic)
- issues aeronautical meteorological reports METAR/SPECI and METREPORT/SPECIAL
- issues forecasts according to Chapter 6, Supplement 5 of the L3 regulation
- provides services for operators and flight crews according to Chapter 9, Supplement 8 of the L3 regulation (flight documentation, briefing and de-briefing, consultations and others)
- provides aeronautical climatological information according to Chapter 8, Appendix 7 of the L3 regulation

Collection of meteorological data and their subsequent distribution

The main task of aviation meteorology is the continuous monitoring of the weather at airports and in the relevant flight areas for the purpose of providing meteorological information to the users of the airspace. Standardized systems are used to provide meteorological information in air traffic. An important stage is the collection of measured meteorological data using terrestrial meteorological stations, radars, balloon probes and data from on-board meteorological stations. The more input data are grouped together, the more high-quality and accurate meteorological forecasts are obtained. A reduction in the frequency of air traffic, as happened for example during the Covid pandemic, causes a reduction in the quality of meteorological forecasts.

Based on measured meteorological data, regular and extraordinary weather reports, alerts and warnings are issued. Meteorological information is distributed through various communication channels in the format of graphic maps or text files. Aviation meteorology reports help air traffic control services and aircraft crews to obtain information about the current weather and its development in order to adapt the current/planned flight to the given conditions. In the Czech Republic, the publication of meteorological information is governed by the "L3 Meteorology" regulation [13], which is based on the international ICAO standard "Annex 3" [12].

OLM of the Czech Hydrometeorological Institute issues the following reports:

- **METAR** - Meteorological reports from weather stations operated by the Air Weather Service at airports with controlled air traffic. Meteorological information is presented in the form of a METAR code. METAR reports are issued at regular 1/2-hour intervals.
- **TAF** - Airport forecasts for airports with controlled air traffic. TAF airport forecasts are issued every 3 hours valid for 9 hours (or every 6 hours valid for 24 hours).
- **SIGMET** - is information on selected dangerous meteorological phenomena that can significantly affect the safety of air traffic. A SIGMET contains information on the occurrence or expected occurrence of thunderstorms (TS), severe turbulence (SEV TURB), severe icing (SEV ICE), significant (strong) wave flow behind orographic obstacles (SEV MTW), tropical cyclone (TC) or volcanic ash (VA) and others. SIGMET information is issued in the form of abbreviated open speech for relevant FIRs and for flights between FL100 and FL450. The validity period is max. 4 hours (up to 6 hours in the case of SIGMET information about VA).
- **AIRMET** - Information about dangerous weather phenomena on the route for flights at low levels.
- **GAMET** - regional forecast for flights at low altitudes (up to FL100) for individual FIRs. This report is issued 4 times a day, valid for 6 hours.

Meteorological forecasts

Obtained basic meteorological data from ground devices, on-board weather stations, satellites and other sources are grouped as input information needed for meteorological forecasting models. An integral part of the input data is also information about the surface of the earth (forest, desert, water surface) together with orographic information (mountains, lowlands). All of this information is input into a forecast model, which is software with a programmed set of equations that describe the behaviour of the Earth's atmosphere. The output of the forecast model is forecast grids with different resolutions, for example 3 x 3 km, where each point of the grid contains forecasted meteorological parameters (temperature, precipitation, humidity, wind speed and direction, cloudiness, and others). Aviation forecasting networks provide information for the land area as well as for altitude levels.

World meteorological centres issue global forecasts for the entire planet. The resolution of global forecasts is approximately 25 km. The outputs from these global models are inputs for local models that recalculate the global forecast and create networks with a more detailed resolution of, for example, 1 x 1 km. Therefore, forecasting is not only based on physical equations, but the outputs from the models are still statistically processed and improved. Currently, artificial intelligence is also used to improve forecasts.

2.2 Deficiencies of current meteorological information for UAV operations

As mentioned in the introductory part, several previous studies have been devoted to this issue, and the author's goal is to summarize them, which is devoted to subsection 2.2.

MIT Lincoln Laboratory Research: ATC-437 [11] developed a preliminary identification and assessment of current meteorological information gaps for UAS operations, conducted through surveys and interviews with more than 90 UAS operators, along with recommendations for improving the provision of weather information for UAS operations. In total, 12 major meteorological information gaps for UAS operators were identified and are listed in the following table.

Table 1: Prioritized ranking of Specific Weather Information Gaps [source: MIT Lincoln Laboratory, ATC-437, page 72]

	Weather Information Gap	***Impacted UAS Operation***
1.	Numerical weather model performance is uncertain, especially where there is a large variation in terrain.	All UAS missions, especially in the low-altitude domain
2.	No mechanism to alert operators to rapid changes in winds (e.g., due to microburst outflows, gust fronts and sharp synoptic fronts)	Primarily small UAS operations
3.	Off-airport weather observations (visibility, ceiling, wind) are sparse	All UAS missions that operate off-airport, especially VLOS operations (Part 107)
4.	Tactical convective weather products lack short-term storm forecasts and are susceptible to latencies	Primarily BVLOS missions for UAS without onboard weather radar
5.	Current wind aloft forecasts lack precision and winds aloft observations are lacking in the low-altitude and super high-altitude regions	Primarily BVLOS mission planning, especially for time-based operations
6.	Strategic convective weather products lack precision at long forecast horizons and need better uncertainty information to support decision making	Primarily BVLOS missions with durations greater than 2 hours
7.	Urban wind products are not sufficient and are not available to the public	All UAS missions in an urban environment
8.	Lack of validated stratospheric and low-altitude turbulence information	Very high-altitude missions / low-altitude missions in the boundary layer
9.	Icing and turbulence forecasts lack an uncertainty element to support contingency planning	Primarily BVLOS missions
10.	Icing models do not account for ‘cold soak’ effect	High-altitude BVLOS missions
11.	Turbulence and icing models not designed for small UAS	Primarily BVLOS missions with small UAS
12.	Weather impact models do not exist for UAS	Airspace management, including geofences, airspace capacity balancing, time-based ops

A key finding was that classic aerodrome weather observations and forecasts tailored for aerodrome operations are not sufficient for off-airdrome operations at low altitudes. Users in the survey said that airport weather information cannot be transferred to conditions at remote launch sites, which are affected by local orography - terrain, vegetation and water resources.

In addition, the survey results show that significantly less weather information is available for areas outside the airport zone at low altitude than for standard manned flights. The lack of observations (visibility, wind and other meteorological parameters) especially for areas of UAS operation at low altitudes makes the verification of numerical weather predictions for these locations a top priority. Warning of hazardous weather through convective activity and strong surface winds is a major problem for UAS operations (This problem could be partially addressed by providing UAS operators with access to existing FAA "Real-time conventional aircraft weather decision support products").

Based on the research "Preliminary Weather Information Gap Analysis for UAS Operations", a plan summarizing the development of the proposed research to fill the identified gaps was subsequently developed by the MIT Lincoln Laboratory “Preliminary UAS Weather Research Roadmap” [14]. The following table shows a list of 14 recommendations regarding current information gaps.

Table 2: List of Weather Research Recommendations to Address Information Gaps [source: MIT Lincoln Laboratory, ATC-438, page 15]

	Research Recommendations
1.	Include a weather component to future FAA, Department of Homeland Security (DHS) and Department of Defence (DOD) low-altitude UAS test sites and future Pathfinder evaluations to obtain feedback on operational significance of weather on BVLOS UAS operations
2.	Survey of ongoing weather research to determine the degree to which it aligns with identified UAS weather information gaps
3.	Investigate accessibility of existing weather technology and data to UAS operators
4.	Investigate hazardous weather alerting concepts for UAS operations
5.	Validate analysis and forecast performance of numerical models in UAS domains
6.	Evaluate use of airport observations and forecasts for local weather analysis
7.	Explore weather uncertainty concepts for contingency planning
8.	Investigate modification of existing aviation weather products (e.g., icing and turbulence models) for UAS applications
9.	Determine wind accuracy requirements to enable sustainable time-based operations
10.	Investigate methods for improving wind decision support for urban operations
11.	Define weather requirements for geofence boundaries
12.	Evaluate the ability of convective weather products to support BVLOS tactical navigation around convective weather
13.	Investigate the value of In-situ weather observations to support more detailed local analysis and as possible input to numerical weather models
14.	Develop weather impact models to support UAS airspace capacity management

Another research [15] addressing the shortcomings of current meteorological information for UAV use is the "SESAR Horizon 2020" research, part of the SESAR Horizon 2020 DREAMS research project, analysing the operational and technical aspects of UAV Air Information

Management (AIM) for the European Unmanned Aerial Vehicle Management System U-Space transport (European U-Space Unmanned Traffic Management System).

The essence of the DREAMS project is the analysis of the current goals and future needs of aeronautical information for unmanned aircraft flights. This research project investigated the operation of UAVs in very low altitude airspace. A comprehensive analysis of gaps in existing information services has been identified based on an online survey of traditional manned aviation providers and current U-Space service providers in accordance with the requirements of UAV operators and users. This research study points to information gaps that fall into seven key categories, one of which is meteorology. Proposals for solutions to bridge information gaps are also part of the research.

This analysis defined that the main problem from a meteorological point of view is the lack of hyperlocal data points, which is mainly caused by the absence of meteorological sensors. Only five countries (USA, UK, Canada, Germany and Norway) provide hyperlocal precipitation information and severe weather warnings relevant to UAV operations. The absence of hyperlocal wind warnings, which are especially necessary in urban traffic, is also a significant problem. In an urban environment, there are various features (such as several buildings) that play a significant role in creating uncertain wind vortices that could lead to unsafe UAV flights.

A solution to eliminate this problem would be to install sensors measuring and collecting meteorological data at a hyperlocal level, scaling and extrapolating hyperlocal weather information from Norway and Germany to other European states and providing weather information for UAV operations with a minute-to-minute frequency.

Questionnaire “Voice of the Customer” (VOC)

All previous researches and surveys found were conducted in North America [11],[14] or in general for the whole of Europe [15]. Since the test flights took place within Central Europe (Czech Republic, Slovak Republic and Poland), I decided to process my own survey and address potential respondents within these three countries, to which I sent the questionnaire. The aim of my own questionnaire is to verify whether UAV operators observe the same deficiencies in meteorological information in a given location or whether there are differences in this area in the deficiencies of current meteorological services.

The group of respondents consists of UAV operators within a wide range of applications: Construction, Agriculture, Energy, Photography, Hobbies and Entertainment, Emergency Services, Topography, etc.

All respondents are UAV pilots (license holders 3+ years), mainly using multicopters in the open category (A1, A2 and A3) for flights up to 100 meters.

The full questionnaire is provided in APPENDIX IV.

List below contains most important findings what were collected from UAV meteorological services VOC:

- All respondents use information issued by the national meteorological institute (SHMU, CHMU),
- All respondents use meteorological mobile apps,
- Most respondents use two meteorological sources for comparison,
- More than half of respondents use Webcam map to monitor the real image of the surrounding locations,
- Most respondents consider weather forecast as relevant for time horizon a maximum of 24 hours in advance,
- Most respondents perform the last meteorological info update one hour before the flight,
- 3 most anticipated and used weather parameters are: Wind, Temperature and Wind gusts,
- None of the respondents has ever used the paid UAV meteorological service,
- Almost 80% of respondents use only free meteorological sources of information,
- Respondents observe the largest deviation (reality vs. forecast) in wind and clouds,
- Respondents observe the most common deviation (reality vs. forecast) in wind and precipitations,
- The need to change or postpone the flight plan due to inaccurate forecasting is less than 5% of all flights,
- Most respondents do not observe frequent turbulence in the boundary layer as well as rapid wind changes,
- Half of respondents have experienced unexpected icing on UAV,
- Responders observed frequent “unexpected” turbulences when performing flights around buildings/bridges/pillars,
- Almost everyone observes larger deviations during flight in uneven terrain (hills, mountains),

The biggest weakness of the current meteorological data from UAV pilot’s point of view:

- Inaccurate overall weather forecast,
- Local changes depending on the surrounding relief,
- Inaccuracies related to precipitation, clouds, wind forecast and turbulences
- Each model predicts a different prediction (rarely match),
- Inaccuracy in time horizon 1 and more days.

The most common meteorological complication during the UAV flight:

- Wind gust and wind shear,
- Strong irregular wind,
- Predicting the strength and direction of the wind for very local conditions,
- Unexpected turbulences,
- Unexpected precipitation and clouds,
- Unexpected fog.

To be solved in order to achieve UAV safe operation:

- Larger networks of hyperlocal weather observatories,
- Time granularity of data: update every hour and not every 3 hours as it is most of the time today,
- Reliable forecast for more days in advance,
- Increase the accuracy of forecasted values,
- Improve prediction models,
- Increase the number of atmospheric measurements using meteodrones at different altitudes,
- UAV is quite sensitive to wind gusts and turbulences; hence unexpected wind changes and turbulences are a major complication.

A summary of the most critical points with respect to UAV dedicated meteo service to support safe UAV operations are:

- Wind behaviour – strong irregular wind, wind gust, wind shear,
- Frequent unexpected turbulences,
- Hyperlocal weather - forecasting the strength and direction of the wind for very local conditions is deemed very essential,
- Focus on precipitations, clouds, fog (increase the accuracy of those forecasts),
- Forecast inaccuracy for 1h+ time horizon.

This questionnaire proved that the most critical meteorological parameter for drone users is the wind and turbulence. The risk is considered due to sensitivity to wind gusts/shears/turbulence. Furthermore, precise values about the strength and direction of the prevailing wind for very local conditions is needed. Current, detailed, and accurate information about the wind and turbulence is the most important challenge that needs to be focused and improved.

Based on my questionnaire containing 48 questions focused on weather forecasting for UAV operations, I defined the weaknesses of the current services and the problems that UAV operators have to face. The set of questions was mainly oriented towards the point of view of direct users, so the results mainly reflect their opinion. In comparison with foreign studies, we see that the main problems and shortcomings of current meteorological forecasts also correspond to the location of Central Europe within the Czech Republic, Slovak Republic and Poland.

2.3 DEMONSTRATION MISSION- RZESZOW

After defining a summarizing set of weaknesses in current meteorological information, UAV test flights followed in order to verify the accuracy of meteorological forecasts using UAV onboard measurements of meteorological parameters. This section provides background information from a demonstration mission conducted in collaboration with DroneHub, Honeywell Aerospace, and Meteomatics. The results were published in article "Hyperlocal Weather Information for Drone Operations" [16].

Figure 1: Consortium of testing flights in Rzeszow

The original idea of test flights was to select among all meteorological providers at least two that met specified criteria, and both provided forecasts compared with directly measured data (using sensors installed on the UAV). Unfortunately, this determination of accuracy from two independent sources was not possible because only one meteorological provider "Meteomatics" [17] was able to provide grid data with a resolution of approximately 100 m horizontally and 10 m vertically within the area of interest. This fact clearly demonstrates that the availability of hyperlocal forecasts for drone purposes is very limited nowadays.

Based on the results of the VOC questionnaire, the main weaknesses were defined, what is necessary for the specific needs of the meteorological information requirements for very low-altitude drone use, which were verified during the demonstration mission. All demonstration flights were performed as part of the SESAR Joint Undertaking under the European Union's Horizon 2020, Project Number: 101017643 [18].

2.3.1 Physical components used in conjunction with directly measured data

The drone test vehicle (see Figure 2) is developed and operated by the Dronehub (Syracuse, NY, USA), with a location in Rzeszow. Meteorological testing was performed as part of the testing system for the task of drone rescue monitoring services. The first flights started in November 2021, and the second round started in March 2022. The aim of the mission was to demonstrate the possibility of using drones by rescue services for monitoring. The drone pilot planned the flight route along which the drone reached the call location and moved within the indicated area. The mission was carried out in Beyond Visual Line of Sight (BVLOS) mode. All flights were performed by an octocopter X8 (developed by Dronehub). The drone, named "FoxTech D130", is fully enclosed and powered by eight installed engines. Its flight time with the payload is up to 26 min. Sensors serving the following missions were integrated into the drone. The collection of meteorological data from drone flights was performed by an updated/tailored SC-Modem (see Figure 3) developed by Honeywell Aerospace Technologies (Phoenix, AZ, USA) within a previous project.

Figure 2: Drone in the box by DroneHub used for testing.

Figure 3: Honeywell SC-Modem (black box with fan) and sensors case included two meteorological sensors (white box on drone leg).

Meteorological data were directly measured by two installed sensors. The OW THERM sensor is produced by Okystar (Okystar Tech Co.,Ltd, Shenzhen, CN). It is an atmospheric sensor type used for temperature measurement. The measuring range is from –55 ◦C up to 125 ◦C The temperature measurement accuracy of this sensor is ±5 ◦C. The second meteorological sensor is named BARO. This sensor is produced by Okystar and is a position sensor type (accelerometer, gyroscope, magnetic field, pressure) used for temperature and barometric pressure measurement. The accelerometer’s measuring range is ±2, ±4, ±8, ±16 g and the gyroscope’s measuring range is ±250, ±500, ±2 000 ◦ /s.

Measured data were recorded on the drone, and via LTE connectivity, the data were uploaded to Azure for further processing. The MAVLink was used according to a lightweight communication protocol between the drone and ground control stations. It defined a set of bi-directional messages exchanged between a drone and a ground station. From all MAVLink-recorded messages, we used the information that was necessary to perform the analysis and to compare the meteorological data. Data generated and used from MQTT (Message Queuing Telemetry Transport) included latitude, longitude, altitude, and time information. Based on location and time data, we were able to clearly determine where the drone is located and to which reference point it is closest.

2.3.2 Data acquisition approach

Based on the plotting of the flight trajectory, relevant meteorological forecast points used for data analysis and comparison of “forecast versus reality” were determined. The area where the demonstration mission was allowed and planned was 600 m by 800 m in size. Most forecasts provide a resolution of several kilometres (3 km or more), meaning they can provide a single forecast for the entire area. Since the goal was to perform a detailed analysis, it was necessary to create a philosophy of reference points that would ensure the most detailed analysis possible. After a depth survey, it was determined that the most detailed data provided by Meteomatics were able with the resolution of 90 m horizontally and 10 m vertically within the area of interest. Based on this information, a network of reference points was created for every 100 m, which means that there are 54 reference points in a permissible area. Three different flight heights were forecasted for each reference point (60 m, 70 m and 80 m). Figure 4 details the referenced points. The actual flight path is drawn in red. The yellow rectangle shows reference points that were used for comparison. The strategy of comparing the measured parameters was implemented using selected reference points (Figure 4) For each single piece of data measured during the flight, the nearest point according to the longitude and latitude information of the reference was determined, and subsequently, the corresponding forecasts were used for comparison.

Each downloaded meteorological forecast contained data for 54 reference points, for 3 flight heights (60 m, 70 m, and 80 m), and for 5 selected parameters, namely: temperature [◦C], barometric pressure [hPa], wind speed [m/s] , wind direction [◦], and wind gust [m/s].

For the location of interest (Poland, Rzeszow), the data provided by Meteomatics was forecasted from the ECMWF-ifs model as a default. This model is updated four times daily: at 00, 06, 12, and 18 UTC. Additional improvements to the meteorological data forecast came from calibration with station measurements. There are several nearby stations in our area of interest. The data from weather stations is usually updated every 10 minutes, although some of them are updated every three hours. Model data calibrated with station measurements improves the quality of the data both for historical data and for the nowcast range (the next 6 hours). Meteorological forecasts were downloaded nine times a day, from 9 a.m. to 5 p.m. Every hour from the current time until the end of the flight day. Within the first week of the drone data measurements, a very detailed download scheme was selected. Based on this schedule, it was possible to see how often the forecast gradually changes and whether the rate of deviation is so significant that it is necessary to update on an hourly basis or whether the first morning forecast is sufficiently accurate for the entire flight day.

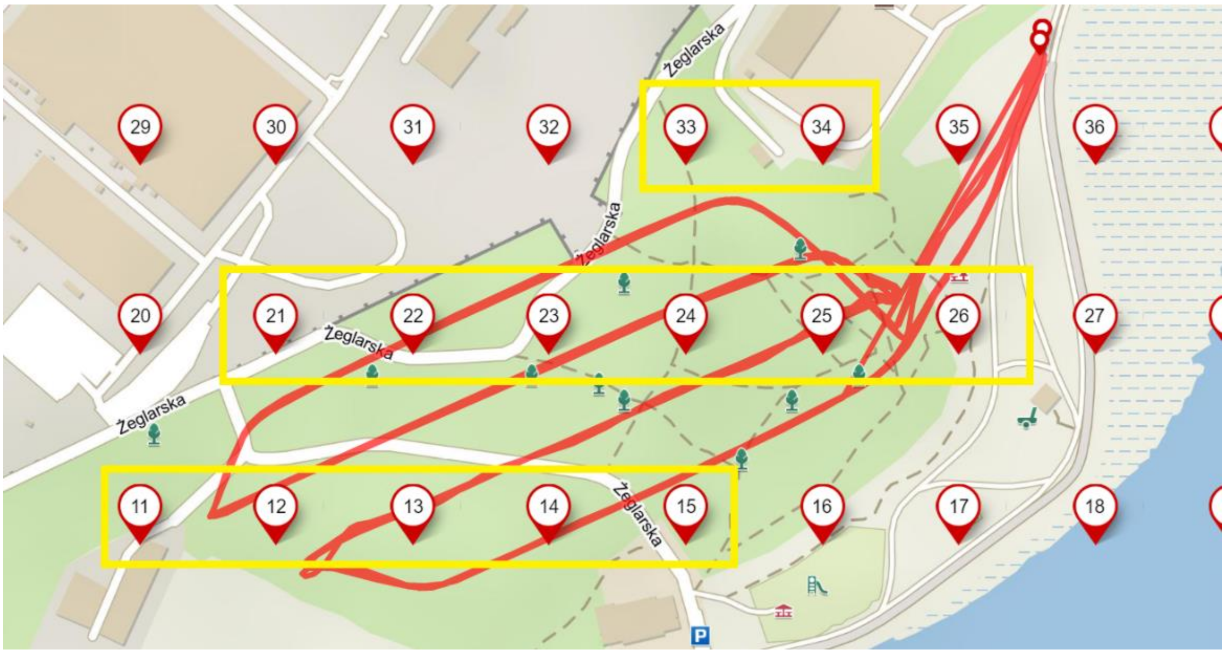

Figure 4: Reference points (highlighted in yellow) and flight path of the Beyond Visual Line of Sight mode testing flights.

2.3.3 Data exploitation methodology

The required meteorological data for the purposes of this project has its own specifics. Only one meteorological data provider out of all those contacted met all the required criteria. The selection of the final meteorological service provider was made among the following 15: Tomorrow, SkySight, Custom Weather, Windy, Meteomatics, Drone Forecast, Aeris Weather, Ambee, Ubimet, Meteopress, Weather Source, Stormglass, Aura, Open Weather, and Met Gis. After a selection process, Meteomatics was chosen as the weather forecast data provider. The initial idea was to select two meteorological data providers and compare the measured data against the predictions from the two independent sources. Unfortunately, we did not find a second provider that would meet all the set criteria.

The second major problem was forecasting at low altitudes (from 60 m to 80 m AGL). Most weather forecasts could provide hyperlocal data only for ground level or for too high levels. Currently, there is a very limited selection of low-altitude hyperlocal forecast providers. The meteorological provider “Meteomatics” brings proven interpolation techniques [19],[20] together with the most recent observational data taken from weather stations, satellite images, and radar and combines these with model data that has already been snapped to NASA’s 90-meter digital terrain model. The interpolation technique assists in the preparation of forecasts because it reduces the demand on the forecaster to draw or edit all required weather elements at all required times when changes are needed in guidance [21]. Meteomatics obtains a large part of the data from external providers (over 25 different models and over 60 different data sources) and then processes it further using various methods so that it is available to final customers in a useful and precise form. Meteomatics Mix combines different models and sources into an intelligent blend, such that the best data source is chosen for each time and location. In addition, Meteomatics also collects weather data with their self-developed meteodrones [22],[23]. The meteodrones collect data from the middle and lower atmospheric layers, a zone where typically not much data is available, and thus make a relevant contribution to data collection. The data collected by the meteodrones is fed directly into the weather model calculations, further improving the models.

To our knowledge, no studies have dealt with a specific comparison of predictions and direct measurements for hyperlocal data at low altitudes and defined exact deviations. All studies lead to the conclusion that current weather forecasts are not sufficient and that it is necessary to focus more on hyperlocal data. This idea is the main goal of the following comparison.

To be able to make an objective comparison of the measured data with the forecasted ones, a selection of input data was needed. Only the data collected during the flight, which took place in the range of determined flight levels from 60 m to 80 m, was analysed. Data recorded during take-off and landing phases outside steady flight level were separated. During the demonstration mission, one MAVLink error occurred (caused the loss of localization information) and had to be filtered; thus, only data with completed information containing GPS position were analysed.

The strategy of comparing the measured parameters was implemented using selected reference points. For each single piece of data measured during the flight, the nearest point of reference was determined, and subsequently, the corresponding forecasts were used for comparison. The reference points for which the forecasts were downloaded have a fixed value of latitude and longitude. The position of the drone was recorded using GPS. The comparison was based on matching the closest reference point to the drone's position during the flight time. By applying the longitude and latitude values, a straightforward calculation was used to get the closest reference point. The downloaded forecast was for three fixed altitudes: 60 m, 70 m, and 80 m, and therefore matching was also performed according to the drone height to the given flight levels. According to four input parameters (timestamp, latitude, longitude, and altitude), forecasted values were paired with directly measured values of meteorological parameters, and deviations were evaluated.

2.3.4 Deviations of measured metrological parameters at very low altitudes

The test flights took place over four days, when a total of 32 flights were performed. On November 18 (9 flights), on November 24 (11 flights), on March 8 (6 flights), and on the last flight day, March 10 (10 flights). Each day, flights were scheduled between 10 a.m. and 2 p.m. with each individual flight test lasting approximately 10 minutes. Deviations in the measurements were analysed and evaluated, always summarizing for the given flight day.

Table 3, Table 4 and Table 5 show the detailed measurement deviations and their minimum, maximum, and median values observed during the test day. The temperature was measured using two sensors, whose deviations from the forecast can be compared, and the barometric pressure using one sensor.

Table 3: Temperature deviations (Baro sensor)

Date	Minimum	Maximum	Median
18.11.2021	0.12 ◦C	1.057 ◦C	0.419 ◦C
24.11.2021	0.966 ◦C	2.8 ◦C	1.249 ◦C
08.03.2022	0.003 ◦C	2.144 ◦C	0.667 ◦C
10.03.2022	0.001 ◦C	6.111 ◦C	0.423 ◦C

Table 4: Temperature deviations (OW_Therm sensor)

Date	Minimum	Maximum	Median
18.11.2021	0.15 ◦C	0.8625 ◦C	0.4625 ◦C
24.11.2021	0.975 ◦C	2.6 ◦C	1.3 ◦C
08.03.2022	0.0125 ◦C	1.425 ◦C	0.6 ◦C
10.03.2022	0.003 ◦C	2.144 ◦C	0.25 ◦C

Table 5: Barometric pressure deviations (Baro sensor)

Date	Minimum	Maximum	Median
18.11.2021	0.006 hPa	2.904 hPa	1.352 hPa
24.11.2021	0.006 hPa	3.021 hPa	1.5255 hPa
08.03.2022	0 hPa	2.389 hPa	0.683 hPa
10.03.2022	0 hPa	1.957 hPa	0.58 hPa

The average deviation over all days of temperature measured by the BARO sensor is 0.69 ◦C and the OW THERM sensor is 0.65 ◦C. It is very important to remember that the temperature measurement accuracy of the OW THERM sensor is 0.5 ◦C. Based on these tests, the current temperature data provider for hyperlocal conditions at low altitudes can be considered sufficiently accurate, and this meteorological parameter does not need to be improved.

The BARO sensor's average barometric pressure deviation is 1.03 hPa, which indicates that it is sufficiently accurate for drone operation in hyperlocal conditions. There is no need to look for improvements and innovations to achieve greater accuracy for this basic meteorological parameter.

This analysis outlined another topic for research, namely the lack of information regarding low-altitude turbulence, which will be addressed in the next chapter 2.4. Turbulence at low altitude, in the context of this work, refers to the irregular and chaotic movement of air that can occur at low altitudes due to Earth surface and particularly around buildings, bridges, and other structures. This turbulence can be unpredictable and pose challenges for drone flights, especially in urban environments.

UAVs are quite sensitive to wind gusts and turbulence; hence, unexpected wind changes and turbulences are a major complication. Most respondents of the VOC questionnaire observe frequent "unexpected" turbulence during flights around buildings/bridges/pillars. While conducting a survey of meteorological information and service providers, we found that information about turbulence is a missing meteorological parameter that no one provides for hyperlocal conditions at low altitudes. The topic of turbulence detection at low altitudes has been addressed by several previous studies [10],[24],[25],[26],[27],[28]. The next part of the research will be focused on the detection of turbulence at low altitudes (the limit for this research is 150 m AGL).

2.4 TURBULENCE

Turbulence has long been recognized as one of the most hazardous meteorological phenomena in aviation, affecting both manned and unmanned aircraft, particularly those operating in close proximity to the ground. My preliminary research phase consisted of surveying UAV users regarding their satisfaction with current meteorological forecasts and also surveying providers of existing meteorological services focusing on hyperlocal predictions. These surveys clearly revealed that the primary shortcomings lie in the inaccuracies of predicted data related to wind characteristics and turbulence. Based on these findings, I have chosen to focus my dissertation research on the investigation of turbulence.

Turbulence, one of the most unpredictable atmospheric phenomena, poses a significant hazard to aviation. It manifests as irregular air movement caused by eddies and vertical currents. While turbulence can range from mild, causing only minor discomfort, to severe, potentially leading to temporary loss of aircraft control or even structural damage.

Turbulence occurs within turbulent flows, characterized by the mixing of fluid layers and the formation of vortices. Generally, fluid flow can be classified into two regimes: laminar and turbulent. The Reynolds number (Re) serves as a fundamental parameter for determining whether a flow is laminar or turbulent.

The Reynolds number is a dimensionless quantity employed in fluid dynamics to characterize the flow regime. It aids in distinguishing between laminar and turbulent flow. While often associated with pipe flow, the Reynolds number is also applicable to aerodynamic flows, such as the flow of air over an object or through a channel. In aerodynamics, the Reynolds number is typically defined without reference to pipe diameter.

The formula for the Reynolds number (Anderson, Houghton) in aerodynamic flow is as follows:

$$Re = (\rho V L) / \mu$$

Equation 1

Where:

- Re is the Reynolds number [dimensionless]
- ρ is the fluid density [kg/m^3]
- V is the fluid velocity relative to the object [m/s]
- L is the characteristic length of the object (e.g., its chord length for an air foil) [m]
- μ is the dynamic viscosity of the fluid [Ns/m^2]

In aerodynamics, the characteristic length (L) is typically chosen based on the specific flow situation. For instance, in the case of flow over an air foil, the chord length is often used as the characteristic length.

By calculating the Reynolds number for a given aerodynamic flow, it is possible to assess the nature of the flow (laminar or turbulent) and predict its behaviour.

2.4.1 Basic Classification of Turbulence Based on Origin

Turbulence arises due to two primary factors: dynamic and thermal. Thermal turbulence results from uneven heating of the Earth's surface and the presence of steep vertical temperature gradients. Dynamic turbulence, on the other hand, is generated by the friction between moving air and the rough terrain of the Earth's surface, as well as by inhomogeneities in wind speed and direction.

Turbulence is generally categorized into seven primary types, as outlined in Table 6. This classification system was developed by the National Weather Service (NWS) [29], a U.S. government agency under the National Oceanic and Atmospheric Administration (NOAA) responsible for providing weather, water, and climate data, forecasts, and warnings.

Table 6: Types of Atmospheric Turbulence

Type	Characteristics
Clear-air turbulence (CAT)	Turbulent movement of air masses without any visual cues (e.g., clouds), caused by the collision of air masses moving at significantly different speeds.
Wake turbulence	A highly turbulent disturbance generated behind an aircraft in flight, characterized by its short duration.
Mechanical turbulence	Friction between the air and the Earth's surface, particularly irregular terrain and man-made obstacles, generates vortices and consequently turbulence at low altitudes.
Mountain waves	Arises from the passage of airflow over mountainous terrain, causing oscillations on the lee side of the elevation due to the disruption of horizontal airflow caused by the terrain.
Convective (thermal) turbulence	Refers to turbulent vertical motions resulting from convective currents and the subsequent rising and sinking of air.
Frontal turbulence	Updraft at a frontal boundary.
Wind shear	The change in wind speed and/or direction with increasing altitude.

2.4.2 Basic Classification of Turbulence Based on Intensity

The categorization of turbulence intensity, based on the maximum value of the square root of Eddy Dissipation Rate (EDR), is defined by ICAO, 2.6 ICAO Annex 3 [12], Meteorological Service for International Air Navigation, as follows:

- **Light:** 0.1 to 0.4 EDR
  Characterized by slight, irregular changes in aircraft altitude and/or attitude.
- **Moderate:** 0.4 to 0.6 EDR
  Involves noticeable changes in aircraft altitude and/or attitude. Passengers may experience strain against seatbelts, and unsecured objects may be displaced.
- **Severe:** Above 0.6 EDR
  Characterized by large, abrupt changes in aircraft altitude and/or attitude. Passengers may be forcefully thrown against seatbelts, and unsecured objects may be tossed about.
- **Extreme:** Approaching 1.0 EDR
  Represents the most intense level of turbulence. Involves violent aircraft motions and is virtually impossible to control. May cause structural damage to the aircraft, and passengers may be subjected to extreme forces.

2.4.3 Limitations of PIREPs and the Rise of In-Situ Data in Aviation Meteorology

Before the advent of In-Situ data, pilot reports, known as PIREPs, were the sole routine source of turbulence observations. However, these reports are associated with several limitations:

- Inconsistent reporting across space and time
- Generally low reporting frequency
- Positional and temporal inaccuracies (In cases of severe turbulence, pilots prioritize aircraft control over reporting.)
- Subjective categorization into only four levels (light, moderate, severe, extreme)
- Aircraft dependency (moderate turbulence for a heavy aircraft may be severe for a light aircraft), leading to difficulties in interpreting information.

The need for automated, aircraft-independent atmospheric measurements is evident.

"In-Situ" is a Latin phrase that translates literally to "in place" or "in position." It refers to data collected at its original and natural location. In-Situ data processing involves analysing data where it is measured and stored.

Given the numerous shortcomings of PIREPs, the detection and prediction of turbulence for commercial aircraft is now shifting towards the utilization of In-Situ data. This data allows for the estimation of three key turbulence indicators:

- Vertical acceleration
- Derived Equivalent Vertical Gust (DEVG)
- Eddy Dissipation Rate (EDR)

By accessing accurate and objective aircraft-generated data through automated turbulence reports (with precise location information), several benefits can be realized:

- Optimization of flight paths based on real-time turbulence occurrences
- Enhanced situational awareness
- Contribution to a more comprehensive understanding and improved accuracy of atmospheric turbulence data at various altitudes
- Optimization of fuel consumption (through optimal flight altitude), thereby reducing CO2 emissions

The current proactive approach to turbulence detection is also driven by research predicting a significant increase in turbulence occurrences [30]. This research utilized computer simulations to examine changes in turbulence at 39,000 feet altitude under a scenario of doubled carbon dioxide levels. The findings indicated a substantial increase in severe turbulence (149%), severe-moderate turbulence (127%), moderate-light turbulence (75%), and light turbulence (59%). This increase is attributed to climate change amplifying wind shear and variations in wind speed and direction, major contributors to turbulence.

2.4.4 The Eddy Dissipation Rate (EDR) Method

The Eddy Dissipation Rate (EDR) quantifies the rate at which energy dissipates within the atmosphere. It is an objective, aircraft-independent, and universal measure of turbulence, representing the turbulent state of the atmosphere. The physical unit of EDR is ε, expressed in m^2/s^3. EDR signifies the rate at which energy cascades from large to small eddies within the inertial subrange. This energy is ultimately converted into thermal internal energy within the viscous subrange [31]. The primary advantages of this method include straightforward information sharing and the ability to translate information for specific aircraft types. This parameter alone suffices to fully characterize turbulence without the need for additional information or parameters.

EDR is estimated using two methods: either through the aircraft's vertical acceleration [32] or through the estimated vertical wind speed [33, 34]. The vertical wind-based EDR algorithm developed by the National Centre for Atmospheric Research (NCAR) (Sharman et al., 2014; Cornman, 2016) [33, 34] is currently implemented on some fleets of United Airlines, Delta Air Lines, and Southwest Airlines. The algorithm developed by Haverdings and Chan (2010), [32] is being tested on some aircraft of an airline based in Hong Kong. Although research [32] estimated EDR in a similar manner to research [34], they adopted a different angle-of-attack calibration and a different time window, which may cause a discrepancy between the two EDRs.

EDR is more useful than DEVG in terms of both turbulence detection and prediction metrics [33], as DEVG is not a direct measure of turbulence intensity but rather a gust load transfer factor. The International Civil Aviation Organization (ICAO) has designated EDR as the preferred and standard metric for turbulence reporting [12]. EDR is used in performance assessments of global turbulence prediction systems [35],[36], as well as in many turbulence-focused case studies [37],[38]. As these two different turbulence metrics are reported by different airlines, EDR reports cover most areas in the Northern Hemisphere, while DEVG reports have been primarily from the Southern Hemisphere. A study “Retrieval of eddy dissipation rate from derived equivalent vertical gust included in Aircraft Meteorological Data Relay“ [39] focused on converting AMDAR DEVG data to EDR to obtain more reliable and consistent observations of aviation turbulence, which should lead to improved verification of global aviation turbulence forecasts and the building of a global aviation turbulence climatology.

2.4.4.1 Current State of EDR Estimation Algorithm Development

FAA

Considering the shortcomings and challenges associated with PIREP reports, the Federal Aviation Administration (FAA) has been sponsoring activities related to In-Situ measurements for nearly 30 years through the AWRP and WTIC programs [40]. The FAA's Aviation Weather Research Program (AWRP) investigates applied weather with the goal of minimizing the impact of weather on the National Airspace System (NAS). The second FAA program, Weather Technology in the Cockpit (WTIC), develops minimum meteorological service recommendations for cockpit-provided meteorological information, weather-focused pilot training, and the integration of cockpit weather information technologies into standards, guidelines, and training materials, as well as their implementation through government agencies. The result and main focus of these long-standing research efforts is the focus on detection using the EDR method. The WTIC program supports the development and integration of In-Situ EDR software into operational systems such as ACMS or EFB. This is an open-source software package that includes Onboard Software, Online Debugging and Verification Software, Ground Data Reception and QC Software, and Documentation. This software is available through NCAR or IATA.

Thanks to FAA sponsorship, NCAR has developed in-situ algorithms for deriving and reporting turbulence encountered by commercial aircraft. The algorithms calculate the Eddy Dissipation Rate (EDR) from available onboard flight parameters. EDR is a turbulence metric representing the actual state of the atmosphere. This parameter is widely used in the research community as a measure of turbulence intensity and has been adopted as the ICAO standard for aviation turbulence. Approximately 100 Boeing 757 aircraft operated by United Airlines are currently equipped with software that relays EDR reports recorded at one-minute intervals (during flight). To reduce communication costs, the system operates on event-triggered logic. When an event exceeding a certain EDR value is detected, the logic triggers a downlink message. Routine reports are still provided, but at less frequent intervals. This improved algorithm was recently implemented on approximately 70 Boeing 737-800s operated by Delta Air Lines. The aviation industry is increasingly recognizing the benefits of this program, and it is expected that some form of In-Situ EDR observation systems will operate on most commercial aircraft flying on both continental U.S. (CONUS) and international routes.

IATA

IATA offers a platform called "Turbulence Aware" [41], which is EDR reporting software. This platform is based on the EDR algorithm developed by the National Centre for Atmospheric Research (NCAR - funded by the FAA). IATA provides technical support for implementation within airlines. EDR is a measure of energy dissipation, providing a calculated estimate of the turbulent state of the atmosphere. EDR is the official ICAO and WMO metric for measuring turbulence intensity. The "Turbulence Aware" platform is designed to enable industry-wide sharing of turbulence data to improve situational awareness and enhance safety. To be effective, it requires airlines to contribute their data to the global pool. Long-term access to the system is therefore based on a "give-to-get" approach, and participating airlines must implement EDR reporting.

In early 2020, there was a transition from the trial version to a fully functional service. Currently, the platform collects turbulence reports from 1,500 aircraft across 12 airlines. The following airlines are currently involved in contributing data to the global pool using EDR reports: Aer Lingus, Air France, Aegean, Ana, China Airlines, Delta, EasyJet, Korean Air, Lufthansa, Qatar Airways, Saudia, Southwest, Swiss, United, and Westjet.

The following images illustrate the difference between having only a small number of airlines contributing EDR reports versus a more comprehensive implementation of the platform.

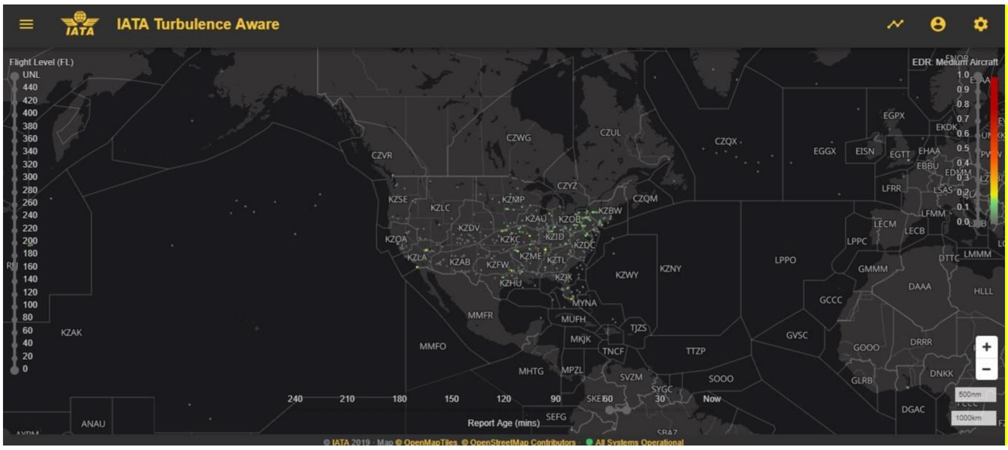

Figure 5: EDR reporting coverage with limited airline participation, source: [41]

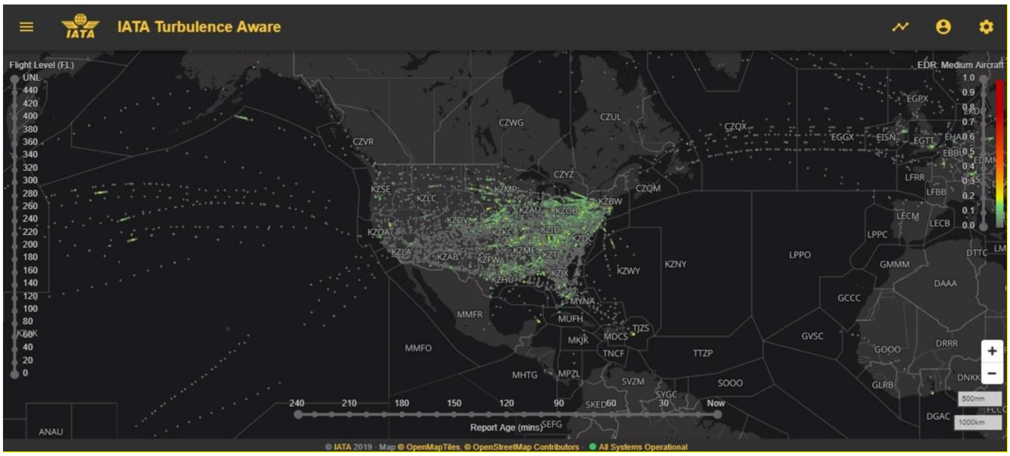

Figure 6: Comprehensive EDR reporting coverage, source: [41]

RTCA

RTCA is a non-profit organization in the USA that develops technical guidance for government regulatory bodies and industry. Founded in 1935, RTCA works closely with the Federal Aviation Administration (FAA) and industry experts from the USA and around the world to develop comprehensive, industry-vetted, and consensus-based recommendations regarding the use of standards. These standards can be used to achieve compliance with regulations set forth by the FAA and other aviation regulatory bodies. RTCA provides a forum for private sector stakeholders to collaborate in an open, fair, and balanced partnership through the development of recommendations, all while adhering to U.S. antitrust laws.

RTCA DO-370 (December 19, 2017): In-Situ Eddy Dissipation Rate (EDR) Algorithm Performance Guidelines. This document defines the minimum performance requirements for the use of a turbulence calculation algorithm using the Eddy Dissipation Rate (EDR) from In-Situ data (direct contact with the atmosphere).

Currently, several different methods for calculating EDR exist in the market, and none is preferred over the others; that is, there is no "gold standard" method for calculating EDR. Each method has advantages and disadvantages unique to the given algorithm. DO-370 defines "requirements" in the form of necessary statistical boundaries for test outputs to ensure that operational algorithms will generate operationally comparable reports that will be used by various end-users. The requirements of this document apply to EDR algorithm developers, where output characteristics are defined that apply to a universal set of EDR algorithms.

2.4.4.2 Current Usage of EDR Algorithms in Numbers

The following table illustrates the current implementation of In-situ EDR algorithms across various airline fleets. This data was presented in May 2022 at the "Aviation Weather Industry Technology Meeting" hosted by NCAR and the FAA.

Table 7: Summary of current usage of EDR algorithms

Airlines	
USA	Delta, Southwest, United, American
International	Swiss, Aer Lingus, Qantas, Air France, Cathay, Qatar, and many others
Aircraft type	
Boeing	777, 787, 737NG, 737MAX, 767
Airbus	32X, 330, 350
Systems	
ACMS	Honeywell, Teledyne
AID	Aircraft Interface Device
EFB	
Current Applications	
Input for GTGN	In-situ EDR data serves as a crucial input for Global Turbulence Guidance Nowcast (GTGN) systems, providing real-time information on turbulence conditions.
Direct Display in EFB Applications	EDR information is directly displayed in Electronic Flight Bag (EFB) applications, such as those provided by IATA or FWV, aiding pilots in making informed decisions regarding flight paths and altitudes.
Utilized by Aviation Meteorologists	Aviation meteorologists leverage In-situ EDR data for enhanced turbulence forecasting and analysis.
Aviation Meteorological Offices	Organizations like the Aviation Weather Center (AWC) utilize In-situ EDR data to improve their understanding of atmospheric turbulence and refine their forecasting models.
Science and Research	
Algorithm Development, Tuning, and Validation	Ongoing efforts focus on enhancing various turbulence prediction algorithms, including Global Turbulence Guidance (GTG), Global Turbulence Guidance Nowcast (GTGN), Global GTG, and the NCAR Turbulence Detection Algorithm (NTDA).
Case Studies	In-depth case studies are conducted to analyse specific turbulence events and validate the performance of different detection and prediction algorithms.
Climatology	Long-term In-situ EDR data is utilized to establish a comprehensive climatology of atmospheric turbulence, aiding in the identification of trends and patterns.

The primary areas of interest defined by the NCAR Research Applications Laboratory during the Aviation Weather Industry Technology Meeting held in Colorado on May 24, 2022, include the following goals:

- Data Quality Assessment: Continue to evaluate the quality of data from new and existing EDR data sources and facilitate their use as necessary.
- In-Situ EDR Deployment: Continue to support the further deployment of In-Situ EDR software across various aircraft fleets.
- EDR Standardization (Harmonization): Ensure operational comparability among different In-Situ EDR algorithms across diverse fleets (RTCA SC206 and ITSAT).

2.5 Low-level turbulence (LLT)

The majority of unmanned aerial vehicle (UAV) operations occur within the atmospheric boundary layer, typically with a maximum flight altitude of 150 meters above ground level. Consequently, the focus of this study is on turbulence detection and analysis within this specific flight regime.

One of the primary causes of turbulence within this lower airspace is friction between the airflow and the Earth's surface. This mechanical turbulence is particularly prevalent in areas with irregular terrain or man-made obstacles. Its intensity is influenced by the strength of surface winds, the nature of the terrain, and atmospheric stability. Turbulence intensifies with increasing wind speed (generally, significant turbulence requires surface winds of approximately 10 m/s or higher) and rougher or more built-up terrain, especially under unstable atmospheric conditions.

In this lower altitude range, turbulence often arises due to the abundance of obstacles (buildings, bridges, trees, etc.), which generate vortices as the airflow interacts with the terrain. This type of turbulence is referred to as "Low-Level Terrain-Induced Turbulence" (LLT). Another contributing factor is Convective Boundary Layer Turbulence (CBLT). CBLT occurs when a cooler air mass moves over a warmer surface. The heating from below creates unstable conditions, resulting in gusty winds and turbulent flight conditions.

In manned aviation, convective turbulence significantly impacts the flight path of an aircraft during landing approaches. The aircraft encounters convective currents of varying intensity as it descends towards the runway. These thermals can deflect the aircraft from its normal glide path, potentially causing it to overshoot or undershoot the runway.

2.5.1 Technologies for Low-Altitude Turbulence Detection

Lidar, sodar, and radar are the primary remote sensing technologies employed to obtain information about turbulence profiles in the lower atmosphere, particularly within urban environments [10],[43]. These sensing technologies offer spatial resolutions ranging from tens to hundreds of meters. However, spatial variations in turbulent airflow can be on the order of meters, significantly smaller than the resolution capabilities of lidar, sodar, and radar. This discrepancy can lead to substantial averaging and consequent errors in atmospheric turbulence measurements. Future UAV traffic management systems will necessitate the utilization of turbulence data acquired with high spatial resolution.

Acoustic anemometry is another method for obtaining turbulence information. Unlike the previously mentioned techniques, it can provide atmospheric data with high spatial resolution. However, achieving a complete picture of the atmospheric state at various altitudes using this method requires the placement of acoustic devices on meteorological towers or tethered balloons, which may not always be feasible in urban settings.

Each remote sensing technology for turbulence detection has limitations regarding the atmospheric conditions under which it can effectively collect data [43]. Lidars operating in the infrared spectrum require an atmosphere with a sufficient concentration of aerosol particles to act as scatterers and cannot collect data in very clean air conditions [112] or during heavy precipitation. This is because extremely clean atmospheric conditions with excellent visibility do not allow for the reflection of the emitted signal, while low visibility or the presence of precipitation causes absorption of the lidar signal. On the other hand, radars generally function well during light to moderate precipitation and can collect signals in some, but not all, clear-air conditions. Consequently, studies aiming to compare lidar and radar data are challenging due to the almost mutually exclusive atmospheric conditions under which each system can operate effectively. Sonic anemometers tend to provide erroneous results during precipitation [113], and tower-mounted instruments can be affected by tower vibrations [114].

A major trend in low-altitude turbulence sensing (i.e., up to altitudes of around 500 m) is the development of methods for diagnosing the turbulent atmosphere using UAVs, also known as meteodrones. In recent years, unmanned aerial systems have significantly expanded measurement capabilities, offering cost-effective and flexible sensor platforms for high temporal and spatial resolution turbulence detection. Several previous studies [25],[28],[44],[45],[46],[47] have explored this area, utilizing fixed-wing UAVs of various sizes and weights.

Diverse applications have been implemented in this field. One example is the SUMO (Small Unmanned Meteorological Observer) application at a wind farm in Denmark [25],[44], which demonstrated the system's ability to investigate wind turbine wakes, thereby supplementing information on wind field characterization and turbulence near wind turbines. Another research effort related to wind turbines and the atmospheric boundary layer was conducted in [47], where the turbulent 3D wind vector was measured using a fixed-wing unmanned aerial system equipped with a five-hole probe and an inertial navigation system.

Research efforts have explored the potential of unmanned aerial vehicles (UAVs) for investigating atmospheric boundary layer phenomena and turbulence. Studies [45],[46] describe flight tests and the potential application of UAVs for boundary layer studies in maritime environments. Research [28] outlines the components and utilization of a fixed-wing UAV equipped with a five-hole probe for measuring turbulence within the boundary layer. Additionally, an atmospheric sensing system comprising a UAV paired with vector sensors for pressure, temperature, humidity, and wind velocity was developed for measuring turbulence in the lower boundary layer.

During meteorological data collection, fixed-wing UAVs typically traverse the airspace for extended periods. A common flight pattern in turbulence measurement experiments consists of straight segments approximately one kilometre in length [48]. Consequently, the spatial resolution in turbulence spectra measurements is roughly comparable to the length of these straight segments. In the presence of uneven and inhomogeneous underlying surfaces and within a non-stationary atmosphere, the use of fixed-wing UAVs can lead to the same averaging errors observed with lidars, sodars, and radars, resulting in significant inaccuracies in atmospheric turbulence measurements [10]. When investigating atmospheric turbulence in areas with complex orography, diagnostic methods providing high spatial resolution data are preferred. Multicopters, unlike fixed-wing UAVs, lidars, sodars, and radars, enable the acquisition of atmospheric data with high spatial resolution [10].

The capabilities of a quadcopter under ideal conditions (nearly smooth and uniform surface) were examined in [49]. Turbulence spectra were derived from the quadcopter's pitch, roll, and yaw angle data and subsequently compared with measurements from an autonomous sonic meteorological station (AMK-03). The turbulent spectra obtained from the AMK-03 and the DJI Mavic Mini quadcopter were found to be consistent, with minor deviations in the high-frequency spectral range from approximately 1 Hz. The longitudinal and lateral turbulence scales were estimated using the least squares method with the von Karman model as the regression curve.

Study [10] demonstrates that utilizing a quadcopter in a constant altitude hover mode allows for the acquisition of turbulence spectra that align with measurements obtained through acoustic anemometry. These results provide evidence that quadcopters can be employed to study turbulence spectra and their characteristics, such as energy and inertial ranges, and the integral scale of turbulence. This capability enables monitoring and predicting the state of the turbulent atmosphere, for instance, during UAV-based cargo transport in smart cities.

As previously mentioned, measurements using fixed-wing UAVs can lead to significant errors due to averaging. This type of error can be mitigated by using UAVs capable of hovering at a single point for extended durations. Research [10] focuses on turbulence detection in hover mode. This study, utilizing a DJI Phantom 4 Pro in hover mode in conjunction with AMK-03 ultrasonic meteorological stations, demonstrates that quadcopters can acquire high spatial resolution atmospheric turbulent spectra in areas with complex orography. The results of investigating turbulence spectra in the inertial and energy ranges using a quadcopter in hover mode over homogeneous terrain show good agreement with the theory of homogeneous and isotropic turbulence and with measured data obtained using acoustic anemometry. This study concludes that in areas with complex orography, the behaviour of turbulent spectra measured by a quadcopter aligns with the atmospheric turbulence data obtained from the AMK-03 meteorological station. The findings suggest that rotary-wing UAVs can serve as a reliable tool for diagnosing the atmospheric boundary layer. Due to their ability to provide high spatial resolution data on the state of atmospheric turbulence, quadcopters are a promising tool for addressing UAV motion control challenges in adverse weather conditions, as well as for wind energy and climate measurements in urban environments and hard-to-reach locations.

While the majority of research focuses on deploying dedicated meteodrones for low-altitude meteorological observations, this approach inherently limits the spatial coverage of turbulence detection. An alternative strategy, inspired by current projects aimed at turbulence detection for commercial airlines, involves equipping all UAVs with a standardized in-situ EDR algorithm and enabling data sharing among them. In this paradigm, a local central hub would collect and process the aggregated turbulence data, issuing alerts and warnings to UAVs based on their planned flight paths.

For smart cities that envision utilizing UAVs extensively for cargo transport, monitoring, emergency response, and other purposes, achieving comprehensive implementation of EDR reporting across all UAVs operating within the airspace is imperative. This approach would facilitate a dynamic and real-time understanding of the turbulent atmospheric conditions, enabling safer and more efficient UAV operations.

2.5.2 Previous Research on Low-Altitude Turbulence Detection Using UAVs

Research [50] investigated unmanned aerial vehicles (UAVs) operated in close proximity to a VHF radar in the middle and upper atmosphere at the Shigaraki Observatory in Japan, up to an altitude of ~4.5 km, to compare with radar observations. The intensity of mechanical and thermal turbulence is described using the turbulence kinetic energy (TKE) dissipation rate "ε" and the temperature structure function parameter "C_T^2." For locally homogeneous, stationary, and isotropic turbulence in dry (unsaturated) air produced by shear instability in a stably stratified background, ε and C_T^2 are theoretically interconnected. ε can be estimated using C_T^2 as follows:

$$\varepsilon_{CT2} = \left(\gamma \frac{g^2}{T^2} \frac{C_T^2}{N^2}\right)^{3/2}$$

Equation 2

Where:

- ε is Turbulence kinetic energy (TKE) dissipation rate [m^2/s^3]
- g is the gravitational acceleration [m/s^2]
- N^2 is the square of the Brunt-Väisälä frequency expressed in terms of the (dry) potential temperature θ [$1/s^2$]
- C_T^2 is temperature structure function parameter [$K^2 m^{-2/3}$]

The parameter γ is:

$$\gamma = \frac{1}{\beta_\theta} \frac{1 - R_f}{R_f}$$

Equation 3

Where :

- γ [dimensionless]
- βθ is a universal constant with an approximate value of 3.0 [dimensionless]
- Rf is the flux Richardson number [dimensionless]. In the atmospheric turbulence literature, Rf is often assumed to be equal to 0.25.

3 AIM AND OBJECTIVES

Turbulence is one of the most dangerous meteorological phenomena we have ever encountered in aviation. This phenomenon affects classic manned aviation, but it is also a threat to unmanned aviation flying at low altitudes. Preparatory phase of the research consisted of a survey of the UAV users ‘satisfaction with current meteorological forecasts, as well as a survey of current meteorological service providers focused on hyperlocal forecasts. The surveys clearly showed that the biggest shortcomings are the inaccuracies of the forecast data regarding wind characteristics and turbulence. Therefore, the main area of interest chosen for dissertation thesis was turbulence and its detection at low altitudes.

Previous surveys have shown that sodars, lidars and radars are reliable tools for remote sensing of the turbulent atmosphere, and acoustic anemometers (tower mounted) are a popular contact monitoring method. However, all these methods do not provide a sufficiently high spatial resolution in the form of several meters. And precisely because of this lack, small UAVs have become a popular tool in the field of atmospheric monitoring in recent years. UAVs are beginning to be used mainly for low-altitude atmospheric sensing in hard-to-reach locations and in areas with complex orography, such as urban environments, mountainous terrain and the Arctic region.

The main trend in this area is the diagnosis of the wind speed characteristics of the airflow. However, in addition to the wind speed, it is also interesting to study the fluctuation characteristics of the turbulent atmosphere. Previous studies have dealt with low-altitude sensing of fluctuating characteristics of the turbulent atmosphere using a fixed-wing UAV. The sensing process is based on long-term UAV sensing, in order to obtain a representative series of observations of wind speed fluctuations. The result of these studies is the uncertainty in space when measuring the turbulence spectrum, which can be eliminated by using multi-rotor unmanned vehicles that are capable of a "hover" flight mode (hovering at a fixed point in space for a long time) and data collection in that mode.

Scientific studies show that the use of a quadcopter in the altitude hold mode allows obtaining a turbulence spectrum curve that is equal to measurements obtained using acoustic anemometry. This agreement confirms that the quadcopter can be used to study the spectrum of turbulence and its characteristics, for example, energy and inertial ranges and the integral scale of turbulence, and thus monitor and predict the state of the turbulent atmosphere (for example: the needs of UAV cargo transportation in a smart city).

Previous researches have shown that the UAV is the ideal tool for detecting turbulence at low altitudes. However, by integrating meteodrones into the airspace for the purpose of regular observation flights, only partial information will be obtained. If the aim is to provide comprehensive information, it is necessary that all UAVs be able to measure atmospheric turbulence using a metric that will not depend on the size and type of UAV. Information about the turbulent state of the atmosphere can be obtained from In-situ measurements using 3 indicators. One of these indicators is the energy dissipation rate (EDR), which is a calculated estimate of the turbulent state of the atmosphere. EDR is the official ICAO and WMO metric for measuring turbulence intensity. Currently, the implementation of the In-situ EDR algorithm developed by the NCAR laboratory is underway in commercial aviation. The goal is to support the deployment of the given software in as many fleets as possible to contribute to the global database and provide comprehensive data on the state of the turbulent atmosphere.

My research was inspired by the development and solution of this issue in the field of commercial aviation. The main idea is to modify this concept and incorporate it into the UAV world. This solution ensures that all unmanned vehicles would be able to measure the turbulent state of the atmosphere and share the data with each other. This method is verified using two approaches. One solution is only a software change and does not require any special additional hardware (indirect approach). The second solution is testing a low-cost sonic anemometer (direct approach). Smart cities are the question of the future, but detailed hyperlocal meteorological information with high accuracy needs to be solved before they start. A number of questions are connected with the creation of the given concept, which were solved during the research and are defined in detail as follows:

- Description of meteorological forecast for civil aviation.
- Research of the requirements and shortcomings of meteorological services for the future operation of unmanned vehicles.
- Analysis of the shortcomings of current meteorological services for unmanned operation in the location of Central Europe (in the form of a self-administered questionnaire).
- Based on previous research and self-administered questionnaire, identify the shortcomings of current meteorological forecasts for the future operation of unmanned aviation.
- Test flights for the purpose of comparing basic meteorological parameters of hyperlocal meteorological forecasts with directly measured data (using a quadcopter).
- Selection of a specific segment of interest from a summary list of weaknesses in current weather forecasts.
- Processing a summary overview of possible tools for solving the identified problem.
- Identification and selection of turbulence detection method.
- Process numerical simulations of turbulence in the built-up urban environment and subsequent interpretation of the obtained results and their use in creating the concept of a demonstration mission.
- Create a test flight scenario to determine the relationship between Eddy dissipation rate and interfering with the control and safety of the unmanned vehicle.
- Definition of limits for safe unmanned operation.

4 THEORY

The topics of interest were briefly covered in Chapter 2: State of the Art, and this Chapter 4: Theory continues the explanation and providing theoretical material in greater detail, which is essential for solving the specified issue.

4.1 Eddy Dissipation Rate – Review

The Eddy Dissipation Rate (EDR) is an objective, aircraft-independent, and universal measure of turbulence based on the rate at which energy dissipates in the atmosphere. In other words, it is a measure of the turbulent state of the atmosphere. The physical unit of EDR is ε in $m^2\ s^{-3}$. EDR represents the rate at which energy cascades from large to small eddies within the inertial subrange. This energy is ultimately converted into thermal internal energy in the viscous subrange [34]. The main advantages of this method are the ease of information sharing and the possibility of translating the information for a specific type of aircraft. This parameter is sufficient to fully characterize turbulence without the need for additional information or other parameters.

EDR is estimated using two methods, either through the vertical acceleration of the aircraft [35] or through the estimated vertical wind speed [36], [37]. The EDR algorithm based on vertical wind developed by the National Center for Atmospheric Research (NCAR) [36],[37] is currently implemented on some fleets of United Airlines, Delta Air Lines, and Southwest Airlines. The algorithm developed by Haverdings and Chan [35] is being tested on some aircraft of an airline based in Hong Kong. Although Haverdings and Chan [35] estimated EDR in a similar way to Cornman [37], they adopted a different angle of attack calibration and a different time window, which may cause a difference between these two EDRs.

EDR is more useful than DEVG in terms of turbulence detection metrics and turbulence prediction [36], as DEVG is not a direct metric of turbulence intensity but a gust load transfer factor. The International Civil Aviation Organization (ICAO) has designated EDR as the preferred and standard metric for turbulence reporting (ICAO, 2001). EDR is used in system performance assessments for global turbulence prediction [38],[39], as well as in many case studies focusing on turbulence [40],[41]. As these two turbulence metrics are reported by different airlines, EDR reports cover most areas in the Northern Hemisphere, while DEVGs have been reported in the Southern Hemisphere. Study [39] focused on converting AMDAR DEVG data to EDR to obtain more reliable and consistent observations of aircraft turbulence, which should lead to improved verification of global aircraft turbulence forecasts, as well as to building a global climatology of aircraft turbulence.

4.2 NCAR algorithm not applicable for multicopters

The current version of the EDR algorithm created by NCAR, as described in chapter 2.4., is not applicable for multicopters. The list of required parameters contains parameters that cannot be measured on a multicopter. One such parameter is, for example, Angle of attack. For this reason, it was necessary to summarize the EDR calculation options and subsequently find an alternative that is easily applicable to multicopters. In the following section 4.3. Velocity processing methods for turbulent dissipation rate are presented.

4.3 EDR calculation possibilities

The eddy dissipation rate (EDR), which is the cube root of the dissipation rate of turbulent kinetic energy, and hence has units of $m^{2/3}\ s^{-1}$. Chapter 4.3. describes all velocity processing methods for the dissipation rate of turbulent kinetic energy.

Turbulent flows exhibit significant intermittency, marked by intense bursts of vorticity and strain. Kolmogorov theory explains this phenomenon through energy cascades from larger to smaller spatial and temporal scales, dissipating energy as heat. However, the reasons behind the high intermittency in turbulence, characterized by non-Gaussian statistics, remain poorly understood. This intermittency can have notable effects, such as the formation of intense vortices in atmospheric flows. Analysing the statistics of all measurements and the progression of individual bursts, were observed in the American research [42] that a typical sequence for intense events begins with rapid strain growth, followed by an increase in vorticity, and concludes with a sudden decline in stretching.

Hence, it is essential to quantify the velocity gradient tensor in turbulent flows as it plays a crucial role in estimating the turbulent dissipation rate [43].

4.3.1 Fluctuating velocity gradients

The calculation of turbulent dissipation rate can be directly derived from its definition [51]:

$$\varepsilon = v \left\{ \begin{array}{c} 2\overline{\left(\frac{\partial u}{\partial x}\right)^2} + \overline{\left(\frac{\partial v}{\partial x}\right)^2} + \overline{\left(\frac{\partial w}{\partial x}\right)^2} + \overline{\left(\frac{\partial u}{\partial y}\right)^2} \\ +2\overline{\left(\frac{\partial v}{\partial y}\right)^2} + \overline{\left(\frac{\partial w}{\partial y}\right)^2} + \overline{\left(\frac{\partial u}{\partial z}\right)^2} + \overline{\left(\frac{\partial v}{\partial z}\right)^2} \\ +2\overline{\left(\frac{\partial w}{\partial z}\right)^2} + 2\left(\overline{\left(\frac{\partial u}{\partial y}\right)\left(\frac{\partial v}{\partial x}\right)} + \overline{\left(\frac{\partial u}{\partial z}\right)\left(\frac{\partial w}{\partial x}\right)} + \overline{\left(\frac{\partial v}{\partial z}\right)\left(\frac{\partial w}{\partial y}\right)} \right) \end{array} \right\}$$

Equation 4

Where:

- ε is Turbulent kinetic energy dissipation rate $[m^2/s^3]$
- v is Kinematic viscosity of the fluid $[m^2/s]$
- u, v, w are Fluctuating velocity components in the x, y, and z directions [m/s]
- $\partial u/\partial x$, $\partial v/\partial x$, ... $\partial w/\partial z$ are spatial gradients [1/s]

To determine the turbulent dissipation rate, it is necessary to measure the gradients in three directions of three fluctuating velocities. While this is routinely accomplished in direct numerical simulations (DNS) of turbulence [52], it poses a challenge for all velocity measurement techniques. This challenge becomes evident in apparent inconsistencies in measured small-scale statistics, such as the disparity between measured enstrophy production and velocity gradient skewness. Due to the limited number of velocity gradients that can be measured, various simplifications are often employed to calculate turbulent dissipation rates from fluctuating velocity gradients. In the case of the simplest turbulence, homogeneous and isotropic turbulence, the dissipation rate can be computed from a single velocity gradient as:

$$\varepsilon_i = 15\,\upsilon\overline{(\frac{\partial u_i}{\partial x_i})^2}$$

Equation 5

Where:

- ε_i is turbulent dissipation rate of homogenous and isotropic turbulence $[m^2/s^3]$
- v is Kinematic viscosity of the fluid $[m^2/s]$
- $\partial u_i/\partial x_i$ are spatial gradients [1/s]

In accordance with Taylor's hypothesis for a frozen turbulence pattern [53], the turbulent dissipation rate can be computed from the time series of fluctuating velocity. The expression is given by:

$$\varepsilon_i = \frac{15\,\upsilon}{U_1^2}\overline{(\frac{\partial u}{\partial t})^2}$$

Equation 6

Where:

- ε_i is turbulent dissipation rate $[m^2/s^3]$
- v is Kinematic viscosity of the fluid $[m^2/s]$
- U_1 is the mean flow velocity in the streamwise direction [m/s]
- $\partial u/\partial t$ is time derivative of the fluctuating velocity component $[m/s^2]$

This expression is valid when the fluctuating velocity is significantly smaller than the mean velocity, where U_1 represents the mean streamwise velocity component. Research [54],[55] treated turbulence as statistically isotropic but non-homogeneous. They estimated the unknown velocity gradients from the measured ones, leading to a simplified form of the dissipation rate defined by:

$$\varepsilon = \upsilon\left(2\overline{(\frac{\partial u}{\partial x})^2} + 2\overline{(\frac{\partial \upsilon}{\partial y})^2} + 3\overline{(\frac{\partial \upsilon}{\partial x})^2} + 3\overline{(\frac{\partial u}{\partial y})^2} + 2\overline{\frac{\partial u}{\partial y}\frac{\partial \upsilon}{\partial x}}\right)$$

Equation 7

Where:

- ε is Turbulent dissipation rate $[m^2/s^3]$
- v is Kinematic viscosity of the fluid $[m^2/s]$
- $\partial u/\partial x$, $\partial v/\partial y$, $\partial v/\partial x$, $\partial u/\partial y$ are Spatial gradients of the fluctuating velocity components [1/s]

The turbulent dissipation rates obtained through the estimation provided in Equation 7 are superior to those calculated using Equation 5. In certain scenarios, the assumption of isotropic turbulence is not applicable. In cases where small-scale turbulence can be assumed to be locally axisymmetric, as proposed by [56],[57], the turbulent dissipation rate can be formulated as:

$$\varepsilon = \nu\left(-\overline{\left(\frac{\partial u}{\partial x}\right)^2} + 8\overline{\left(\frac{\partial v}{\partial y}\right)^2} + 2\overline{\left(\frac{\partial v}{\partial x}\right)^2} + 2\overline{\left(\frac{\partial u}{\partial y}\right)^2} \right)$$

Equation 8

Where:

- ε is turbulent dissipation rate $[m^2/s^3]$
- ν is Kinematic viscosity of the fluid $[m^2/s]$
- $\partial u/\partial x$, $\partial v/\partial y$, $\partial v/\partial x$, $\partial u/\partial y$ are Spatial gradients of the fluctuating velocity components [1/s]

It is noteworthy that the directly estimated turbulent dissipation rate from fluctuating velocity gradients, under the assumptions of isotropy, local isotropy, or local axisymmetric, decreases as the interrogation size increases [58]. This trend is largely influenced by the resolution of measurements.

4.3.2 Smagorinsky closure method

When a dynamic equilibrium is reached, characterized by a balance between the energy transferred from the largest scales to the smallest scales, the estimation of turbulent dissipation rate can be derived from the flux of turbulent kinetic energy through the inertial subrange [59]. This forms the basis for employing the Smagorinsky sub-grid model in large eddy particle image velocimetry (PIV) for turbulent dissipation rate estimation. An apparent advantage of this approach is that velocity measurements do not necessarily have to resolve the Kolmogorov scales. The turbulent dissipation rate can be approximated as the sub grid scale dissipation rate at the PIV resolution, expressed as:

$$\varepsilon = \frac{1}{2}\nu_T\overline{\left(\frac{\partial u_i}{\partial x_j} + \frac{\partial u_j}{\partial x_i}\right)^2}$$

Equation 9

Where:

- ε is turbulent dissipation rate $[m^2/s^3]$
- $\partial u_i/\partial x_j$, $\partial u_j/\partial x_i$ are Spatial gradients of the velocity components [1/s]
- ν_{T} is turbulent viscosity $[m^2/s]$, which can be calculated from the measured turbulent velocity gradients as Equation 10.

$$\nu_T = (C_s\Delta)^2\left[\frac{1}{2}\left(\frac{\partial u_i}{\partial x_j}+\frac{\partial u_j}{\partial x_i}\right)^2\right]^{1/2}$$

Equation 10

Where:

- v_T is turbulent viscosity [m^2/s]
- C_s is the Smagorinsky constant [dimensionless]
- Δ is the grid scale corresponding to the PIV spatial resolution [m]
- $\partial u_i/\partial x_j$, $\partial u_j/\partial x_i$ are Spatial gradients of the velocity components [1/s]

The turbulent dissipation rate is given by:

$$\varepsilon = (C_s\Delta)^2\left\{\begin{array}{c} 2\overline{\left(\frac{\partial u}{\partial x}\right)^2}+\overline{\left(\frac{\partial v}{\partial x}\right)^2}+\overline{\left(\frac{\partial w}{\partial x}\right)^2}+\overline{\left(\frac{\partial u}{\partial y}\right)^2} \\ +2\overline{\left(\frac{\partial v}{\partial y}\right)^2}+\overline{\left(\frac{\partial w}{\partial y}\right)^2}+\overline{\left(\frac{\partial u}{\partial z}\right)^2}+\overline{\left(\frac{\partial v}{\partial z}\right)^2} \\ +2\overline{\left(\frac{\partial w}{\partial z}\right)^2}+2\left(\overline{\left(\frac{\partial u}{\partial y}\right)\left(\frac{\partial v}{\partial x}\right)}+\overline{\left(\frac{\partial u}{\partial z}\right)\left(\frac{\partial w}{\partial x}\right)}+\overline{\left(\frac{\partial v}{\partial z}\right)\left(\frac{\partial w}{\partial y}\right)}\right) \end{array}\right\}^{3/2}$$

Equation 11

Where:

- ε is Turbulent dissipation rate [m^2/s^3]
- C_s is the Smagorinsky constant [dimensionless]
- Δ is the grid scale corresponding to the PIV spatial resolution [m]
- ∂u/∂x, ∂v/∂y, ∂v/∂x, ∂u/∂y are Spatial gradients of the fluctuating velocity components [1/s]

It's important to note that there is no consensus on the value of the Smagorinsky constant. Research [60] adopted a value of 0.17, [55] chose 0.21, and Research [61] suggested 0.11. The recommendation is to select the value based on the ratio between the spatial resolution and the Kolmogorov scale [62]. Research [63] argued that the Smagorinsky constant for PIV measurements should be contingent on measurement conditions, including interrogation window overlap, the elements used in the strain tensor, and the method of approximating derivatives. Most research has focused on 2-D PIV, where only five out of twelve terms in the turbulent dissipation rate definition can be determined. To estimate turbulent dissipation rate using large eddy PIV, assumptions of isotropic or axisymmetric flow need to be made.

4.3.3 Dimensional analysis

Research [64] proposed a form for the turbulent dissipation rate through dimensional analysis. The mechanism of turbulence dissipation is rooted in the Richardson-Kolmogorov cascade, assuming that turbulence is in equilibrium. In this equilibrium cascade, the rate at which kinetic energy crosses a length scale is consistent across scales from the largest to the smallest [65] and [66]. The energy transfer rate can be characterized by the fluctuating velocity, *u'*, over the integral length scale, l_e.

The energy transferred is turbulence kinetic energy, u'^3. Therefore, the turbulent dissipation rate can be expressed as:

$$\varepsilon = \frac{C_\varepsilon u'^3}{l_e}$$

Equation 12

Where:

- ε is Turbulent dissipation rate [m^2/s^3]
- C_ε: Constant [dimensionless]
- u': Fluctuating velocity [m/s]
- l_e: Integral length scale [m]

The expression includes the constant C_ε, derived from the assumption of equilibrium [67] and [31]. Although the dimensionless dissipation rate was observed to be nearly constant at sufficiently high Taylor Reynolds numbers in experiments [69], caution is advised in accepting this assumption lightly [70]. It has been found that C_ε is not universal, varying based on initial conditions, inlet/boundary conditions, and the type of flow [71],[72],[73]. Even in statistically stationary isotropic turbulence, the time lag between energy injection and dissipation must be considered when estimating C_ε at a specific time step [74].

Experimental evidence by Valente et al. [75] demonstrated that C_ε followed $f(Re_M)/Re_L$ during the decay of grid-generated turbulence, with Re_M as the global Reynolds number and Re_L as the local Reynolds number. This observation has been confirmed by results from other independent grid-turbulence experiments [76],[77] and DNS simulations [78],[79], illustrating that C_ε is a function of Reynolds number.

McComb et al. [80] explained that the decay of dimensionless dissipation with increasing Reynolds number is attributed to the increase in the Taylor surrogate.

The integral length scale represents the correlation distance of velocity components in space and can be determined by integrating the velocity correlation function, requiring simultaneous measurements of velocities at two different positions. When Taylor's frozen hypothesis is applied, the velocity at a different position can be estimated from the time series of velocity measurements at one point [81]. [82] assumed that the integral length scaled as the diameter of the tank, while [83] assumed the integral length to scale as half the diameter of the tank. [84] considered that the dimensional analysis method provided accurate results for le when assumed as one-tenth of the diameter of a stirred tank, with the constant Ce assumed to be equal to one.

[85] approximated the above equation to estimate the distribution of turbulent dissipation rates in a stirred tank using LDV as:

$$\varepsilon = \frac{C_{\varepsilon} u_r'^3}{\tau \sqrt{\bar{U}_r^2 + u_r'^2}}$$

Equation 13

Where:

- ε is Turbulent dissipation rate [m²/s³]
- Cε is Constant = 1 [dimensionless]
- u'r is Fluctuating velocity in the radial direction [m/s]
- τ isTime scale [s]
- Ur is Mean velocity in the radial direction [m/s]

And τ is given by:

$$\tau = L_r / \bar{U}_c ; \bar{U}_c = \sqrt{\bar{U}^2 + u'^2}$$

Where:

- τ isTime scale [s]
- Lr is Integral length scale in the radial direction [m]
- Uc is velocity scale [m/s]
- u‘ is fluctuating velocity [m/s]

The subscript "r" denotes the radial direction. According to research [86], the underlying assumptions when using the above equation to estimate local turbulent dissipation rates are:

- an energy cascade from large vortices to small vortices;
- local equilibrium between turbulence production and dissipation;
- local isotropy of small scales.

Research [86] further quantified the constant "A" as 0.85. [87] simplified le as one-tenth of the diameter of a stirred tank. [88] calculated the integral length scale from an energy balance calculation throughout the tank, achieving a value of 1 / 8.71 tank diameter. [61] used 2-D spatial autocorrelation to calculate the integral length scale for the estimate of local turbulent dissipation rate from dimensional analysis using local fluctuating velocity.

There is a wide variation in the assumed integral length scale, and furthermore, there is no consensus on the choice of constant C_{ε}. Additional analysis is necessary to determine suitable values for these parameters in specific applications.

4.3.4 Structure function

In the inertial subrange, the relationship between the turbulent dissipation rate and the velocity structure functions is established through the Kolmogorov second similarity hypothesis [68]. The definition of the second-order velocity structure function is as follows:

$$D_{ij}(r,t) = \langle (u_i(x+r,t) - u_i(x,t))(u_j(x+r,t) - u_j(x,t)) \rangle$$

Equation 14

Where:

- Dij(r,t) is the second-order velocity structure function. (It quantifies the average difference in the velocity components u_i and u_j between two points separated by a distance r at a given time t. [m/s^2]
- r is Spatial separation between two points in the flow field [m]
- t is Time instant at which the velocity structure function is evaluated [s]
- ui(x + r, t) is the i-th component of velocity at position x + r and time t. [m/s]
- ui(x, t) The i-th component of velocity at position x and time t [m/s]
- uj(x + r, t) is the j-th component of velocity at position x + r and time t [m/s]
- uj(x, t) is the j-th component of velocity at position x and time t [m/s]

The second-order velocity structure function in the longitudinal direction is expressed as:

$$D_{LL}(r,t) = \left\langle (u_1(x+r,t) - u_1(x,t))^2 \right\rangle$$

Equation 15

The second-order longitudinal velocity structure function takes the form of a function of the turbulent dissipation rate within the inertial subrange, expressed as:

$$D_{LL}(r,t) = C_2(\varepsilon r)^{2/3}$$

Equation 16

In this expression, C_2 represents a universal constant, as per [89], and a determined value of 2.12 is assigned. The third-order longitudinal velocity structure function is also a function of the turbulent dissipation rate within the inertial subrange, formulated as:

$$D_{LLL}(r,t) = C_3 \varepsilon r$$

Equation 17

Kolmogorov [67] specified C_3 as 0.8. [90] proposed that coefficients C_2 and C_3 are Reynolds number-dependent, based on the Taylor microscale. This consideration has been identified as a significant factor contributing to the underestimation of the turbulent dissipation rate.

4.3.5 Energy spectrum

The Kolmogorov second similarity hypothesis [68] formulates the longitudinal energy spectrum in the inertial subrange as follows:

$$E_{11}(k_1) = C_1 \varepsilon^{2/3} k_1^{-5/3}$$

Equation 18

In this equation, C_1 represents a universal empirical constant, with a suggested value of 0.53 according to [89]. The turbulent dissipation rate can be obtained by fitting the energy spectra curve, applying a $k^{(-5/3)}$ curve fit to the inertial subrange of E_{11}. This relationship is expressed as:

$$\varepsilon = \left(\frac{1}{C_1} k_1^{5/3} E_{11}(k_1) \right)^{3/2}$$

Equation 19

As per [91], $E_{11}(k_1)$ can be derived from the cosine transform of the longitudinal spatial correlation function, expressed as:

$$E_{11}(k_1) = \frac{2}{\pi} \langle u_1'^2 \rangle \int_0^{\infty} f(r_1) cos(k_1 r_1) dr_1$$

Equation 20

The longitudinal energy spectrum can also be acquired by conducting a Fourier transform of PIV velocity data. Following the formulation by [92], $E_{11}(k_1)$ can be expressed as:

$$E_{11}(k_1) = \frac{1}{\Delta k_1} \frac{1}{N^2} \sum_{j=0}^{N/2-1} \hat{u}_j \hat{u}_j^*$$

Equation 21

In this equation, N represents the number of points undergoing transformation, u_j signifies the Fourier transform of u'_1, and u_j^* denotes the complex conjugate of the Fourier transform. The Fourier transformation of PIV measurements typically involves the use of fast Fourier transform, which necessitates data to be periodic. To achieve periodicity, PIV measurements can be transformed by constraining the velocity to 0 at the boundaries of the observation area [93].

4.3.6 Forced balance of the TKE equation

[94] proposed that the local turbulent dissipation rate can be obtained by solving the turbulent kinetic energy equation, as:

$$\frac{\bar{D} k}{\bar{D} t} = \frac{\partial}{\partial x_j} \left[-\frac{\langle u_j p' \rangle}{\rho} + 2\upsilon \langle u_i s_{ij} \rangle - \frac{1}{2} \langle u_i u_j u_j \rangle \right] - 2\upsilon \langle s_{ij} s_{ij} \rangle - \langle u_i u_j \rangle \langle S_{ij} \rangle$$

Equation 22

In the provided equation, the first term on the right-hand side accounts for the transport of turbulence kinetic energy by pressure, viscous stresses, and Reynolds stresses. The second term represents the rate of dissipation of turbulence kinetic energy, while the last term corresponds to turbulence production.

By considering the balance of turbulent kinetic energy, the turbulent dissipation rate can be expressed in the following manner:

$$\begin{aligned}\varepsilon = \frac{\partial}{\partial x_j}\left[-\frac{\langle u_j p'\rangle}{\rho} + 2\upsilon\langle u_i s_{ij}\rangle - \frac{1}{2}\langle u_i u_j u_j\rangle\right] - \langle u_i u_j\rangle\langle S_{ij}\rangle \\ - \frac{\partial}{\partial t}\left(\frac{1}{2}\,\bar{u_i' u_i'}\right) - \bar{u_j}\,\frac{\partial}{\partial x_j}\left(\frac{1}{2}\,\bar{u_i' u_i'}\right)\end{aligned}$$

Equation 23

To determine each term, certain assumptions must be made, particularly for the first term on the right-hand side representing pressure diffusion, which cannot be directly measured. The advantage of this approach lies in not requiring flow measurements to resolve down to the dissipative Kolmogorov scales. However, a drawback is that the estimated turbulent dissipation rate is susceptible to errors introduced in estimating each term. [95] applied this method to estimate the turbulent dissipation rate in a stirred tank using the balance equation of turbulent kinetic energy. While each term was derived from PIV measurements, the pressure diffusion term, unattainable from PIV data, was assumed to be negligible. This same methodology was employed to determine the fraction of total energy dissipated in the impeller region [96].

4.4 Wind measurement techniques for multi-rotor UAV

Wind estimation in the lower atmosphere is limited by the difficulty of performing detailed observations within atmospheric boundary layer, especially in urban area. The beginning of In-situ observations used tethered balloon system with implemented cup and vane anemometer. This method is very challenging for handling the system and also very expensive (Research activities with tethered balloon system: [97], [98]). Technological progress and the advent of the UAV system provides a new alternative to real-time data collection at low altitudes. Fixed-wing unmanned aerial vehicles were the first to be used for atmospheric observations, but they are not suitable for wind velocity estimation (Research activities with fixed-wing UAV [99], [100], [101]). UAV with fixed-wing platform is no table to stay in hovering mode as multi-rotors. Hovering mode is a key advantage of multirotors in the sense of wind estimation. The hover mode allows to measure vertical wind profiles or the temporal variability of the wind at one point in space. Another advantage of multi-rotors is vertical take-off and landing capability. These advantages make the multirotor copter an ideal platform to measure vertical profiles or to obtain temporal changes of meteorological variables at a fixed location [102]. Multirotors UAV are ideal for In-Situ wind data estimation because of low-cost concept, reusable, easy to operate, usable in hard-to-reach places.

The purpose of this research activity is to find the simplest and most economical solution that would be applicable on a wide scale of unmanned operation. An ideal variant would be an alternative where the wind speed would be estimated from the movements of the drone and only a software adjustment would be sufficient to provide the EDR metric. The second alternative is to find low-cost hardware equipment that will ensure direct measurement of real time data on board the unmanned vehicle. The following subsection describes the technical measurement options that exist for measuring In-situ wind characteristics as well as the final selection that will be tested. This section describes the sensor hardware and associated estimation techniques used to estimate wind speed and wind direction for multi-rotor UAV platform. Based on existing literature, wind speed measuring techniques can be divided into four groups according on the hardware used, as depicted:

a) Single Pitot-static tubes

A pitot-static tube (also called Prandtl tube) is used to measure the dynamic pressure P_d of a moving fluid (air).

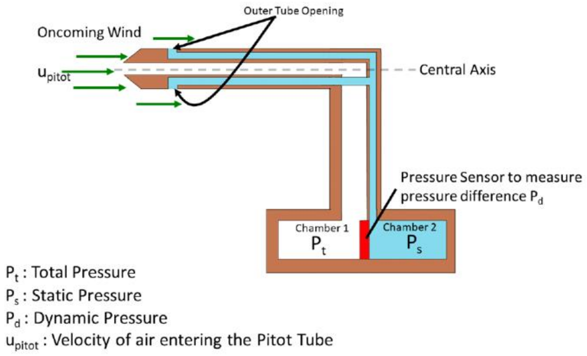

Figure 7: Pitot-static tube principle

As is shown in Figure 7, a pitot-static tube consists of a probe that faces the direction of the oncoming wind. The tube has an opening along its central axis that allows the oncoming wind to pass through the main channel and into Chamber 1. The two openings on the outer surface of the tube (outer tube openings) are connected to a set of channels leading to Chamber 2. The channels leading to Chamber 2 (shown in blue) are kept separate from the main channel. The incoming air is brought to rest in Chamber 1 since there is no outlet and holds the total pressure of the fluid P_t.

Static pressure P_s refers to the pressure of the fluid surrounding the tube. The openings connected to Chamber 2 are perpendicular to the direction of oncoming wind flow. As such, Chamber 2 holds air at static pressure. A transducer element placed between Chamber 1 and Chamber 2 measures the pressure difference between total pressure P_t and static pressure P_s. This pressure difference is the dynamic pressure of air, P_d. The dynamic pressure P_d measured is then used to estimate the air speed of the pitot tube mounted on the aerial vehicle. This estimation is accomplished through Bernouli’s equation which states that total pressure is the sum of dynamic pressure and static pressure.

A pitot tube is used to measure airspeed in the direction that the tube is pointed. In case of a multi-rotor’s UAV needs to measure airspeed in multiple directions, several pitot tubes would be necessary, which would increase the weight and complexity of the aircraft. In comparison to fixed-wing UAVs, the use of flow sensors in multi-rotor vehicles is limited by interference from the rotors (rotor wash), [103] and [104]. An approach to address this interference is to find experimentally, or by dynamic flow modelling, the location of minimum rotor interference on the body of a multi-rotor vehicle.

b) Multi-hole pressure probes (MHPP)

MHPPs use the same concept as Single hole Pitot tubes, but with additional holes due to which are able to produce 2D or 3D wind vector measurements. Pressure flow sensors, however, can only measure the sensor's facing direction. This concept is well suited for fixed-wing aircraft, but multi-rotors have more complex six-degree-of-freedom motion. The ability for omnidirectional motion makes it difficult to incorporate a directional-based sensor like MHPP on a multi-rotor UAV. Examples of using MHPP implemented on UAV are [99], [105], [106].

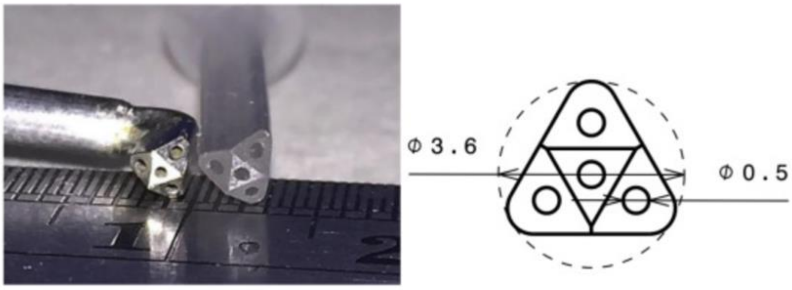

Figure 8: Cobra probe, Source: [106]

c) Ultrasonic anemometer: Time of flight theory

Ultrasonic anemometers are commonly seen in two types. First concept is called „Time-of-Flight"(ToF). Explanation of working principle is simply and clearly described in [107]. More detailed description is listed in U.S. Patent, Patent Number: 5,877,416 [108].

The sensor system emits an ultrasonic pulse through a transmitter or emitter and is able to determine the distance to a solid object (also known as the reflector) based on the time taken for the pulse to reverberate back to the emitter. The ultrasonic wavefield is affected by the fluid field.

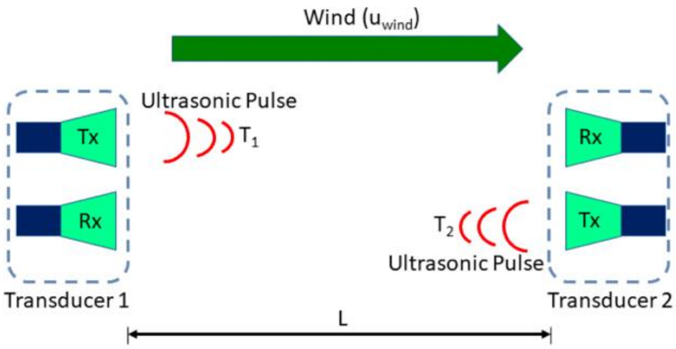

Figure 9: Working principle of ToF Ultrasonic anemometer [Source: DOI: 10.1109/ACCESS.2020.2977693]

An ultrasonic anemometer is equipped with multiple pairs of ultrasonic transducers placed at a fixed distance L. As depicted in Figure 9: Working principle of ToF Ultrasonic anemometer, each transducer contains two components: a Transmitter (Tx) and a Receiver (Rx). An ultrasonic pulse of the ultrasonic anemometer is sent from the Tx of Transducer 1 to the Rx of Transducer 2. The time between the transmission from Tx-Transducer 1 to Rx-Transducer 2 is measured. Next, a second pulse is transmitted from Tx-Transducer 2 to Rx- Transducer 1, and the time between this transmission and reception is measured.

In there is no wind occurring, these two time periods are equal for the path from Tx-Transducer 1 to Rx-Transducer 2 and Tx-Transducer 2 to Rx-Transducer 1. But, if the wind is observed, both these time measurements are different and the pulse traveling opposite to the direction of wind will take longer to reach the Rx component. The resulting time difference is subsequently used to estimate the wind speed and wind direction.

d) Ultrasonic anemometer: Acoustic resonance principle

The second sensor type of Ultrasonic anemometer is based on Acoustic resonance (Acu-Res) principle. This measurement system was invented by Dr Savvas Kapartis in 1999 (Date of patent: March 2nd, 1999, and Patent number: 5877416). Applicant of this patent is FT Technologies (UK) Ltd., who produces different types of sonic anemometers and one from their portfolio is FT-205. This light-weighted sensor is compact and suitable for UAV implementation. FT sensors were used within UAV research activities [109], [110].

Working principle of Acu-Res technology [111] is based on a pair of small parallel plates, referred to as the upper and lower reflector. In the horizontal direction, the structure is unbounded and air flows freely between the plates. In the vertical direction, it is bordered by reflectors. Acoustic waves are generated and received using three vibrating membranes connected to the same number of piezoelectric elements. In the Figure 10 is shown the arrangement of the Membranes in a triangular formation.

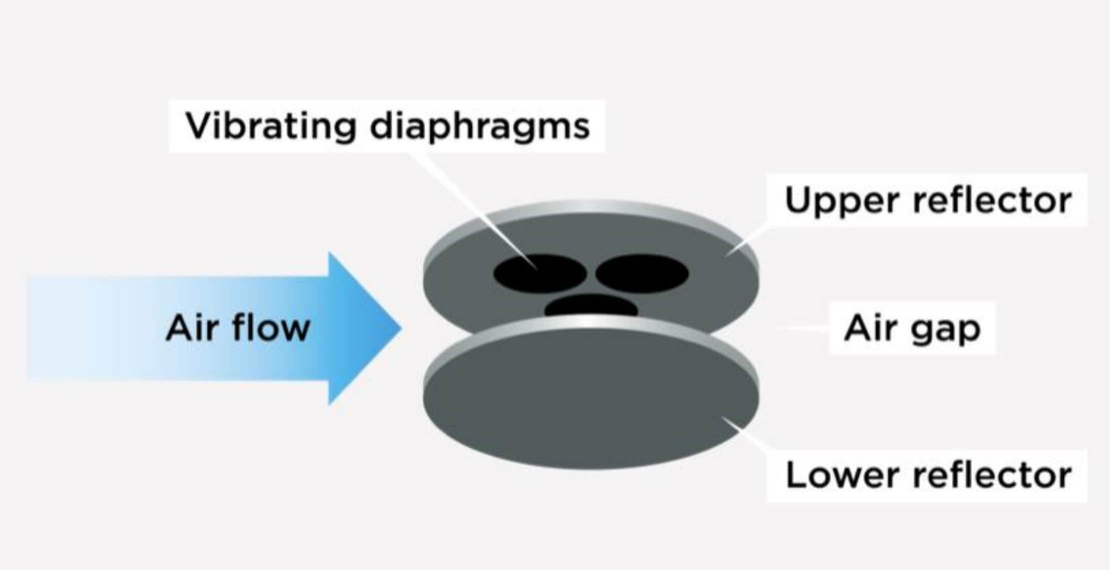

Figure 10: Acu-Res Working principle [Source: 111]

e) Summary of wind characteristics measurement techniques (direct approach)

Table 8: Advantages and disadvantages of different techniques for measuring wind characteristics

Measurement technique	*Advantages*	*Disadvantages*
Pitot-static tube	• Inexpensive device, • Light weight,	• Measure only wind speed, • Sensor placement is challenging (rotor wash), • Dependent on direction of airflow, • Require the use of several pitot-tubes (multi-rotor)
MHPP	• Inexpensive device, • Light weight	• Sensor placement is challenging (rotor wash), • can only measure the sensor’s facing wind direction (suited for fixed-wing UAV)
Sonic anemometer: Time of flight theory	• measure wind speed & direction, • Light weight • No moving parts, • Fast response	• Sensor placement is challenging (rotor wash), • higher purchase price, • sensitive to temperature and barometric pressure
Sonic anemometer: Acoustic resonance principle	• measure wind speed & direction, • Light weight, • independent of temperature and barometric pressure • No moving parts, • Fast response	• Sensor placement is challenging (rotor wash), • higher purchase price, • real-tie calibration needed

f) **Summary of representative studies focused on Wind characteristics estimation using sonic anemometer implemented in multi-rotor UAV**

Table 9: Brief summary of UAV mission using ultrasonic anemometer

Author	*Year*	*Type of ultrasonic anemometer*	*UAV platform*
Palomaki et al.	2017	Decagon Devices DS-2	DJI Flame Wheel F550 hexrotor
Donnell et al.	2018	TriSonica mini	Quadrotor
Shimura et al.	2018	FT702	hexarotor
Nolan et al.	2018	Atmos 22	DJI Inspire 2 quadrotor
Hollenbeck et al.	2018	TriSonica mini	Foxtech Hover1 quadrotor
Adkins et al.	2020	FT205	DJI S1000
Thielicke et al.	2021	Gill WindMaster	Quadrotor (COTS components)
Zhengnong et al.	2023	SA210	DJI M600PRO
Tianhao et al.	2023	WPOD	Quadrotor

Summarizing all previous research activities, it seems that use of ultrasonic anemometer is an ideal solution for drone-based wind measurement. The main disadvantage of this measurement technique is price that has a range from 1500 USD to 20 000 USD. This price range is associated with high-quality anemometers (sample sate 10 Hz and more). Considering my primary goal, which is to provide a low-cost solution that can be implemented by a wide range of users, high-quality anemometers are not an alternative for use in this research.

As was mentioned before, the ideal solution would be in the form of a software change without additional hardware equipment (indirect approach) and no extra expense for measurement technology. Part of this research is also to test an affordable device (direct approach) that cannot exceed the price range of a few hundred euros and must provide a low-cost solution as well.

A very important and key step was to summarize the previous research, the specifications of the ultrasonic devices used and the accuracy that was achieved. This information was used as the basic specifications in the search for an ultrasonic anemometer within affordable sensors.

Table 10: Accuracy of various ultrasonic anemometers

Sensor	**Author**	**Sample rate**	**Accuracy (Wind speed)**
DS-2	Palomaki et al. (2017)	1 Hz	0.27 – 0.67 m/s (wind speed 5 m/s)
Tri-Sonica Mini	Carl A. Wolf (2017)	10 Hz	1.13 m/s (wind speed up to 6.75 m/s)
FT-702	Shimura (2018)	1 Hz	0.6 m/s (wind speed up to 11 m/s)
Tri-Sonica Mini	Donnell (2018)	10 Hz	1.08 m/s
FT-205EV	Adkins (2019)	10 Hz	No information about accuracy. (Accuracy stated on the manufacture's website is ±0.3 m/s, for the wind speed up to 16 m/s)
SA-210	Zhengnong Li (2023)	1 Hz	0.29 m/s (3.81 % error at wind speed 7.57 m/s)

As the table clearly shows, for sufficient accuracy it is sufficient to use an ultrasonic anemometer with a sample rate of 1 Hz. The target group of the measuring technique of this research is focused on clearly defined specifics (lower sample rate) and not on high-quality anemometers for financial reasons. In chapter 5, a specific model of the measuring technique is presented.

5 EXPERIMENTAL WORK

5.1 PRELIMINARY NUMERICAL SIMULATION STAR-CCM+

Prior to the commencement of the demonstration mission, it was necessary to create a simulation of a turbulent environment within a built-up urban setting. This was done to identify where turbulent vortices arise near the Earth's surface and around obstacles commonly found in urban environments.

The numerical simulations were processed using STAR-CCM+ software, developed by Siemens. This computational fluid dynamics (CFD) software is utilized in various industrial sectors, including automotive, aerospace, energy, maritime, and others. The license and technical support for using the software were provided by IPSA - Institut polytechnique des sciences avancées, located in Paris, France. All the numerical simulations were conducted during my five-month internship in France, under the supervision of Mr. Wafik Abassi, who provided invaluable guidance throughout the project, from the initial planning stages to the analysis of the final results.

STAR-CCM+ employs the finite volume method to discretize and solve governing equations, such as the Navier-Stokes equations, to predict the behaviour of fluid flow and heat transfer within simulated geometries. The software encompasses a wide array of tools for pre-processing to create geometry and mesh, as well as post-processing tools for visualizing and analysing simulation results.

For this study, the chosen simulation geometry was a 3D CAD model containing a simple, clean-lined building and an adjacent fence, see Figure 11. The presence of two consecutive obstacles allows for the observation of whether there is an increase in swirling currents as air flows across multiple successive obstacles. The geometry also includes an integrated unmanned aerial vehicle in the form of a quadcopter, see Figure 12.

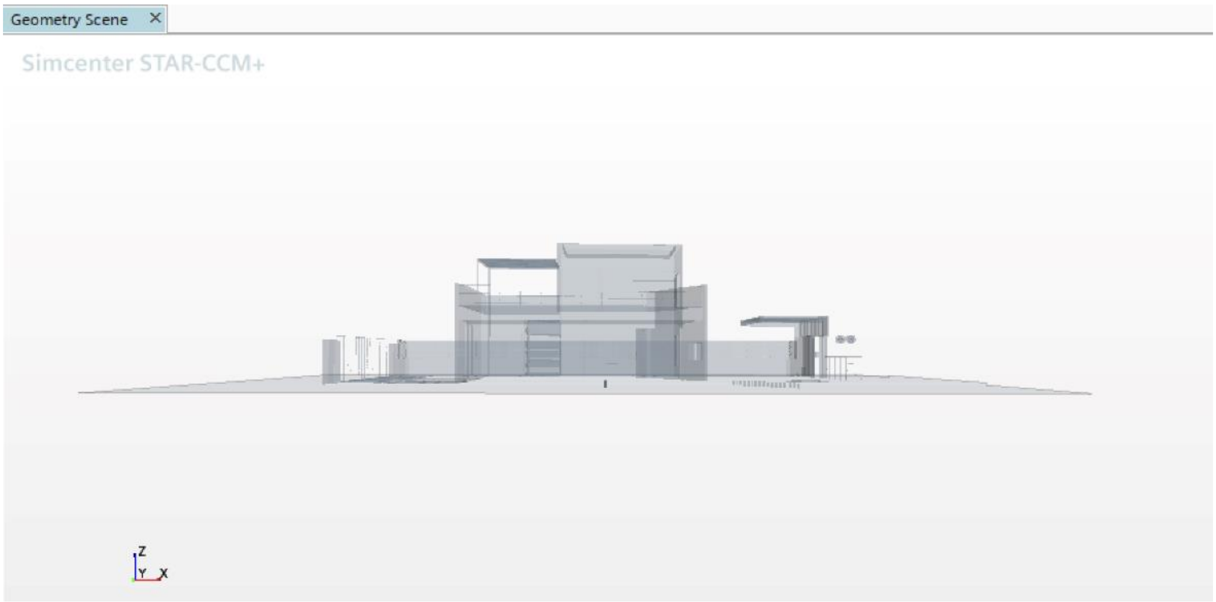

Figure 11: Basic simulation geometry including integrated quadcopter

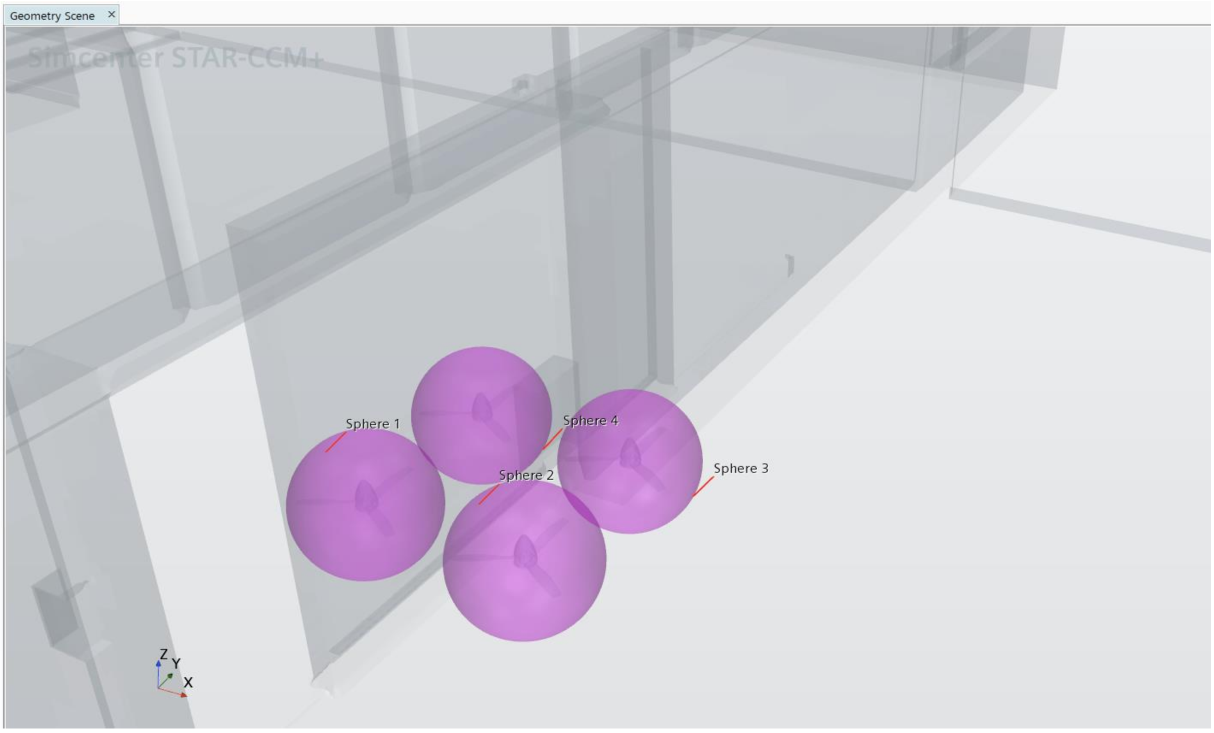

Figure 12: Detailed view of the integrated unmanned aerial vehicle.

After importing the basic geometry, it was necessary to create a mesh that discretizes the geometry into small computational cells. The quality of the mesh is crucial for accurate results. In this study, 5 meshes were used. Meshes 1 to 4 around the individual rotors of the unmanned vehicle were manually set to a resolution of 0.003 m, and the spatial mesh labelled number 5 was set to a resolution of 0.1 m. In addition to the initial manual mesh setup, an automated mesh refinement tool was used. Figure 13 shows a detailed view of the final mesh scene of the study.

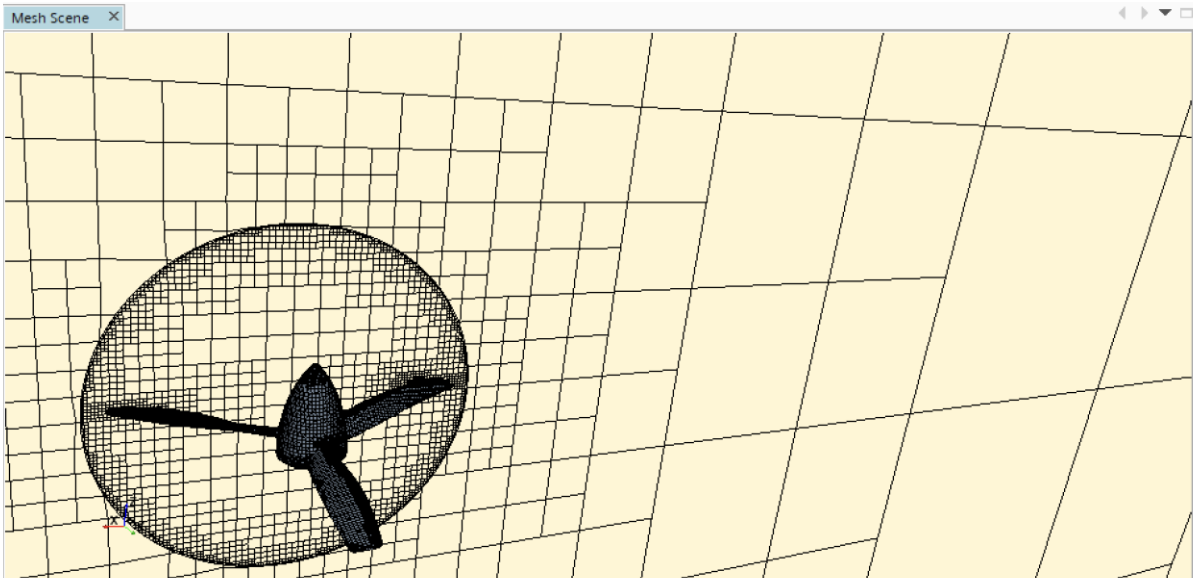

Figure 13: STAR-CCM+ Mesh Scene

The next step was to define the physics of the problem, including fluid properties, boundary conditions, and the turbulence model. For the turbulent simulations, a set of 16 input models was chosen, the exact wording of which is attached in Figure 14.

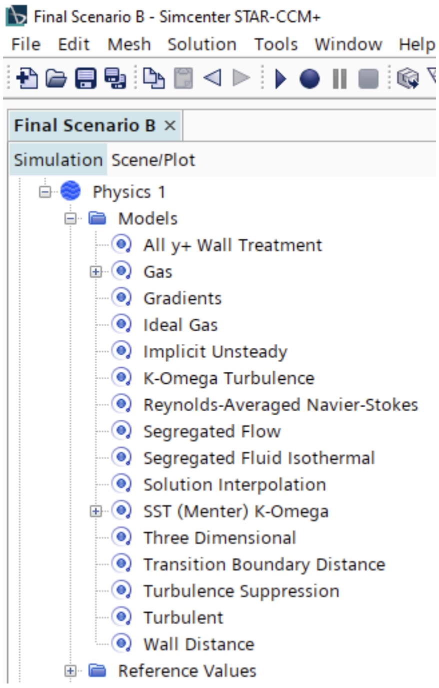

- Physics 1
  - Models
    - All y+ Wall Treatment
    - Gas
    - Gradients
    - Ideal Gas
    - Implicit Unsteady
    - K-Omega Turbulence
    - Reynolds-Averaged Navier-Stokes
    - Segregated Flow
    - Segregated Fluid Isothermal
    - Solution Interpolation
    - SST (Menter) K-Omega
    - Three Dimensional
    - Transition Boundary Distance
    - Turbulence Suppression
    - Turbulent
    - Wall Distance
  - Reference Values

Figure 14: Set of input physical models

The next step was to configure the solver settings, which involves configuring various settings related to the numerical solver used to solve the governing equations of fluid flow and turbulence models. Key solver settings include time step, convergence criteria, numerical settings, and others. Table 11 shows the basic solver settings.

Table 11: Solver Settings of the Case Study Processed in STAR-CCM+ Software

Key aspects	Setting
Time stepping scheme	Implicit Unsteady
Time step	0.001 s
Under-relaxation factor (K-Omega Turbulence)	0.8
Under-relaxation factor (K-Omega Turbulent Viscosity)	1.0
Maximum inner iterations	5
Maximum physical time	0.4 s
Maximum steps	1000

An important input criterion is also the setting of reference environmental values, which in the case study were chosen as standard atmospheric pressure, i.e. 101,325 Pa, wind speeds from 10 m/s to 20 m/s, and wind directions of 90°, 180°, and 270°. After completing all initial settings, the simulation is started, which takes approximately 24 hours (depending on the technical equipment). After the simulation is completed, predefined scenes displayed on selected plane cuts are made available. The main observed parameter is the dissipation rate, and its visualization is shown in the following Figure 15, Figure 16 and Figure 17.

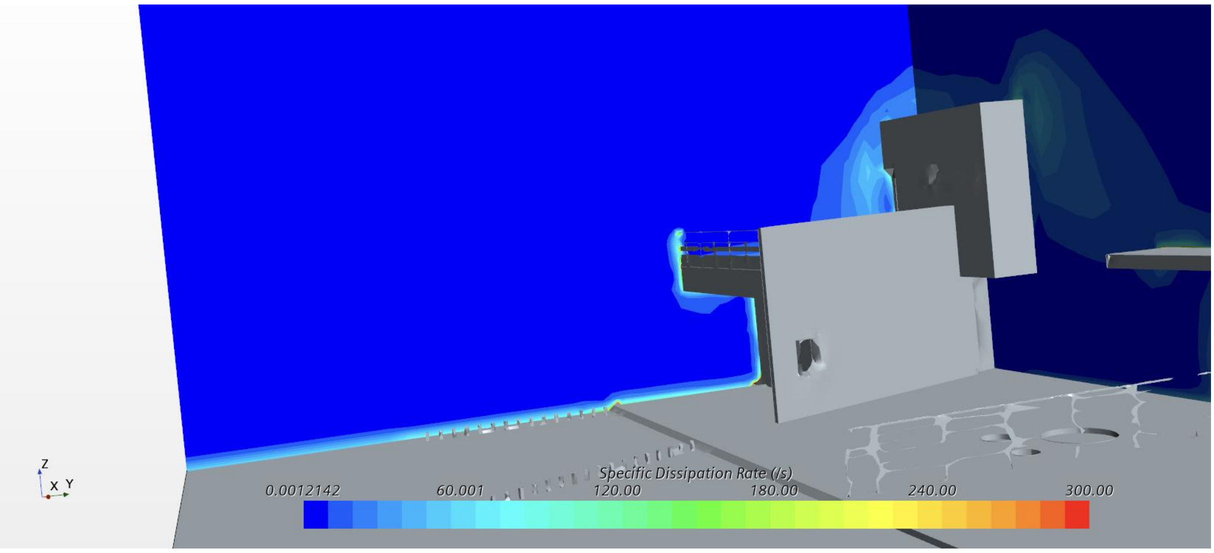

Figure 15: Detailed shot capturing the ground effect (wind speed 10 m/s, wind direction 270°)

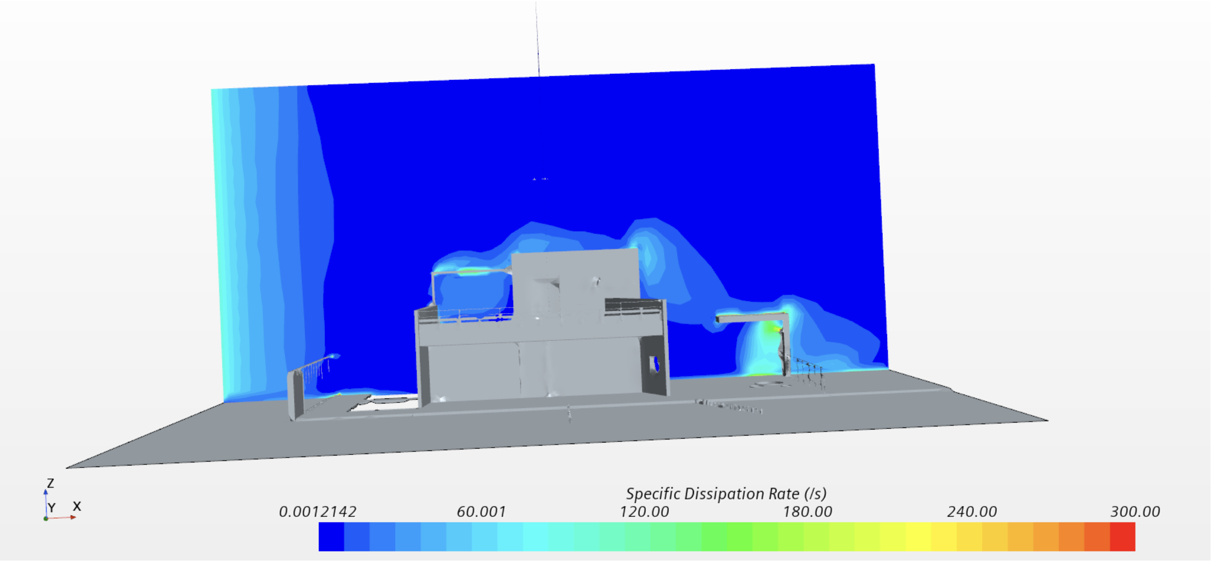

Figure 16: Eddy current dissipation rate (wind speed 10 m/s, wind direction 270°)

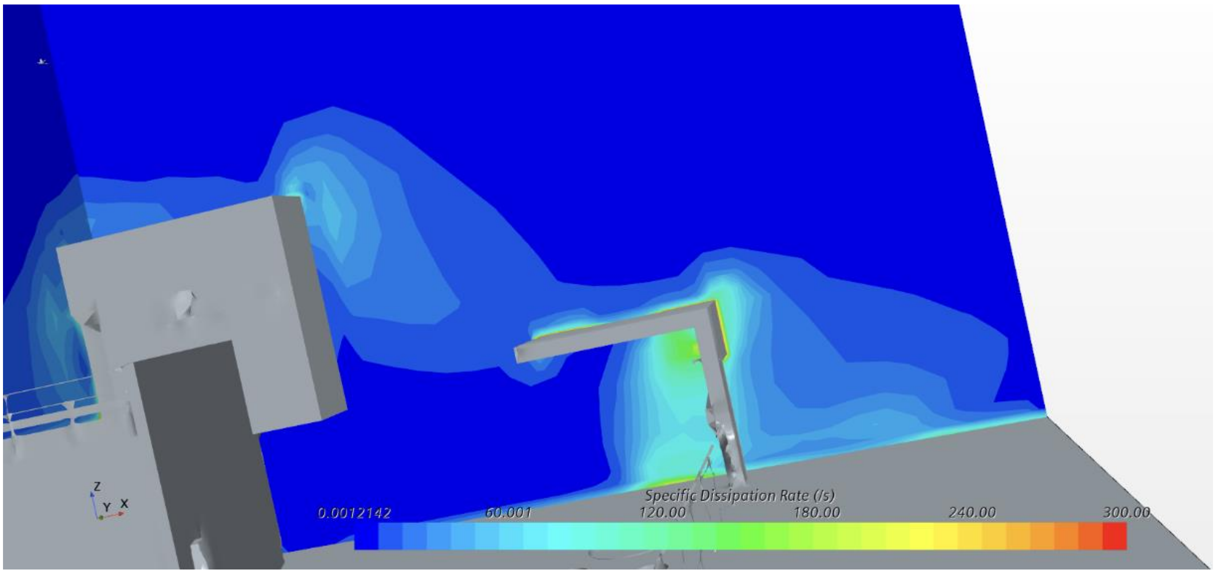

Figure 17: A close-up shot showing the eddy currents around two consecutive obstacles (wind speed 10 m/s and wind direction 270°)

5.1.1 Initial results

The numerical simulations, conducted using Star CCM+ software, aimed to identify the locations and magnitudes of turbulent vortices generated in the vicinity of the building. This detailed information is crucial for planning UAV flight paths, enabling us to design flight patterns that expose UAV to the turbulent flow field for measurement and analysis.

While the software initially proved adequate for preliminary numerical simulations, frequent errors and a less-than-optimal user experience were encountered. However, the primary motivation for transitioning to a more suitable software alternative in subsequent phases of this research stemmed from significant limitations in the software's domain capabilities. Although simulations for a single building were feasible, the software's constraints precluded the analysis of more complex scenarios, which was essential for the specific objectives of this investigation. Consequently, in the second phase of the study, the software was replaced with ENVI-met, which proved to be far more suitable for the specific requirements of this research.

5.2 PRELIMINARY TEST FLIGHTS – BRNO

For the calculation of the EDR algorithm, it was recognized that detailed information regarding wind characteristics, real-time data measured by the UAV, was necessary. Two alternatives were identified: direct and indirect measurement. Direct measurement necessitates the integration of an additional sensor to capture and log wind data for subsequent analysis. Conversely, indirect measurement involves deriving wind speed and direction from the UAV's behaviour, including its 3-axis attitude, rotor RPM, and rotor thrust.

To evaluate the feasibility of each approach, two types of measurements were conducted: indoor and outdoor tests. The results of these tests informed the selection of the most suitable alternative for further investigation.

5.2.1 Indoor hover test

Following the analysis of numerical simulations and the identification of locations where turbulent vortices occur, which could potentially compromise UAV safety, the subsequent research phase involved testing the UAV's behaviour under various load conditions with wind speeds reaching 12 m/s. Due to the UAV's size, testing in a traditional wind tunnel was not feasible. Therefore, a pseudo wind tunnel concept was developed and implemented within the C3a test room at the VUT campus.

The pseudo wind tunnel consisted of a Siemens propeller wind generator (Figure 19), which was operated in 17 distinct modes, each lasting 60 seconds, for a total test duration of 17 minutes. Testing in mode 17 was prematurely terminated due to the onset of instability. Throughout the testing procedure, the UAV was maintained in a stabilized hover mode.

Wind speed measurements were acquired using a “Laserline” anemometer, the data from which is presented in Figure 18. During the initial phase of testing, the average wind speed exhibited a linear increase. However, the latter half of the test period revealed various anomalies attributed to imperfections in the pseudo wind tunnel setup. At maximum power output, the mean wind speed reached 8.8 m/s, with peak values reaching 11.8 m/s.

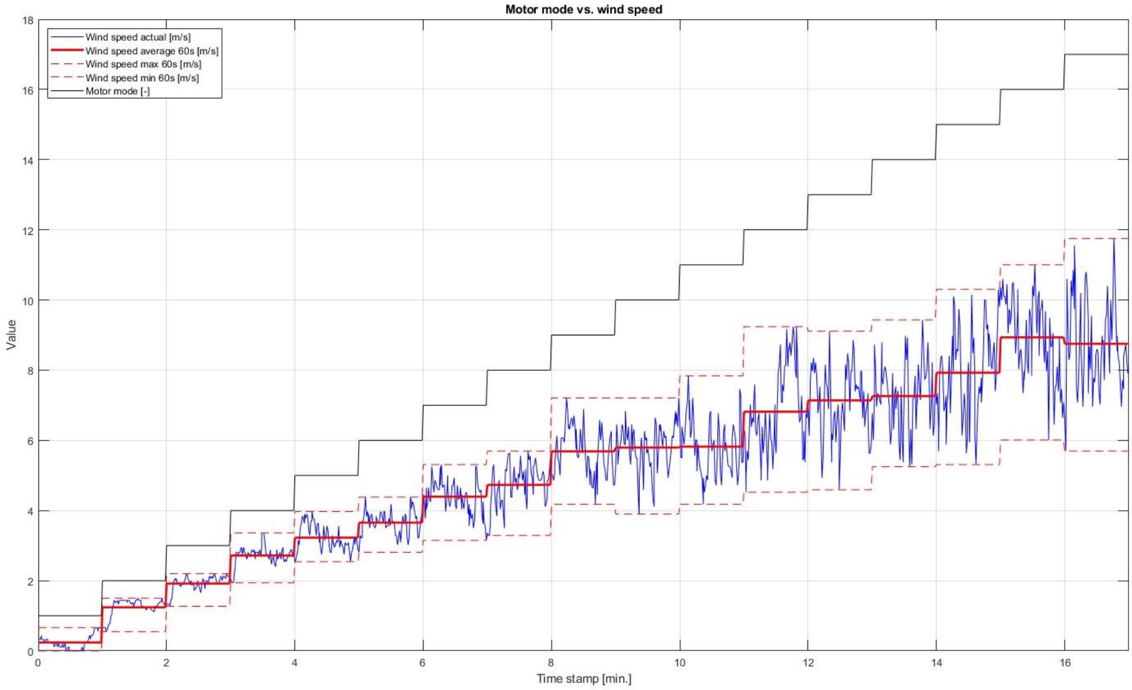

Figure 18: Indoor hover test – 17 test modes and their corresponding wind speeds

For this experiment, a DJI Phantom 3 Advanced UAV was positioned 5 meters from the Siemens propeller wind generator. Data, including motor thrust for each rotor (LF, RF, LB, and RB) and drone attitude in all three axes (pitch, roll, and yaw), were recorded and stored using the onboard DJI data logger.

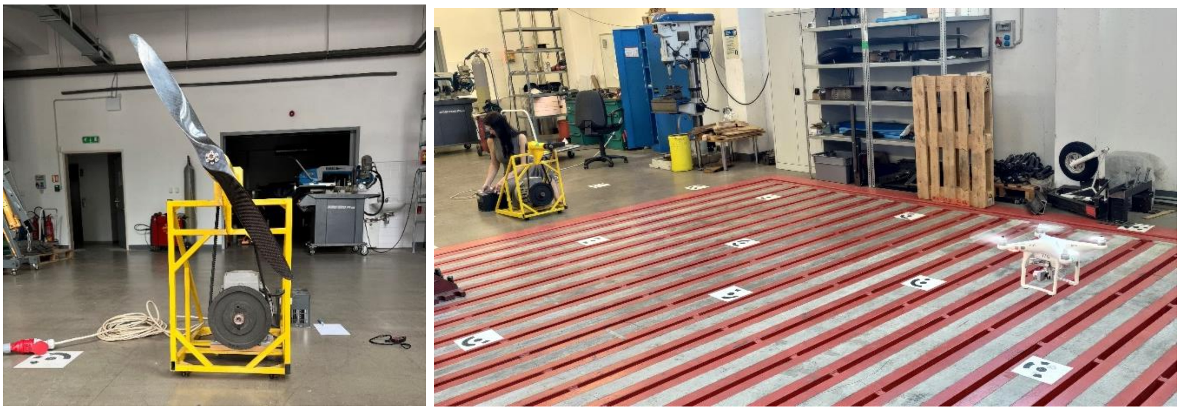

Figure 19: Indoor hover test – Siemens propeller wind generator

Figure 18 illustrates the progression of the test flight up to mode 14. This section of the test is crucial for future research as it achieves the manufacturer's specified maximum wind speed tolerance of 10 m/s for safe UAV operation. With increasing wind speed, the rotation rates of the front and rear motors adjust, and the pitch angle gradually decreases to approximately -7°. This negative pitch allows the UAV to utilize the increased airflow over its rotors to generate additional lift, counteracting the force of the wind and maintaining a stable hover at the desired location.

The total thrust (sum of all motors) is shown in the third graph. It might be expected that with increasing wind, the motor thrust would increase, as the drone needs to both resist the wind and compensate for its weight. However, the graph demonstrates a counterintuitive phenomenon: the total thrust actually decreases with increasing wind speed. This is because the UAV's negative pitch angle [115] enables it to harness the wind's energy to generate lift, reducing the need for the motors to provide as much vertical thrust. In essence, the drone becomes more aerodynamically efficient in the presence of wind, leading to a reduction in overall power consumption.

The primary outcome of this initial test is the verification of the drone's behaviour and controllability in an environment with wind speeds up to 10 m/s. This understanding is essential for the next research phase, which involves flight in windy conditions near obstacles.

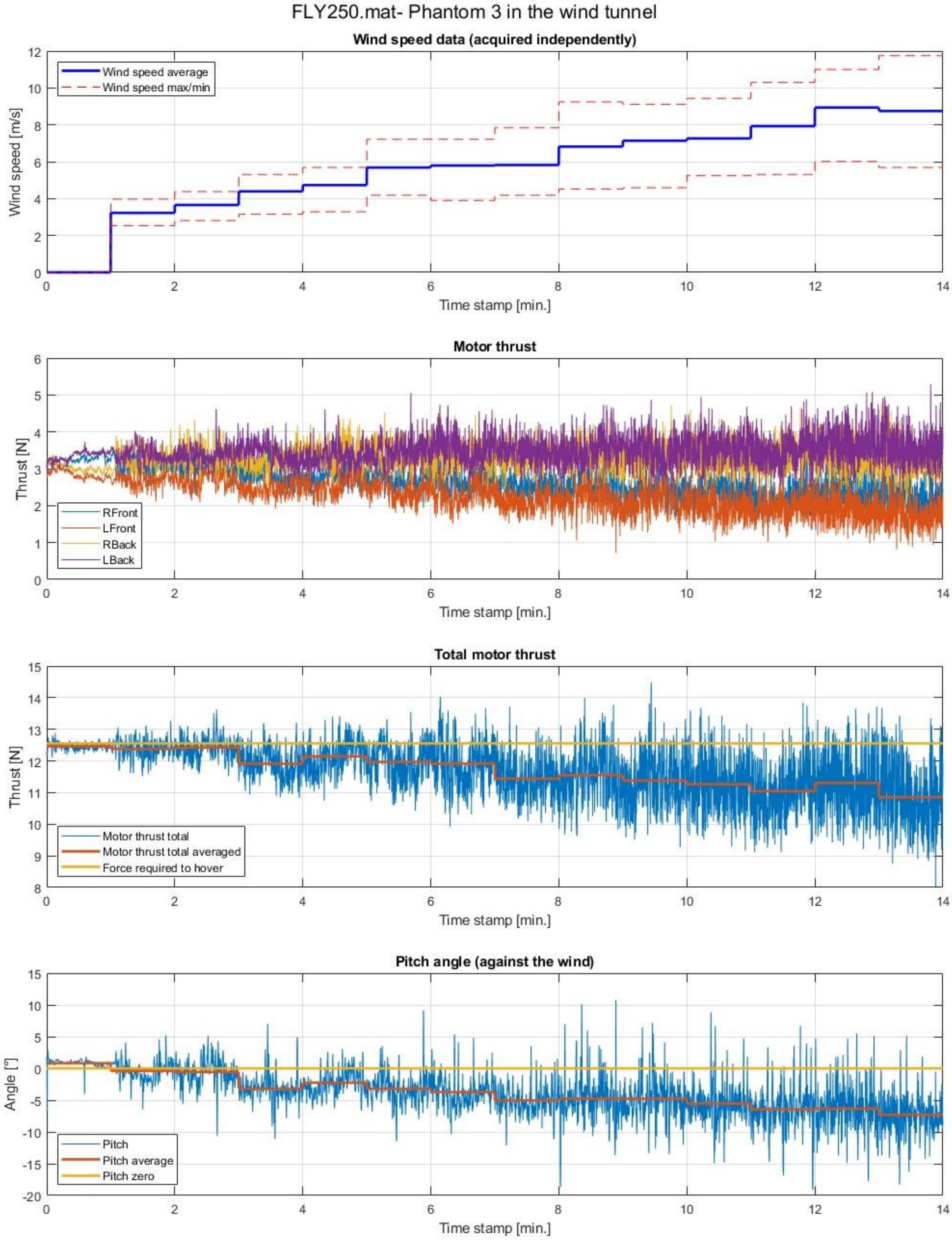

Figure 20: Indoor hover test - Parameters monitored to understand UAV behaviour

5.2.2 Outdoor hover test

All outdoor UAV flights conducted as part of this research were performed within the Brno University of Technology (BUT) campus, in accordance with permission granted by the Civil Aviation Authority (CAA) under authorization number OKPUAS-1268. This authorization permits the operation of unmanned aerial systems within specific geographical zones defined by the CAA. A graphical representation of the 16 approved locations is provided in Figure 21.

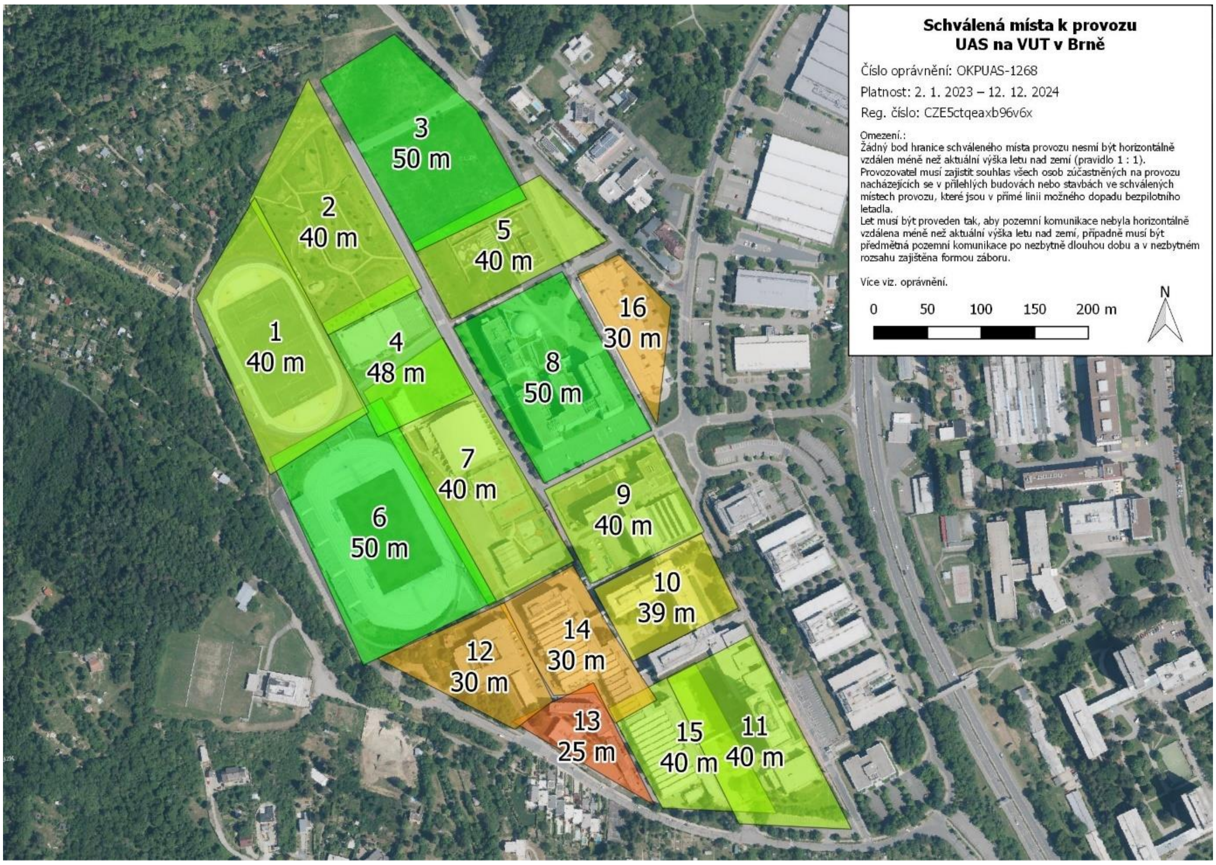
Schválená místa k provozu UAS na VUT v Brně

Číslo oprávnění: OKPUAS-1268

Platnost: 2. 1. 2023 – 12. 12. 2024

Reg. číslo: CZE5ctqeaxb96v6x

Omezení.:
Žádný bod hranice schváleného místa provozu nesmí být horizontálně vzdálen méně než aktuální výška letu nad zemí (pravidlo 1 : 1).
Provozovatel musí zajistit souhlas všech osob zúčastněných na provozu nacházejících se v přilehlých budovách nebo stavbách ve schválených místech provozu, které jsou v přímé linii možného dopadu bezpilotního letadla.
Let musí být proveden tak, aby pozemní komunikace nebyla horizontálně vzdálena méně než aktuální výška letu nad zemí, případně musí být předmětná pozemní komunikace po nezbytně dlouhou dobu a v nezbytném rozsahu zajištěna formou záboru.

Více viz. oprávnění.

Figure 21: Approved locations for UAV operation within the BUT campus

A) Flight scenario "approach towards obstacle"

The initial flight aimed to assess the drone's behaviour during a gradual approach towards a building facade. The objective was to determine the minimum safe distance to the facade, ensuring no hazardous situations arose. The test flight commenced in a meadow within the VUT campus under calm/ideal weather conditions, followed by a controlled approach towards the nearest building. The UAV pilot was able to manoeuvre the drone as close as 1 meter from the building facade without encountering any difficulties. The flight trajectory, along with the monitored parameters, are illustrated in Figure 22 and Figure 23.

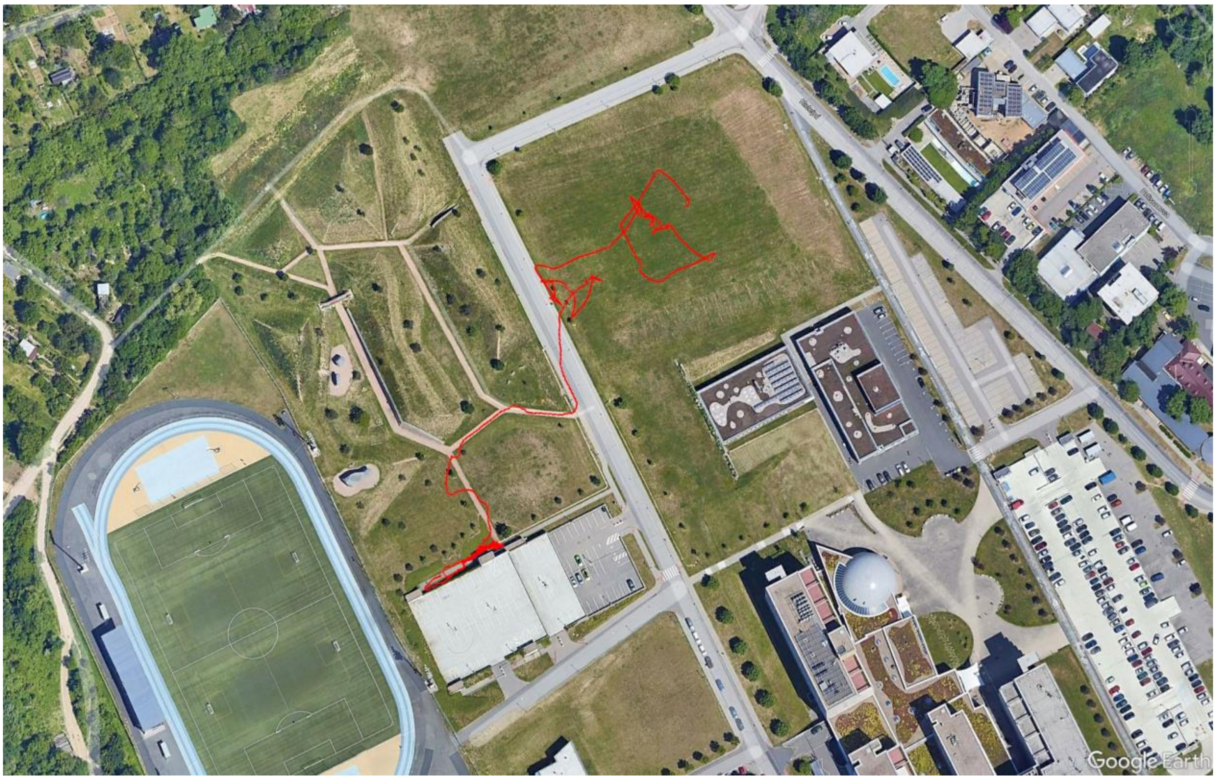

Figure 22: UAV flight trajectory (red colour) within BUT Campus

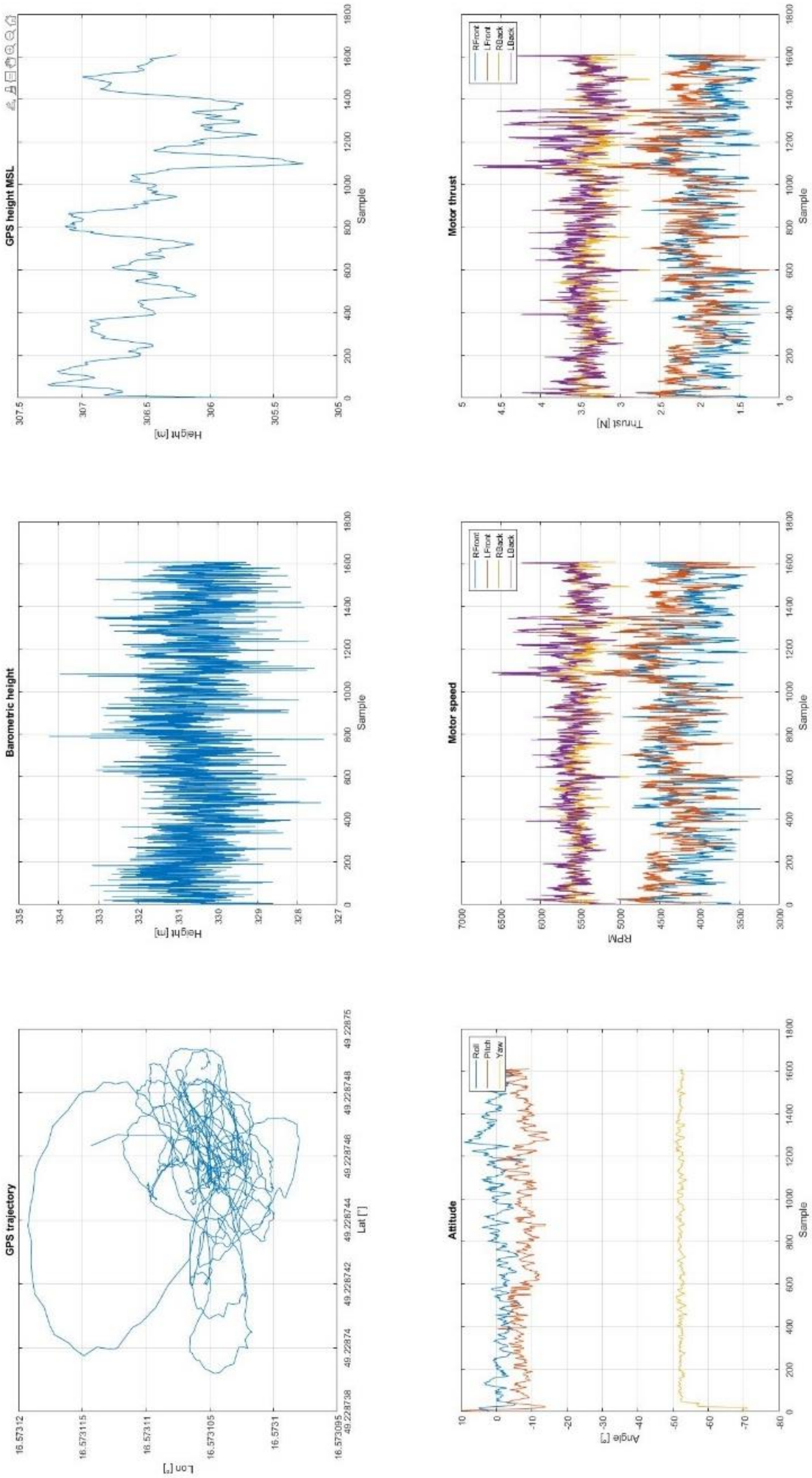

Figure 23: Basic analysis of UAV manoeuvrability and stability during testing flight

B) Flight performed at very close distance to the building (2 m)

Having established the drone's stability and safety during approached flight in proximity to obstacles, the subsequent research phase aimed to achieve two distinct objectives. The first objective was to further assess the drone's stability, manoeuvrability, and safety, specifically in hover mode at close distances to a building. The second objective was to prepare a reliable ground reference for the upcoming AdMaS demonstration mission.

Location of conducted flights was within zone 12 of the BUT campus, see Figure 21: Approved locations for UAV operation within the BUT campus. Testing concept was systematically varying the drone's hover altitude and distance from a designated building. This meticulous approach allowed for a comprehensive evaluation of the UAV's performance in challenging environmental conditions.

Concurrently, the Davis Vantage Pro2 meteorological station (see Figure 24) was deployed as the designated ground reference. This research-grade station, renowned for its ability to provide high-precision meteorological data, was rigorously tested to ensure its accuracy, data logging capabilities, and seamless data export functionality. The station was configured to capture a wide range of parameters, including real-time wind speed (up to 90 m/s), temperature, humidity, barometric pressure, rainfall, heat index, dew point, and high/low values.

This ground meteorological station will serve as a basic reference to verify the values of ENVI-met numerical simulations and sensors additionally integrated on the UAV during the AdMaS mission.

Figure 24: Preliminary concept of hover test with Davis meteorological station

5.2.3 Initial results

During both indoor and outdoor tests, the drone's behaviour and controllability were monitored. Indoor testing confirmed that the drone began to exhibit instability as wind speeds approached 10 m/s. (Testing was conducted within non-destructive limits; therefore, when increased control difficulty was observed, the test was terminated to prevent potential damage to the UAV. The absolute stability limit of the UAV was not tested.)

Subsequent data analysis revealed a primary challenge: exporting the required parameters. Modern UAVs, such as the Mavic 2, restrict access to motor RPM and thrust data. Older models, like the DJI Phantom 4, permit such data export and were therefore utilized, despite their technological limitations.

Given the objective of developing a solution applicable to a wide range of UAVs, including commercial models, it is imperative to identify readily deployable tools. Implementing indirect measurement on modern drones is problematic due to limitations on exported data. While the analysed data provided insights into basic drone behaviour and the influence of prevailing winds, deriving precise wind speed and direction necessitates complex algorithms and data that were unfortunately inaccessible within the constraints of the available UAV fleet.

Based on these findings, the direct measurement method was deemed preferable. This approach involves a low-cost concept for integrating an additional sensor onto the UAV.

Direct measurement, although requiring the addition of a sensor, offers several advantages that contributed to its selection in this research:

- **Accuracy & Reliability:** Direct measurement of wind parameters using a dedicated sensor generally provides more accurate and reliable data compared to indirect methods that rely on estimations and complex algorithms.
- **Simplicity & Robustness:** Direct measurement eliminates the need for intricate calculations and modelling, making the approach simpler and less prone to errors.
- **Compatibility:** Direct measurement is compatible with a wider range of UAVs, including modern models that restrict access to flight controller data required for indirect methods.

In contrast, indirect measurement, while potentially appealing due to its non-intrusive nature, faces challenges related to data availability, algorithm complexity, and model accuracy, particularly in the context of modern UAVs.

The decision to prioritize direct measurement reflects a pragmatic approach that balances the need for accurate wind data with practical considerations of implementation and compatibility across various UAV platforms.

5.3 NUMERICAL SIMULATION – ENVI-met

The initial phase of numerical simulations, utilizing Star CCM+, effectively identified localized turbulent vortices in the building's vicinity, providing crucial data for UAV flight path planning and subsequent data collection within the turbulent flow field. However, the software encountered limitations, including frequent errors and a suboptimal user experience. More critically, Star CCM+'s domain capabilities were insufficient for modelling the larger and more intricate AdMaS campus environment, a key requirement for the subsequent research phase.

Given that the primary research objective was to determine safe UAV operating distances near buildings, a highly detailed mesh resolution (in centimetres) was not essential. ENVI-met's 1-meter grid resolution was deemed adequate for this purpose. Moreover, ENVI-met established track record in similar research, along with its user-friendly interface and capacity to handle large-scale simulations without errors, solidified its selection as the preferred software for the second phase of this investigation.

To assess the impact of buildings on the formation of turbulent phenomena that could negatively affect UAS operations and thus obtain useful quantitative information for developing safety guidelines, a series of numerical simulations were conducted. These simulations focused on two distinct scenarios: the first involved stand-alone buildings of varying heights (from 5m up to 20 m) under different undisturbed wind speed conditions (from 2 m/s up to 10 m/s) but with constant wind direction, in order to obtain quantitative information about the size of the dangerous zones for the UAS flight and to define two equations to predict their size. The second examined a section of the AdMaS Centre - Brno University of Technology (Brno, Czech Republic), during typical spring-summer atmospheric conditions, for two main reasons: to validate the quantitative information, obtained from stand-alone building simulations, about the dangerous zones for UAS flight around buildings in a real-world scenario, and to obtain a model to be compared with the real-time turbulence data collected during UAS flights in the summer of 2024.

Both scenarios were simulated using ENVI-met, (Version 5.6.1, ENVI_MET GmbH, Essen, Germany, Bruse and Fleer, 1998) a holistic three-dimensional non-hydrostatic model designed for simulating surface-plant-air interactions [116]. Grounded in the fundamental principles of Fluid Mechanics, Thermodynamics, and Atmospheric Physics, ENVI-met possesses the capability to compute, inter alia, three-dimensional wind fields, turbulence, air temperature, and humidity. In particular, the spatial and temporal evolution of the wind field is calculated by applying the non-hydrostatic three-dimensional Navier-Stokes equation, and turbulence is parametrized using a $E - \varepsilon$ 1.5 order closure model. The $E - \varepsilon$ model basically consists of two prognostic equations, one describing the production of turbulent kinetic energy (TKE) and the other its dissipation. In contrast to first order closure models, the $E - \varepsilon$ model allows the simulation of advective processes in horizontally inhomogeneous environments without as much computation time as closure models of higher order [117].

According to Fabbri K. [118], ENVI-met is the most widely used software for simulating the urban outdoor microclimate. However, despite some inherent limitations due to the discretization of the domain and to the approximations introduced by the numerical solution of complex equations typical of this kind of software, the ability to investigate wind fields and the turbulence potentially generated when interacting with obstacles of different natures (i.e., buildings and vegetation) in a context where it is possible to replicate daily variations in sun position and the meteorological conditions of a user-selected day, makes ENVI-met a suitable tool even for pursuing objectives beyond microclimatic analyses, as in the case of the present study and in particular for the second scenario, which involved modelling an existing area including buildings and various types of vegetation and soil.

The scientific license for the ENVI-met software was provided by UNICA (Università degli Studi di Cagliari). The preparatory phase and the entire numerical simulations were processed under the guidance of prof. Simone Ferrari and Alessandro Santus.

5.3.1 Single building scenario

A comprehensive set of numerical simulations was conducted to assess the size and location of hazardous zones for Unmanned Aircraft Systems (UAS) operations in the vicinity of stand-alone buildings. The simulations examined a range of building heights, from 5 meters to 20 meters, and considered the effects of varying meteorological conditions, with undisturbed wind speeds spanning from 2 m/s to 10 m/s. The primary objective of this study was to characterize the spatial extent of dangerous areas resulting from flow detachment phenomena induced by the interaction of wind with the built environment. Specifically, the investigation focused on the two most dangerous zones around the building and characterized by a strong change in the wind flow due to the interaction with the building.

The first one is the building downstream wake (a zone characterized by downstream wake distances, low wind speeds and altered flow patterns with shifting wind directions due to wake vortices): This region of significantly reduced wind speed and altered wind direction, located directly behind the building, poses a risk due to the abrupt changes in aerodynamic forces experienced by the UAS.

The second one is the vertical updraft zone, located above the building rooftop, which appear as strong upward airflows near the upstream edges of buildings that can cause undesirable lift, potentially leading to loss of control or collisions.

As above stated, the ENVI-met software was employed to model the intricate dynamics between wind flow and building geometry. Multiple simulation scenarios were executed, systematically varying building height and wind speed to capture the diverse range of potential flow field configurations. The spatial domain for each simulation was carefully tailored to the specific dimensions of the building under investigation, ensuring the flow reattachment inside the domain and, consequently, a representative and accurate simulation environment (see Table 12). A uniform grid cell resolution of 1 m x 1 m x 1 m was maintained across all simulations.

For each simulation, the date and time were consistently set to April 15th, 2024, at 7:00 AM, with a total simulation duration of 5 hours. Meteorological parameters were established using a simple forcing method with a 24-hour cycle and automatic linear interpolation. The minimum and maximum temperatures were set to 18° Celsius and 28° Celsius, respectively, while the minimum and maximum relative humidity values were 45% and 75%, respectively. Wind direction was consistently oriented to the North, as determined by a thorough analysis of wind rose data for the AdMaS centre. Wind speeds of 2, 4, 6, 8, and 10 m/s were selected for each building height, resulting in a total of 20 numerical simulations, each dedicated to exploring a single building scenario under varying wind conditions. Figure 25 illustrates an example of the velocity field (the colours highlight the magnitude, while the vectors both the magnitude and the direction) in a vertical section in the centre of a single building, obtained as output for a 10 m x 10 m x 20 m building subjected to a 10 m/s wind, at 12:00.

The downstream wake distance is defined as the downstream distance, at the ground level and measured in a vertical section of the velocity field in the middle of the building (see Figure 25), between the building and the cell where the wind speed exceeds 25 % of starting wind speed (so, for example, in simulations with a wind speed of 10 m/s, the downstream wake zone is the zone starting from the downstream wall of the building and ending where the velocity is higher than 2.5 m/s). The measurement at ground level is needed because, for the UAS safety, also the take-off and landing need to be done in a safe zone. The downstream wake distance has been measured for each simulated case and its values are shown in Figure 26, versus the building height, for each wind. The downstream wake distance, even if with some fluctuations, tends to increase when the building height and the wind speed increase. The downstream wake zone, which can be defined as the whole zone downstream the building inside the downstream wake distance, should be avoided for UAS operations.

The vertical updraft distance is also measured in a vertical section of the velocity field in the middle of the building and is defined as the distance between the upstream upper corner of the building and the first cell where the velocity vectors become again horizontal. The vertical updraft distance has been measured for each simulated case and its values are shown in Figure 27, versus the building height, for each wind. Similarly, to the downstream wake distance, the vertical updraft distance tends to increase when the building height and the wind speed increase. The vertical updraft zone, which can be defined as the whole zone above the building rooftop inside the vertical updraft distance, should be avoided for UAS operations as well.

Building size (width, length, height)	Domain size	Wind speed
10 m x 10 m x 5 m	60 m x 85 m x 25 m	2,4,6,8 and 10 m/s
10 m x 10 m x 10 m	110 m x 160 m x 50 m	2,4,6,8 and 10 m/s
10 m x 10 m x 15 m	160 m x 235 m x 75 m	2,4,6,8 and 10 m/s
10 m x 10 m x 20 m	210 m x 310 m x 100 m	2,4,6,8 and 10 m/s

Table 12: Summary of all testing domains (ENVI-met, Single building scenario)

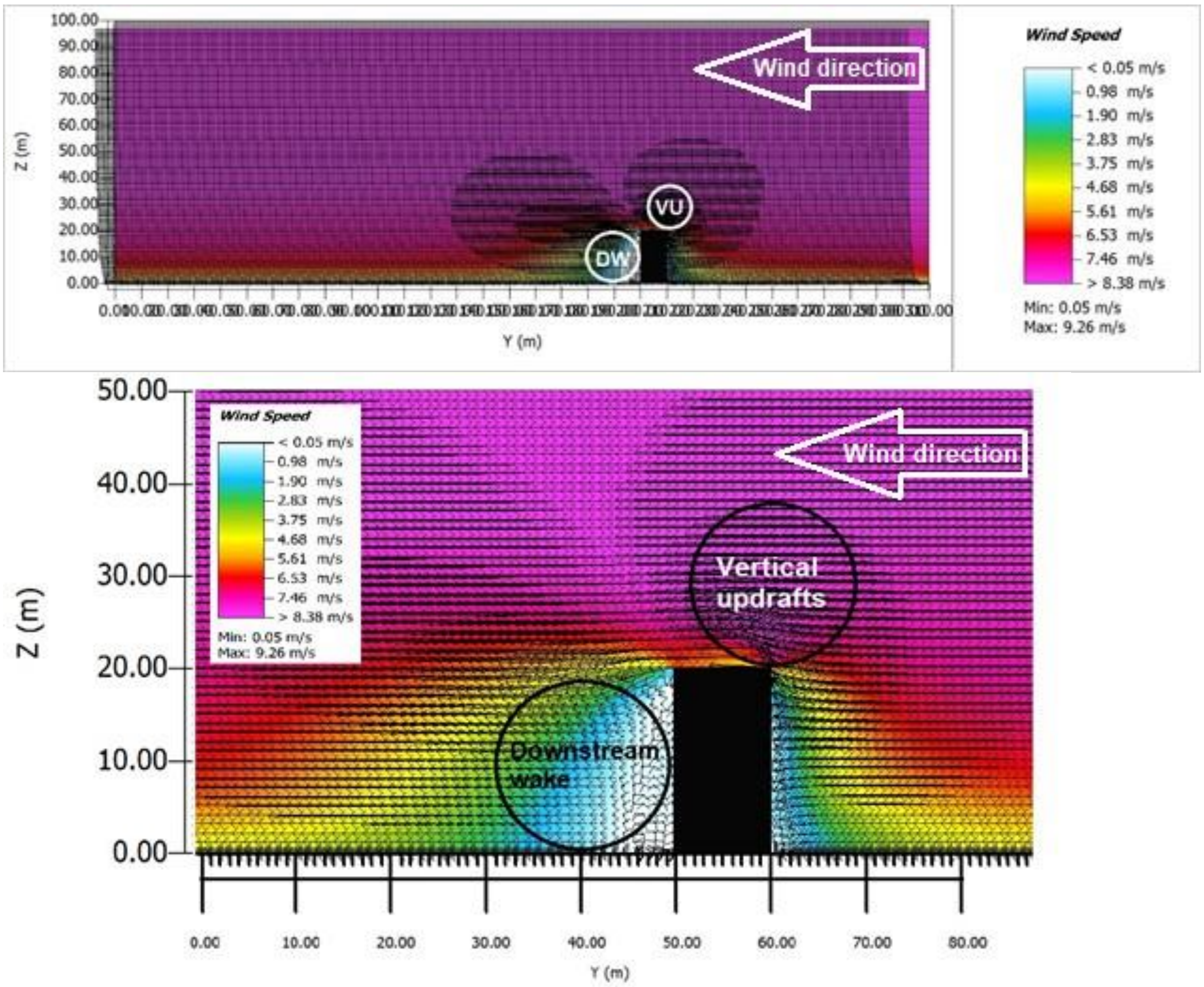

Figure 25: example of the velocity field in a vertical section in the centre of a single building, obtained as output of numerical simulation for a 10 m x 10 m x 20 m building with a 10 m/s wind speed; below, a zoom close to the building to highlight the dangerous

The data presented in Figure 26, depicting the relationship between building height (BH), wind speed (WS), and the extent of the downstream wake (DW) hazardous zone, was meticulously analysed to establish a mathematical relationship between these parameters. This analysis aimed to provide a practical equation for estimating the size of the dangerous zone for UAS operations, contingent upon wind velocity and building height.

Based on the simulation results, a formula (equation 24) was empirically derived to estimate the downstream wake distance (DW), recognizing it as a function of both building height (BH) and wind speed (WS). The formula takes the form of a power-law relationship, incorporating two distinct components: a scale parameter and a shape parameter (DW = scale parameter * shape of parabola).

The DW scale parameter, represented by the expression (k_{1DW} + k_{2DW} * (WS)), accounts for the overall size of the downstream wake.

a) Constant Term, k_{1DW} = 5.8, which establishes a baseline wake length that persists even in minimal wind conditions. It reflects the inherent turbulence and flow disruption introduced by the building's presence.

b) Wind Speed Coefficient, $k_{2DW} = 0.19$, this coefficient modulates the wake length in response to variations in wind speed (WS). Stronger winds impart greater momentum and energy, causing the wake to elongate. The coefficient quantifies this effect, ensuring that the wake expands proportionally with increasing wind velocity.

The DW shape parameter, denoted by BH1/3, dictates the geometric form of the wake, approximating it as a parabola.
Building Height Exponent signifies that the downstream wake length grows with the cube root of the building height (BH). Taller buildings generate larger, more pronounced wakes, and this exponent captures the non-linear growth observed in the simulation data.

The constants $k_{1DW} = 5.8$ and $k_{2DW} = 0.19$ were determined through an iterative optimization process, refining the formula to minimize the average prediction error across the entire dataset. The resulting equation:

$$DW = (k_{1DW} + k_{2DW}\,(WS))*(BH)^{1/3} \qquad \text{Equation 24}$$

achieves a high degree of accuracy, with deviations from the simulated data consistently below 5%.

Figure 26 provides a visual representation of the formula's implications. The five distinct curves illustrate the dependency between building height (ranging from 5m to 20m) and wind speed (ranging from 2 m/s to 10 m/s), showcasing how the wake length expands with both increasing building height and wind speed. The two dashed lines, representing the minimum (2 m/s) and maximum (10 m/s) wind speeds, effectively delineate the overall trend of wake length growth across the entire range of wind velocities, as predicted by the derived Equation 24.

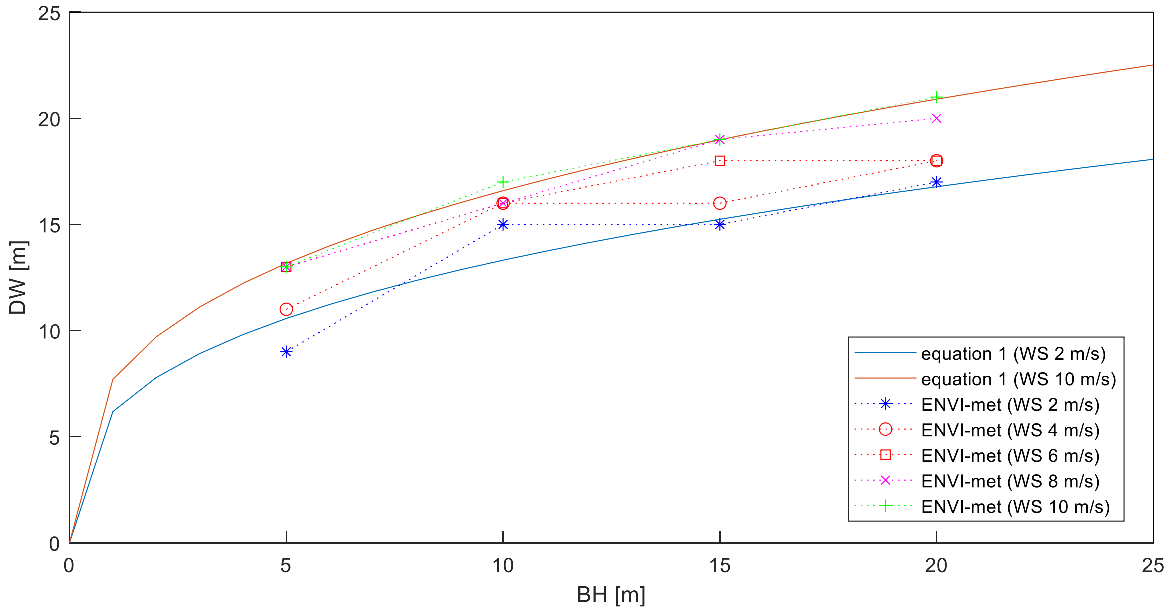

Figure 26: Graphical representation demonstrating the correlation between building height, wind velocity, and the extent of the hazardous zone – downstream wake zone.

Following a similar approach to the downstream wake analysis, the data illustrated in Figure 27, depicting the relationship between building height (BH), wind speed (WS), and the extent of the vertical updraft (VU) hazardous zone, was rigorously examined to establish a mathematical correlation between these parameters. The objective remained the same, to derive a practical equation for predicting the size of the dangerous zone for UAS operations, contingent upon wind velocity and building height.
The resulting formula (Equation 25) for vertical updraft distance (VU) mirrors the structure of the downstream wake equation, adhering to the same power-law relationship and incorporating analogous scale and shape parameters.

The VU scale parameter, represented by the expression (k_{1VU} + k_{2VU}*(WS)), governs the overall magnitude of the vertical updraft.

a) Constant Term, k_{1VU} = 1.06, denotes the baseline updraft height, present even in calm conditions. It accounts for the inherent upward deflection of airflow caused by the building's facade.

b) Wind Speed Coefficient, k_{2VU} = 0.2, modulates the updraft height in response to variations in wind speed (WS). Stronger winds amplify the upward deflection, leading to a taller updraft. The coefficient quantifies this effect, ensuring that the updraft height increases proportionally with escalating wind velocity.

The VU shape parameter, expressed as $BH^{3/5}$, determines the geometric form of the updraft, approximating it as a parabola.

Building Height Exponent signifies that the vertical updraft height grows with the building height (BH) raised to the power of 3/5. This exponent, distinct from the 1/3 exponent in the downstream wake equation, reflects the steeper growth observed in the updraft data compared to the wake data. Taller buildings induce stronger updrafts, and the 3/5 exponent captures this accelerated growth rate.
The constants k_{1VU} = 1.06 and k_{2VU} = 0.2 were determined through an iterative optimization process, refining the formula to minimize the average prediction error across the dataset. The resulting equation:

$$VU = (k_{1VU} + k_{2VU}\,(WS))*(BH)^{3/5} \qquad \text{Equation 25}$$

achieves a high level of accuracy, with deviations from the simulated data generally within 6.1%

Figure 27 visually reinforces the formula's implications. The five distinct curves illustrate the dependency between building height (ranging from 5m to 20m) and wind speed (ranging from 2 m/s to 10 m/s), showcasing how the updraft height expands with both increasing building height and wind speed. Unlike the downstream wake, where the curves were relatively evenly spaced, the curves for the vertical updraft become more widely spaced as building height increases, reflecting the steeper growth rate captured by the 3/5 exponent.

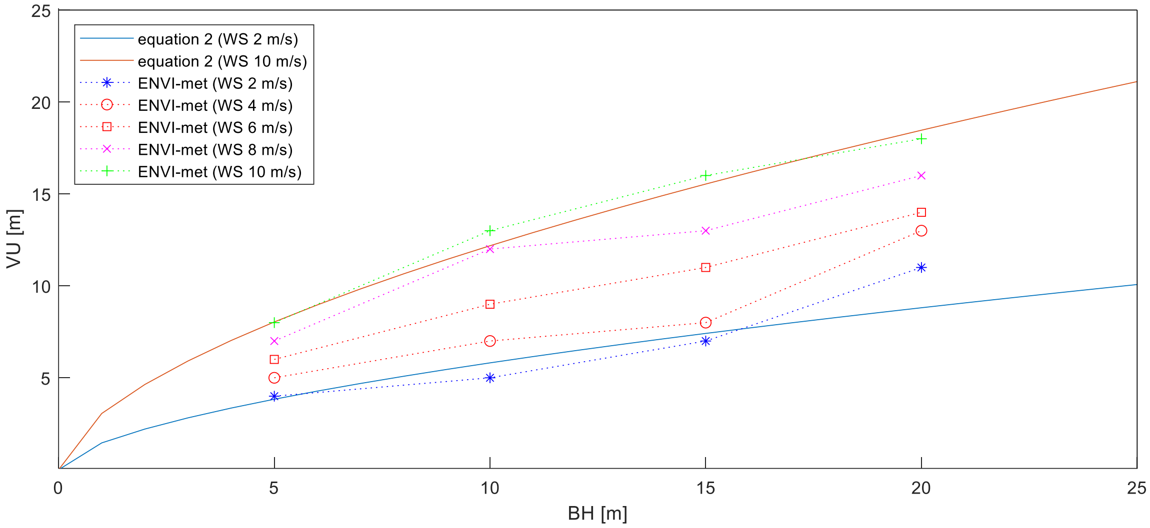

Figure 27: Graphical representation demonstrating the correlation between building height, wind velocity, and the extent of the hazardous zone – vertical updraft zone.

5.3.2 AdMaS centre scenario

To validate the formulas (Equations 24 and 25) derived from the simplified single-building simulations in a real-world situation and to establish a baseline for the subsequent field experiments, a detailed numerical simulation of the AdMaS research centre environment was conducted. This model served two primary purposes:

a) Immediate Validation: The study aimed to promptly verify if the sizes of the downstream wake and updraft distances, as predicted by the numerical simulation results near the main building (Building H) in the AdMaS complex, aligned with the values calculated using the new empirical formulas. This initial comparison served to assess the applicability of these formulas in real-world scenarios.

b) **Real-time Data Comparison:** The model acted as a virtual testbed for comparison with real-time wind velocity data collected during the UAS flights conducted in the spring-summer of 2024. This comparative analysis facilitated the further validation and refinement of our turbulence models, ensuring their robustness and applicability in informing safe and efficient UAS operations within complex urban environments.

5.3.2.1 Meteorological data acquisition

Historical meteorological data for Brno - AdMaS location was provided by two meteorological information service providers. The first provider is the company „Meteomatics“, which was already described in detail in section 2.3 The data and their accuracy were verified during the demonstration mission in Rzeszów, and due to the excellent results, the cooperation was extended at this stage as well. The second provider of historical data is ČHMÚ: Czech Hydrometeorological Institute.

From both information sources, 5 meteorological parameters were obtained:
1. temperature
2. barometric pressure
3. relative humidity
4. wind speed
5. wind direction

The main analysed period was the spring-summer season, due to the schedule of the main demonstration mission in the AdMaS campus. Summary of the most important information is described in the following section and additional detailed information in APPENDIX I.

Meteomatics

Historical data was provided for the last 4 seasons (April - May), years 2020 - 2023. Time increments were 15 minutes. The coordinates of the place for which the data were provided are located in the AdMaS campus (See Figure 28). This location was chosen due to the future integration of a portable weather station during the Spring 2024 demonstration mission.

Figure 28: Meteomatics historical data, coordinates information (49°14'06.6"N 16°34'18.1"E)

Time information	
Years	2020 - 2023
Months	March, April, May
Time increments	15 minutes
Meteorological parameters	
Temperature [°C]	at 2 m above ground
Pressure [hPa]	Mean Sea Level
Relative humidity [%]	at 2 m above ground
Wind speed [m/s]	At 10 m above ground
Wind direction [degrees]	at 10 m above ground

Figure 29: Summary of Meteomatics historical data

One of the most important input types of information is the wind characteristics. The wind direction and speed analysis were processed in the form of a wind rose. In the first step, the spring periods of individual years (2020 – 2023) were analysed separately, to compare whether individual seasons are similar, or whether large differences are observed between individual years (For more details, see APPENDIX I.).

The demonstration verification mission was planned for April 2024 in the time window from 09:00 a.m. until 03:00 p.m. And based on this information, historical data was filtered to estimate the most likely meteorological conditions that will be observed on the flight days. Figure 30 shows average April wind rose (2020 – 2023) daily characteristic (excluding evening and night).

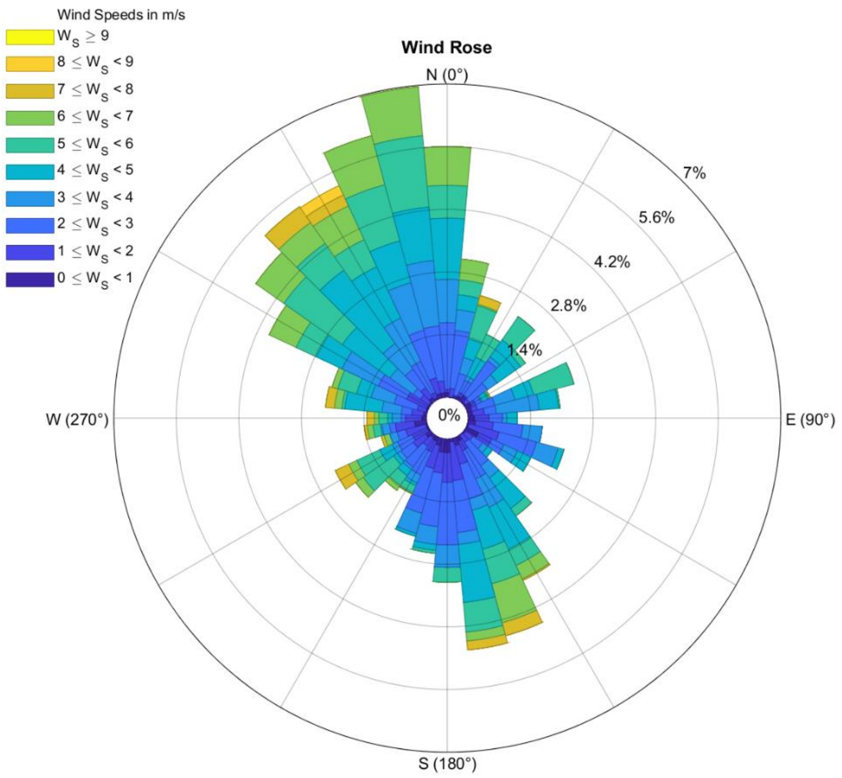

Figure 30: Wind rose April 2020 – 2023 (Time window from 09:00 a.m. to 03:00 p.m.)

Based on this analysis, we decided on simulation scenarios that will use a North wind direction.

For another three parameters (relative humidity, MSL pressure and temperature) were performed same data analysis and data filtering as in the wind characteristics.

Table 13: Average values of basic parameters (Meteomatics data)

Parameter	Values
Relative humidity	**48.00 %**
MSL pressure	**1016.20 hPa**
Temperature	**12.15 °C**

ČHMÚ (Czech Hydrometeorological Institute)

Near the point of interest, ČHMÚ has two meteorological stations. One in the Zabovresky location, which is approximately 2 km distant from AdMaS. The second meteorological station is located at Turany airport, approximately 12 km distant from AdMaS. Data that were measured at the closest possible distance are more relevant, and therefore historical data from the meteorological station Zabovresky was preferred. However, atmospheric pressure is recorded only at the Turany airport, and for this reason, meteorological data from other meteorological stations were also used for supplementation.

Table 14: ČHMÚ historical data

Meteorological parameter	**Index type**	**Location**	**Period**
Temperature	Average	Zabovresky	1987 - 2022
Relative humidity	Average	Zabovresky	1987 - 2022
Pressure	Average	Turany	1961 - 2022
Wind speed	Average	Zabovresky	1987 - 2022
Wind speed	Maximum	Zabovresky	1999 - 2022
Wind direction	Maximum	Zabovresky	1999 - 2022

Wind rose

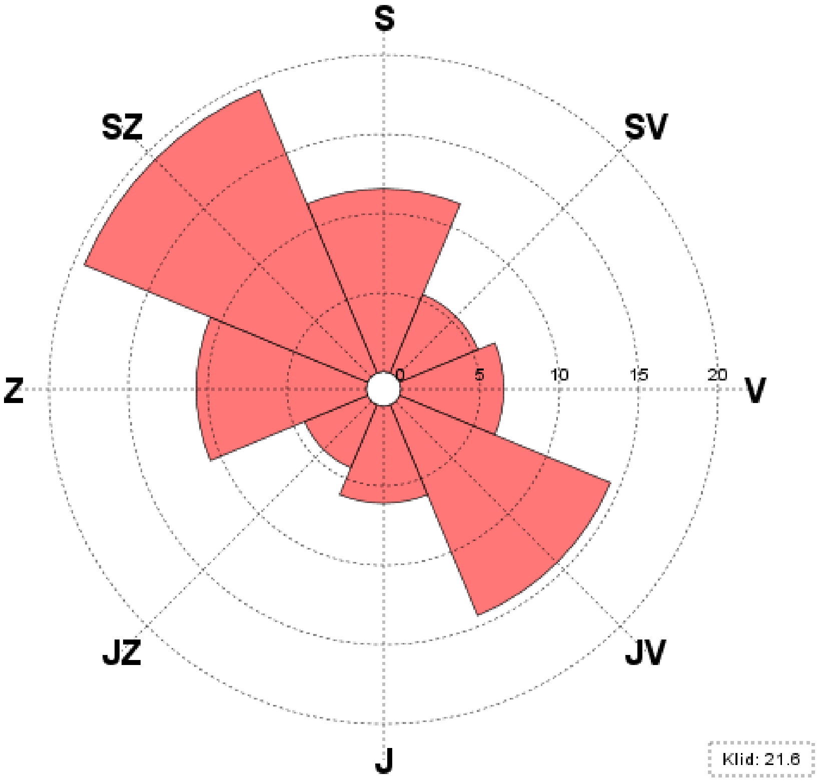

Figure 31: Wind rose (2011 - 2022) [source: ČHMÚ]

Max daily wind speed

Historical data obtains maximum daily wind speed for the period 2000 – 2022. On the Figure 32, see graph shows Months average of Maximum daily wind speed (average of all April days from 1st to 30th) for each calendar year.

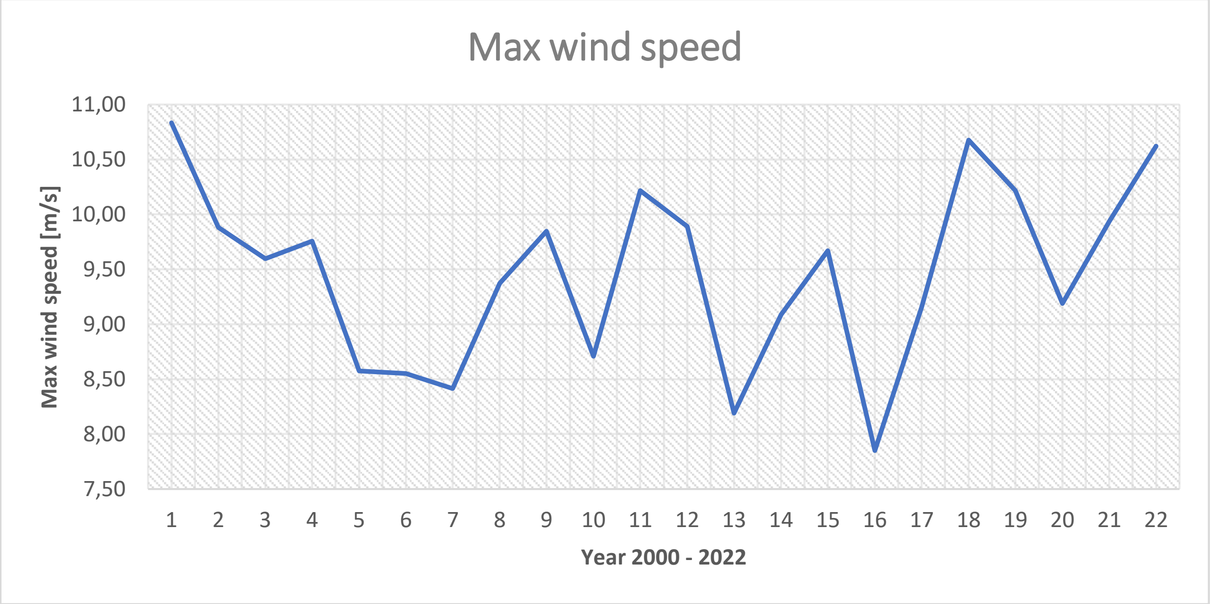

Figure 32: Max wind speed 2000 – 2022 (April average)

Temperature

Historical data obtains average daily temperature for the period 1987 – 2022. On the Figure 33, see graph shows Average April temperature (average of all April days from 1st to 30th) for each calendar year.

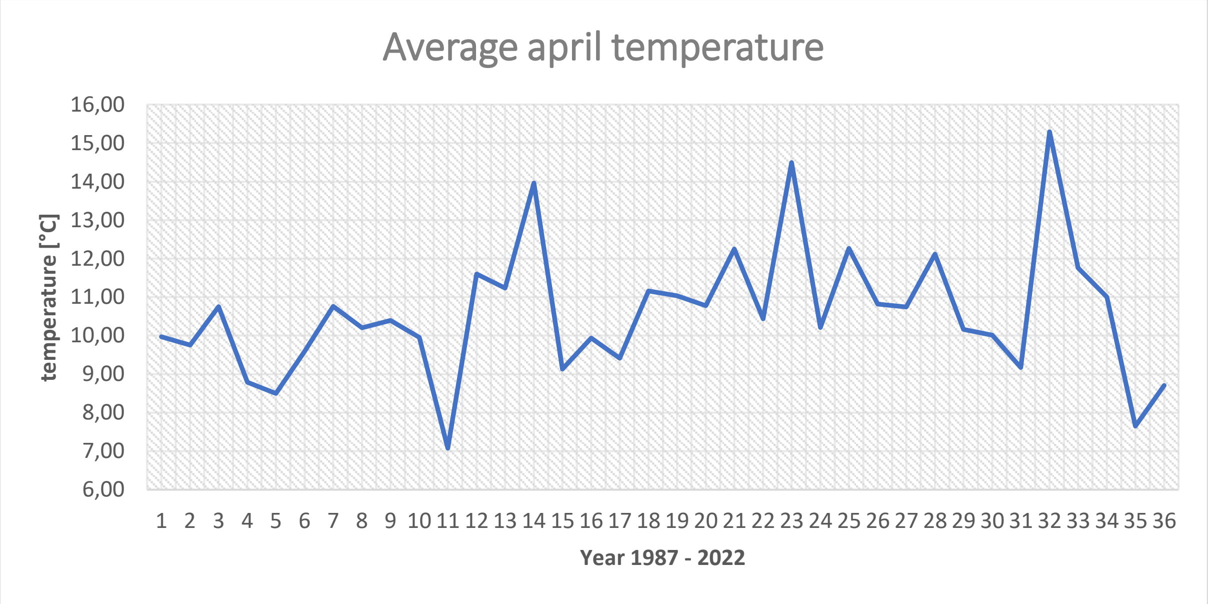

Figure 33: Average temperature (April average)

Relative humidity

Historical data obtains average daily relative humidity for the period 1987 – 2022. On the Figure 34, see graph shows Average April temperature (average of all April days from 1st to 30th) for each calendar year.

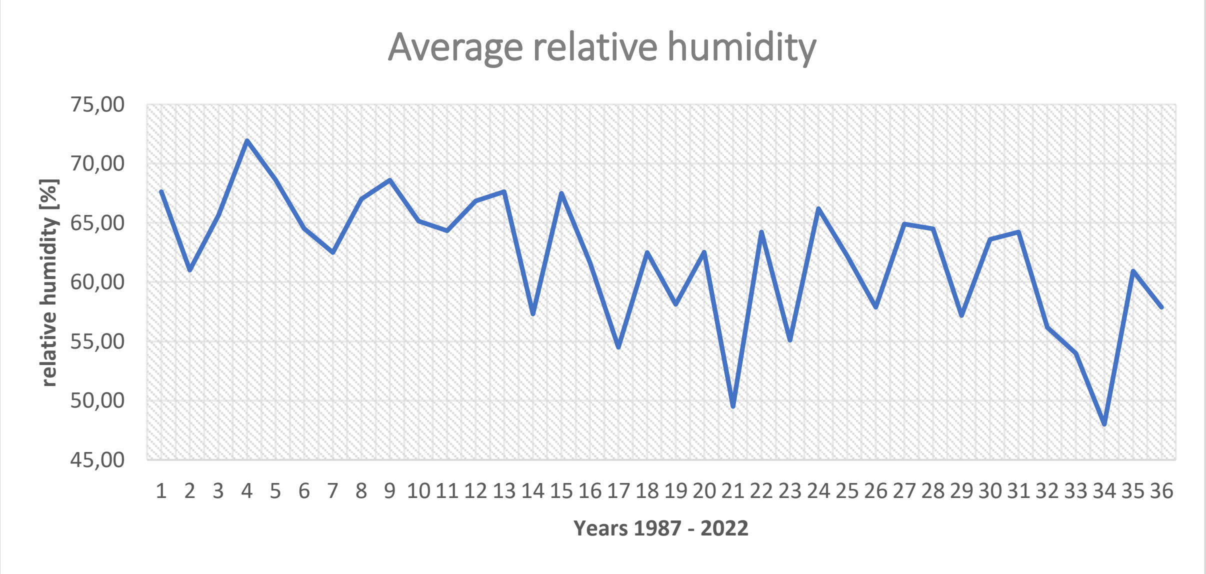

Figure 34: Relative humidity (April average)

Barometric pressure

Historical data obtains average daily barometric pressure for the period 1961 – 2022. On the Figure 35, see graph shows Average April barometric pressure (average of all April days from 1st to 30th) for each calendar year.

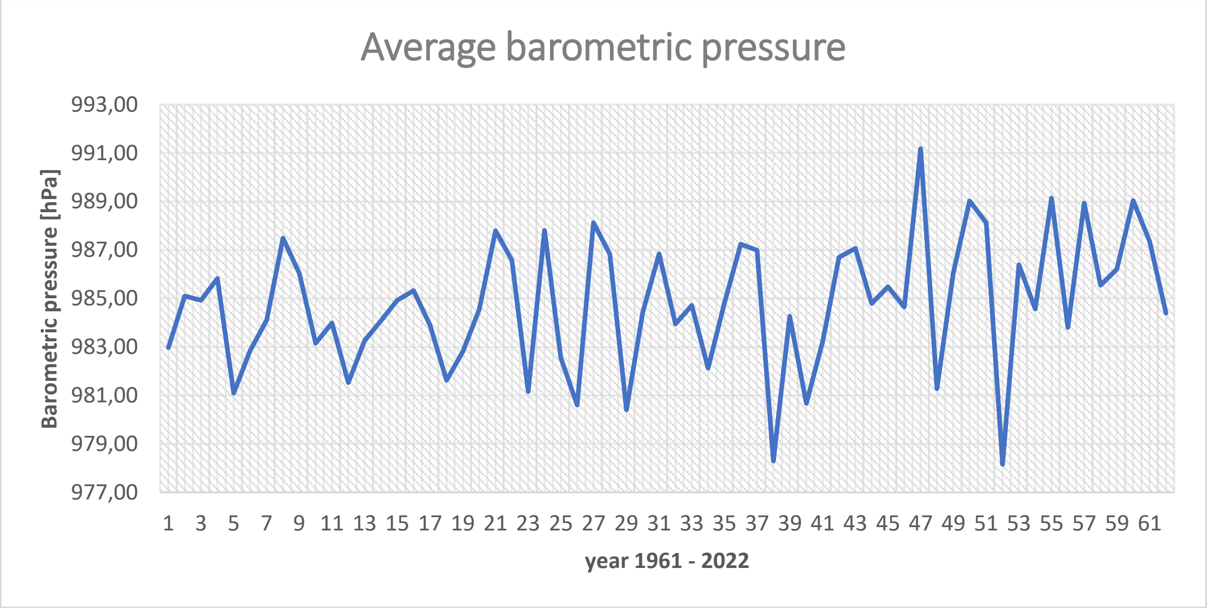

Figure 35: Barometric pressure (April average)

5.3.2.2 Digital Terrain Model (DTM)

Another very important input is a detailed geological analysis of the AdMaS Centre area and also the surrounding terrain. Since it has been proven that the prevailing wind in the given location is north to northwest, it is necessary to emphasize the terrain relief in the direction of prevailing wind.

Figure 36 displays a terrain map oriented to the north. For this study, the focus is mainly on building H, around which the demonstration mission and turbulence detection will be carried out. As can be seen on the map, there is a nearby hill in front of the AdMaS campus from the north side. This fact needs to be verified by Reattachment distance calculation in order to be able to correctly decide on the size of the area for which the numerical simulation will be processed in the ENVI-met software.

Figure 36: AdMaS centre and surroundings

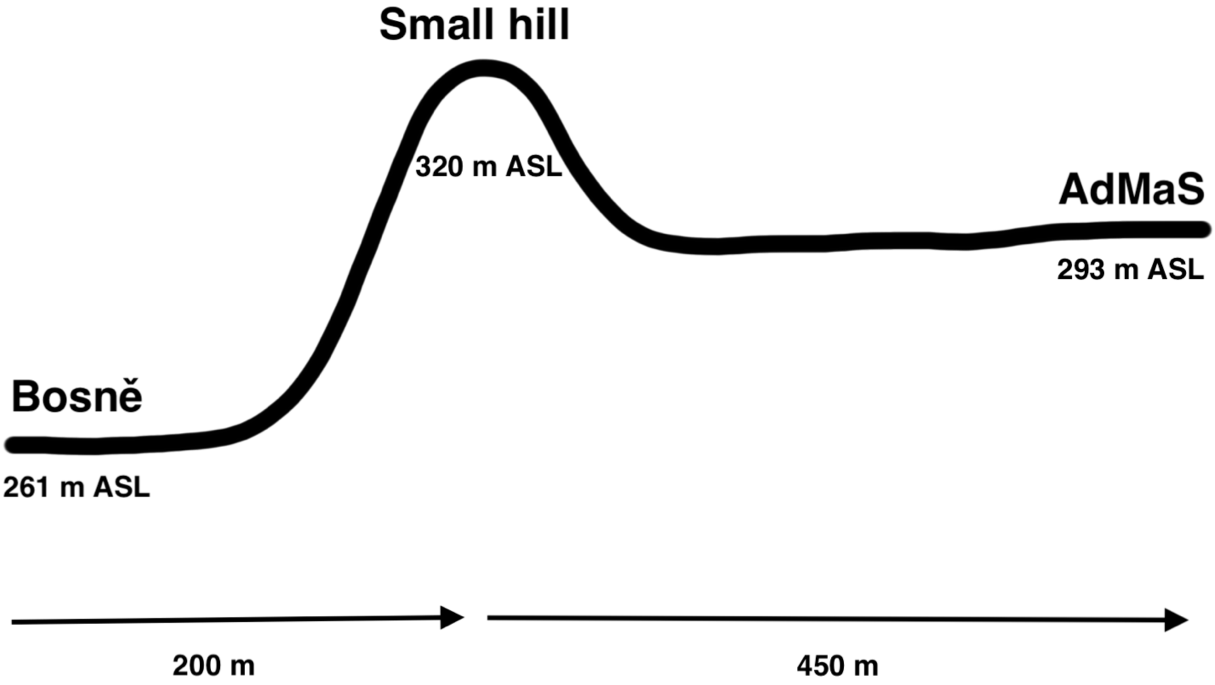

Figure 37: Medlanecky hill profile

Reattachment distance calculation

Regarding the hill placed upstream the main prevailing wind direction (North to North-West), the distance of flow reattachment in the case of a Backward-Facing Step with:

Re = U*h/nu > 3000-300000

U = the velocity,
h = the height of the step,
nu = the kinematic viscosity of the fluid

is Re = 5-7 h

In case, surely less extreme than the BFS, as there is not a sharp change in direction but a smooth (natural) one. Based on the previous meteorological and georeferenced analysis, U is in the range 2-8 m/s, H = 27m and nu = 1.48 x 10-5 m2/s. Based on all provided information is determined Re = 3.6 x 10-6 – 14.5 x 10-6 and reattachment distance = 135-190 m, what is much smaller than the distance between the hill and AdMaS Campus (distance is 450 m).

Based on this calculation, it is possible to claim that it is not necessary to consider the distant surrounding terrain of the AdMaS area, but it is sufficient to focus only on the limited area of the centre.
In the next step it was necessary to evaluate the defined area of the centre. If the terrain is fragmented, importing a digital terrain model is necessary. However, if it is a flat terrain, it is possible to forget about DTM and it is sufficient to model only buildings, roads, vegetation, etc. As shown in the Figure 36 and Figure 37, it is clear at first glance that the AdMaS area is a flat terrain. And based on the stated reasons, DTM was not used in the processed numerical simulations.

Figure 38:2D DTM AdMaS Centre

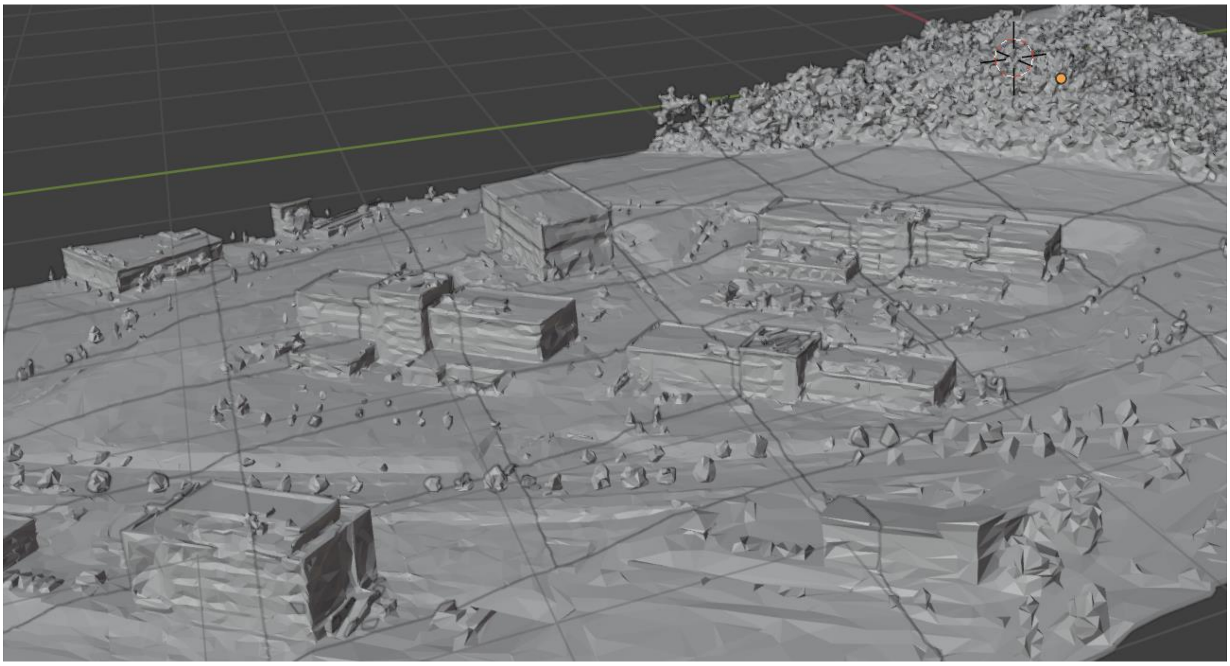

Figure 39:3D DTM AdMaS Centre

5.3.2.3 Concept of AdMaS numerical simulations

Based on the meteorological analysis of Figure 30, where the colours represent the wind velocity, the bar position the direction the wind comes from and the bar length the percentage that windblown during the investigated period, we determined that the most frequent wind directions fell within the range of 330-359 degrees, with the most frequent velocities in the range from 1 to 6 m/s. This information was used during design of simulation scenarios, ensuring that data reflected the most common wind conditions experienced at the AdMaS research centre. As the 1 m/s velocity is considered not to be dangerous for the UAS operations, the simulations of the AdMaS centre were performed with undisturbed velocities of 2, 4 and 6 m/s. The demonstration flights will be performed when the wind conditions will be within this simulated velocity range.

Topographical analysis of the surrounding terrain, particularly a prominent hill situated north of the AdMaS centre, was conducted to build the simulation domain. Calculations of the reattachment distance (135 – 190 m), based on prevailing wind conditions and hill geometry (hill distance 450 m), indicated that the hill's influence (see Figure 37) air flow within the campus would be negligible. Consequently, and considering that the terrain is flat inside the AdMaS centre, we delineated the simulation domain shown on the Figure 40. The domain was rotated to be aligned with the building H, around which the demonstration flights will be performed. Moreover, the modelling of buildings (materials and sizes), vegetation, and other pertinent features (e.g., pavements and roads) within the campus was done in the numerical model.

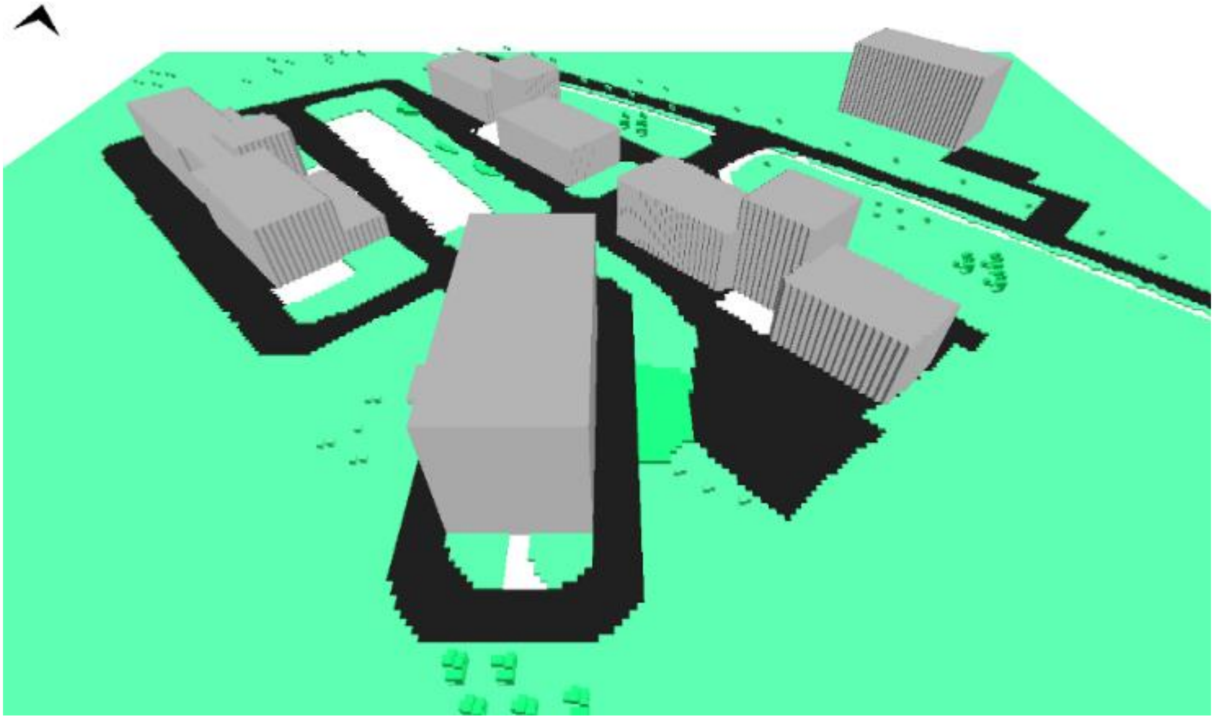

Figure 40: Visualization of the 3d simulated domain

Utilizing the ENVI-met model, wind flow patterns around Building H were simulated under the predominant wind conditions identified through meteorological analysis: for example, on Fig. 13, the wind velocity field in a horizontal plane close to the terrain level, at 12:00 and with an undisturbed wind speed of 4 m/s is shown. Due to the above-mentioned rotation of the domain, in the figure the wind comes from above. The downstream wake zones behind the buildings are visible. In Fig. 14, the wind velocity field in a vertical plane taken in the middle of the building H width at 12:00 p.m., with an undisturbed wind velocity of 4 m/s, is shown. In this figure, the wind comes from the right and the interaction between the flow patterns between the buildings is visible; the building H is identifiable as the largest one on the left. This section was used to measure the dimensions of the downstream wake zone and of the updraft zone induced by the interaction between the wind flow and the building H in presence of the other buildings, using the same methodology illustrated in 5.3.1. In Table 15 these values were subsequently compared with the predicted sizes calculated using the empirical formulas derived from the single-building simulations (Equation 24 and 25).

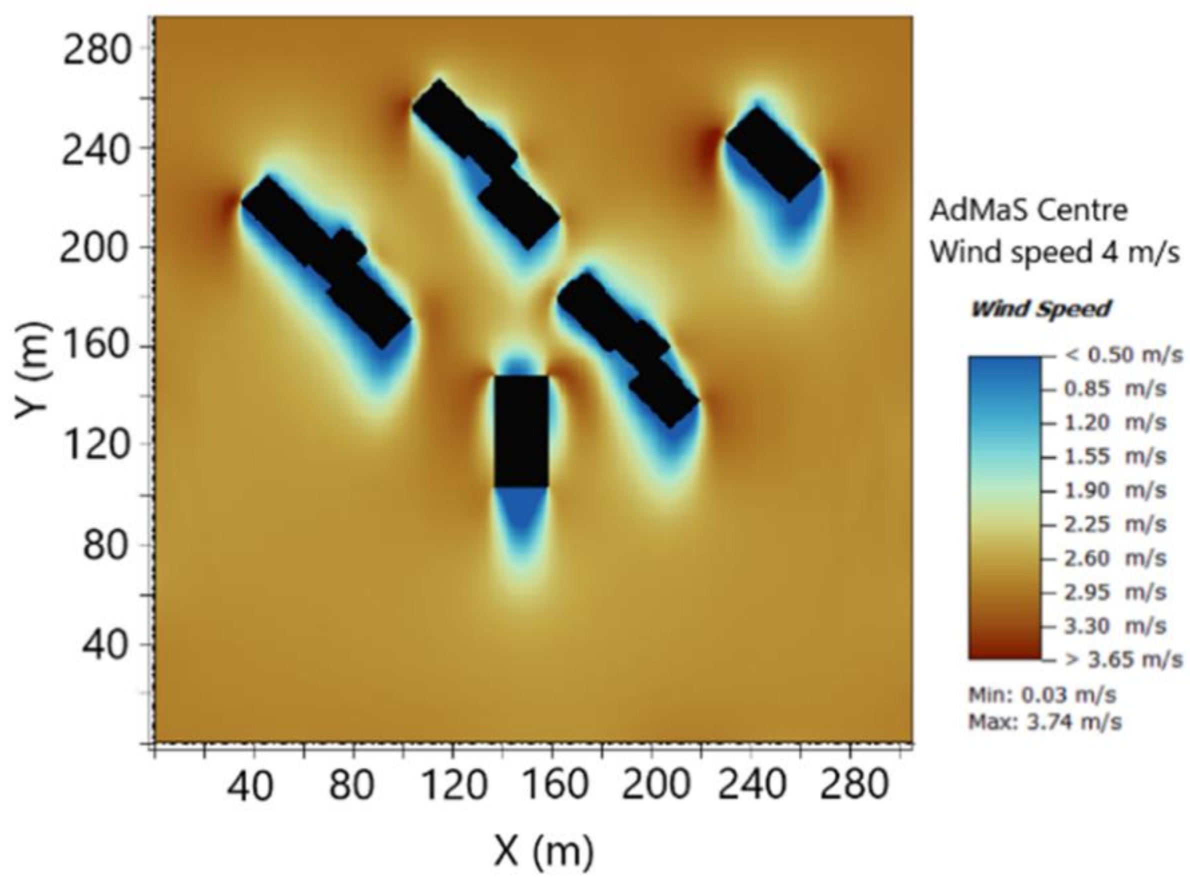

Figure 41: wind velocity field in a horizontal plane close to the terrain level (9,5 m above the ground) at 12:00, extracted as an output of the ENVI-met numerical simulation of AdMaS centre with starting wind speed 4 m/s; wind comes from above.

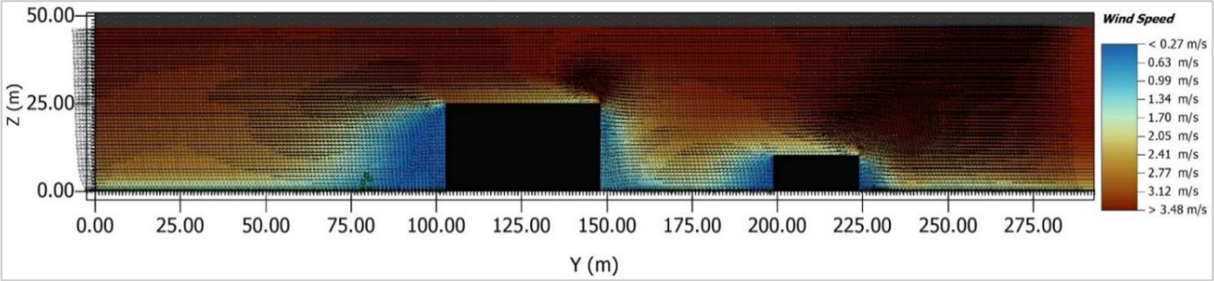

Figure 42: wind velocity field in a vertical plane taken in the middle of the building H width at 12:00, extracted as an output of the ENVI-met numerical simulation of AdMaS centre with starting wind speed 4 m/s; wind comes from the right.

Table 15: Comparison of calculated (via eq. 1 and 2) and measured (on the numerical simulations of the AdMaS centre) danger zone sizes

Building height	Wind Speed	Calculated wake distance (equation 24)	Measured dimension of DW distance in numerical simulation (ENVI-met)	Calculated vertical updraft distance (equation 25)	Measured dimension of VU zone in numerical simulation (ENVI-met)
25 m	2 m/s	18 m	19 m	10 m	10 m
25 m	4 m/s	20 m	20 m	13 m	15 m
25 m	6 m/s	21 m	21 m	21 m	18 m

5.3.3 Initial results

The data presented in Table 15 compares the results of the AdMaS simulations (for building H with BH = 25 m) with the calculated values obtained using the refined equations 24 and 25. The formula for downstream wake distance (equation 24), demonstrates a good agreement with the simulation results (all simulations result is in the APPENDIX III.). For wind speeds of 2, 4 and 6 m/s, the calculated wake distances of 18 m, 20 m, and 21 m, respectively, closely match the simulated values of 19 m, 20 m, and 21 m. These results indicate that the equation effectively captures the relationship between building height, wind speed, and downstream wake length for this specific building configuration.

The formula for vertical updraft distance (equation 25), shows a generally good agreement with the simulation results for wind speeds of 2 m/s and 6 m/s. The calculated VU distances of 10 m and 21 m are very close to the simulated values of 10 m and 18 m, respectively. However, at a wind speed of 4 m/s, the calculated VU distance of 13 m slightly underestimates the simulated value of 15 m.

This discrepancy can likely be attributed to the complex interaction between the incoming wind profile, the upstream buildings, and the specific shape of building H. The simplified model used in the formula might not fully capture these intricate interactions, leading to some deviation from the simulation results. In summary, the preliminary analysis indicates a favourable overall agreement between the simulated and predicted values for both the downstream wake and vertical updraft distances. This provides initial support for the applicability of our formulas to real-world building configurations. The discrepancies observed in the vertical updraft distance for a wind speed of 4 m/s highlight the importance of considering the complex interactions between buildings, terrain, and vegetation in determining the precise size of the dangerous zones for UAS operations in the built environment. While the current formulas offer valuable insights and predictions, future research could focus on refining the vertical updraft model to better account for these complex interactions and further reduce prediction errors. This could involve incorporating additional parameters, exploring alternative functional forms, or utilizing more sophisticated simulation techniques.

To validate these simulation results and their implications for real-world UAS operations, a demonstrative mission was planned. This mission necessitated careful preparation, including the selection of suitable measurement sensors, unmanned aerial vehicles (UAVs), and a terrestrial meteorological station. The hardware components crucial to the success of this demonstrative mission are detailed in Chapter 5.4.

5.4 Hardware equipment

Upon completion of the numerical simulations, the research progressed to the preparation of a demonstrative mission. This mission is designed to validate the accuracy and precision of the aforementioned simulations. In anticipation of the test flights, meticulous preparations were undertaken, encompassing the selection of appropriate measurement sensors, unmanned aerial vehicles (UAVs), and a terrestrial meteorological station. In chapter 5.4. is presented comprehensive examination of the hardware components integral to the demonstrative mission.

5.4.1 Sonic anemometer

Building upon prior research on drone-based wind measurement [102] and [109], ultrasonic anemometers were identified as the ideal technology due to their ability to measure three-dimensional wind vectors without moving parts. However, existing research has primarily focused on high-cost, high-frequency anemometers, which are often impractical for smaller UAS platforms due to weight and budget constraints [109]. High-quality ultrasonic anemometers can range in cost from 1,500€ to 20,000€ and weigh between 0.225 kg and 2.150 kg, making them unsuitable for many smaller UAS.

To address this limitation, affordability and ease of integration was prioritized, selecting the Calypso "Ultrasonic Portable Mini" anemometer. This compact (0.078 kg), wireless sensor offers a 1 Hz sampling rate and seamless integration with a mobile app for data logging. While this approach aligns with the need for low-cost, lightweight sensors for UAS applications, as emphasized in [119], the lower sampling rate necessitates rigorous validation to ensure accurate turbulence estimation, unlike the higher-frequency sensors (10 Hz and above) used in studies like [120]. The main distinction of this approach lies in the development of a turbulence estimation system tailored for the specific characteristics of low-cost, low-frequency sensors commonly found on smaller UAS platforms. While previous studies like [120] focused on modelling urban wind field effects on UAS flight using high-fidelity simulations and data from specialized sensors, our research aims to provide a practical and accessible solution for smaller UAS operators by leveraging affordable sensors and validating their performance in real-world conditions.

Therefore, prior to UAS integration, the Calypso anemometer underwent wind tunnel testing Figure 43 to assess its accuracy under controlled conditions. The anemometer was tested across a range of wind speeds from 1 m/s to 15 m/s (see Figure 44, with each velocity maintained for 60 seconds. This testing methodology, similar to that employed in [121], allows to systematically evaluate the sensor's performance across the wind speeds most relevant to our target operating environment, including the gusty conditions near buildings studied by [122].
Furthermore, this approach diverges from previous work that relied on high-frequency sensors and comprehensive flight data typically available on commercial aircraft (NCAR). Instead, the Eddy Dissipation Rate (EDR) calculation methodology was adapted to accommodate the lower sampling rate (1 Hz) and limited sensor suite of the UAS platform. This adaptation enables to estimate turbulence in real-world conditions, bridging the gap between theoretical models and practical applications for smaller UAS operators.

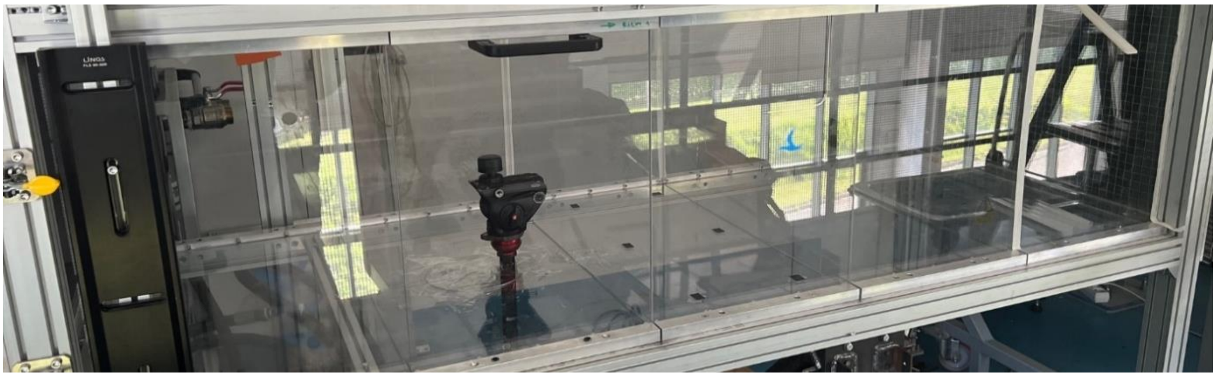

Figure 43: Calypso sonic anemometer located in the wind tunnel during verification tests.

As expected, as shown in the Table 16, the anemometer exhibited higher deviations (over 10%) at wind speeds below 3 m/s. This is a common observation in aerodynamic measurements at low speeds. However, for wind speeds above 3 m/s, the Calypso anemometer demonstrated high precision, with deviations consistently below 10% (above 7% below 3%). Moreover, low wind velocity is less critical from the point of view of danger for the UAS flights.

Table 16: Results of the sonic anemometer accuracy verification tests, using a wind tunnel venturi tube as reference.

Level	Calypso data 60 sec average [m/s]	Wind tunnel data 60 sec average [m/s]	Deviation 60 s Average [m/s]	% deviation
1	0.530	0.227	0.447	44.71
2	1.755	1.238	0.783	39.16
3	3.067	2.772	0.388	12.94
4	4.392	4.174	0.324	8.10
5	5.690	5.552	0.230	4.60
6	6.968	6.838	0.228	3.80
7	8.242	8.159	0.181	2.58
8	9.568	9.476	0.208	2.60
9	10.897	10.818	0.168	1.87
10	12.233	12.149	0.175	1.75
11	13.595	13.491	0.171	1.56
12	14.998	14.839	0.241	2.01
13	16.387	16.211	0.218	1.68
14	17.918	17.575	0.397	2.83
15	19.351	18.957	0.445	2.97

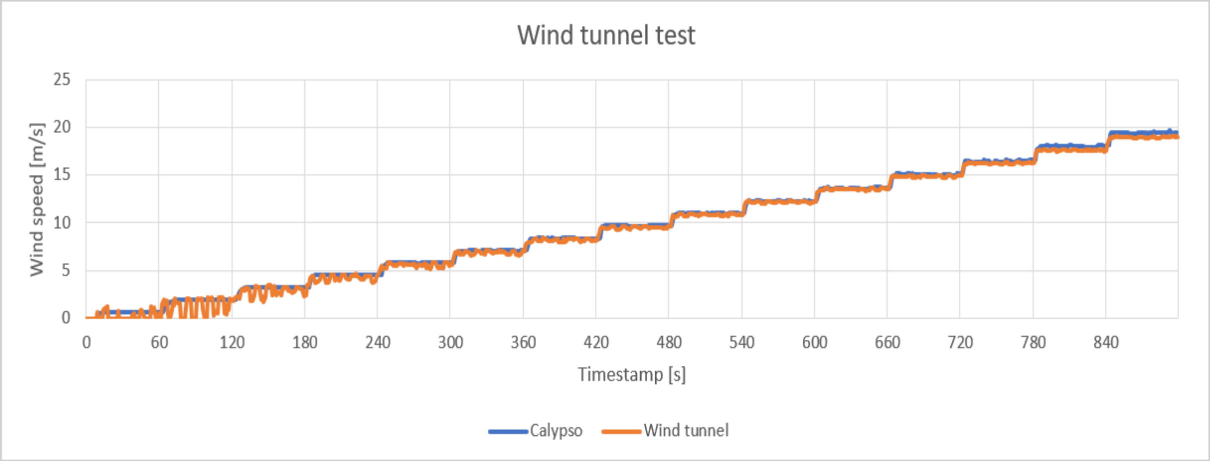

Figure 44: Dependency between time (horizontal axis) and wind speed (vertical axis) clearly shows low measurement precision below 3 m/s, but sufficient precision above.

5.4.2 UAV platform

Following wind tunnel validation, the Calypso anemometers were initially integrated onto the DJI M100 four-rotor UAS fitted with the Cube Orange+ autopilot module running the PX4 flight stack. The custom-build setup involved the Calypso devices mounted on a carbon tube 148 cm apart, a distance securing a sufficient clearance from the rotors in order not to influence the measurements [109]. Initial flight tests focused on assessing the UAS's manoeuvrability and stability with the added sensors, as well as verifying the reliability of the Bluetooth data connection and the effectiveness of the data logging process. These tests ensured the system's operational readiness for the subsequent field experiments.

Initial idea was aiming to capture three-dimensional wind characteristics. However, during flight tests, it became evident that while the horizontally oriented sensor provided accurate measurements, the vertically oriented sensor exhibited significant errors, with readings reaching up to 25 m/s in some instances. These discrepancies, likely attributed to flow distortion, sensor sensitivity, and vibrations inherent to the UAS platform and the low-cost sensor, necessitated a methodological adaptation.

In light of the challenges encountered with vertical wind measurements, the decision was made to focus exclusively on the horizontal wind data and adapt the analysis to a two-dimensional framework. This shift allowed for a more reliable and robust assessment of turbulence characteristics within the constraints of the available sensor technology. The Calypso anemometer, while exhibiting limitations in the vertical orientation, demonstrated high precision in measuring horizontal wind speeds, making it suitable for characterizing the dominant flow patterns in the near-field environment of the building.

The observed errors in the vertical wind speed measurements can likely be attributed to a combination of factors inherent to the Calypso anemometer's design and the specific conditions of UAS operation:

- **Flow Distortion:** The presence of the UAS platform itself, particularly the rotor downwash, can create complex flow patterns and turbulence in the vicinity of the vertical sensor. This flow distortion can lead to inaccurate readings, especially for a low-cost sensor like the Calypso, which may be more susceptible to such disturbances compared to high-end research-grade anemometers.
- **Sensor Sensitivity:** Ultrasonic anemometers, including the Calypso, rely on measuring the time-of-flight of acoustic pulses between transducers. In the vertical orientation, the sensor's sensitivity to small changes in temperature and humidity gradients along the measurement path can be amplified, potentially contributing to measurement errors.
- **Vibrations:** Vibrations transmitted from the UAS platform to the vertically mounted sensor could also introduce noise and inaccuracies into the measurements.

The Eddy Dissipation Rate (EDR) is a key turbulence metric. The inertial dissipation method using structure function [124] was selected for EDR calculation, as detailed in our previous work [123]. This method was adapted for 1 Hz sampling rate by adjusting the range of temporal separation (τ) and extending the time window for analysis. Preliminary flight tests, including hovering manoeuvres, allowed to measure baseline EDR values and further refine our calculation methodology.

Figure 45: the DJI M100 UAS fitted with two Calypso anemometers during the initial flight tests.

5.4.3 Ground meteorological station

To establish a reliable ground truth reference for in-situ wind measurements during UAS flight tests, a Davis Vantage Pro2 meteorological station (Figure 46) was employed. This research-grade station, renowned for its capacity to deliver professional-grade meteorological data, was configured to record real-time wind speeds (up to 90 m/s), temperature, humidity, barometric pressure, rainfall, and additional relevant parameters such as heat index, dew point, and high/low values.

Figure 46: ground-based reference, meteorological station Davis Vantage Pro2 during UAS test flight.

In the context of this investigation, the Vantage Pro2 served as a ground-based reference for the validation of wind speed measurements acquired by the onboard Calypso anemometer during a dedicated test flight. The UAS was operated at an approximate altitude of 2 meters above the terrain, corresponding to the elevation of the Davis anemometer. Comparative analysis of the data obtained from both sensors (Figure 47) revealed a high degree of concordance, thereby substantiating the accuracy and reliability of the wind measurements. Due to the different position of both ground- and air-based anemometers (Figure 51), small deviations observed were expected.

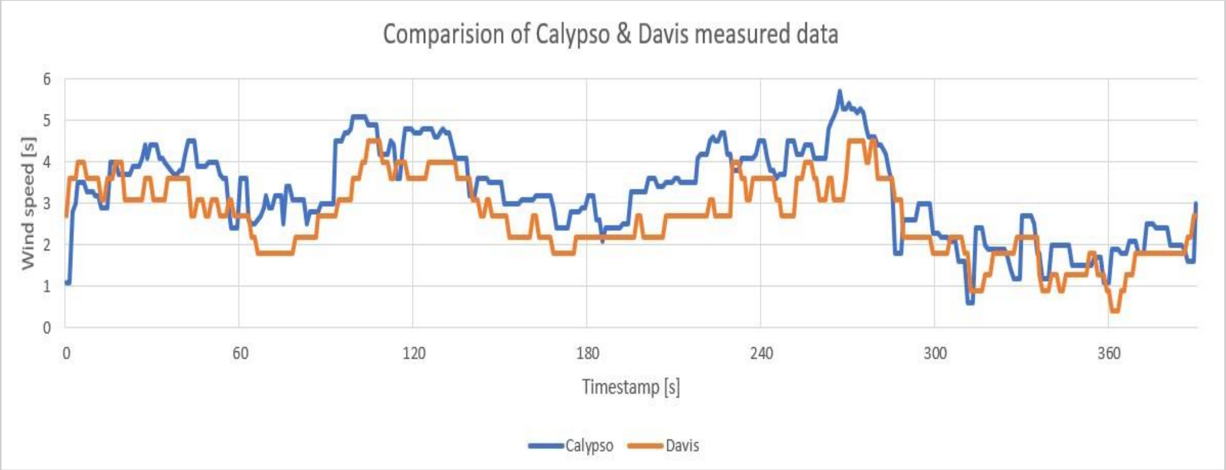

Figure 47: The comparison of the data from the ground-based reference and the anemometer onboard UAS in flight.

Furthermore, the Davis Vantage Pro2 is poised to play a pivotal role in our forthcoming demonstration mission. By furnishing precise measurements of ground-level wind speed and direction, it will enable us to accurately calibrate our numerical simulations and rigorously assess the real-world performance of our turbulence prediction models.

5.4.4 Initial results

Initial wind tunnel tests validated the accuracy of the low-cost Calypso ultrasonic anemometer for wind speeds above 3 m/s, crucial for safe UAS operations. Integration of these anemometers onto the DJI M100 UAS platform was successful, and data logging procedures were established. Additionally, the Davis Vantage Pro2 meteorological station was deployed as a ground truth reference, and its wind speed measurements exhibited strong agreement with those from the onboard Calypso anemometer during a test flight. These initial findings lay a solid foundation for further investigations into low-altitude turbulence detection using UAS platforms.

5.5 DEMONSTRATION MISSION AdMaS

5.5.1 Location

Following the successful integration and testing of the anemometers, verification of Bluetooth connectivity and data logging procedures, and validation of measurement accuracy, the preliminary testing phase was concluded. Subsequently, the main demonstration mission was conducted in Brno, within the AdMaS centre (Figure 48).

Within this centre, an analysis was performed to select the most suitable building for the test flights. Key parameters considered included the building's orientation, shape, and surrounding structures. The chosen building, Building H, experiences minimal external influences and features a simple, streamlined design without complex architectural elements. Its north-facing orientation is ideal, aligning with the prevailing northerly winds in the area. The test flights were executed on the southern side of the building, at the edge of the AdMaS centre where no other structures are present. This location minimized potential interference from surrounding buildings, ensuring a controlled environment for data collection.

Figure 48: Brno - AdMaS Centre

5.5.2 Concept

The primary objective of the demonstration mission is to acquire a sufficient number of measurements to validate the numerical simulations, their accuracy, and the conclusions drawn from them. To ensure the comprehensiveness of the measurements, data collection at various points is essential. A grid of points (see Figure 49 and

Table 17) was established at different flight altitudes and distances from the building. Based on the results of the numerical simulations, a measurement grid was designed, where the UAV maintained a 120-second hover mode at each point, during which measured values were recorded at a 1 Hz sampling rate.

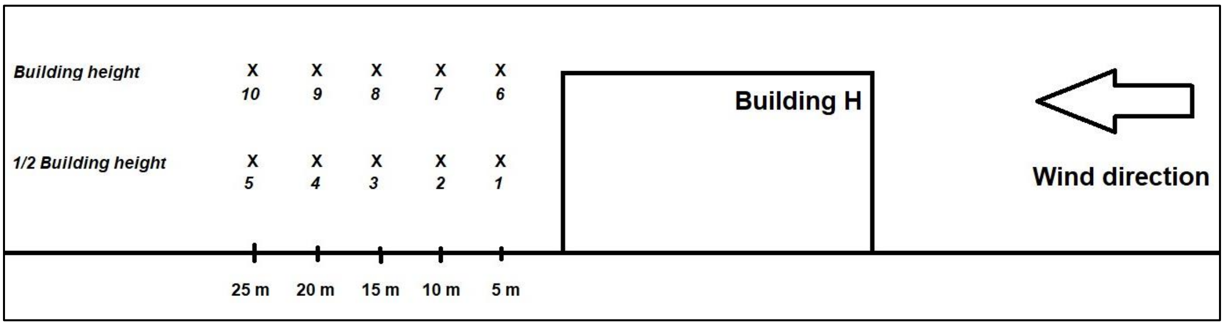

Figure 49: AdMaS measurement grid of points

Figure 50: Photos from demonstration mission AdMaS

Table 17: List of testing points

Point	Altitude	Distance from building H
1	½ Building height	5 m
2	½ Building height	10 m
3	½ Building height	15 m
4	½ Building height	20 m
5	½ Building height	25 m
6	Building height	5 m
7	Building height	10 m
8	Building height	15 m
9	Building height	20 m
10	Building height	25 m

5.5.3 Selection of test days and measurement details

Test days were strategically selected based on prevailing meteorological conditions to ensure a diverse range of wind speeds. During the testing period, the predominant wind direction was from the north, with nine distinct wind speed variations ranging from 1.51 to 3.92 m/s (measured by the ground-based meteorological station at 2 m AGL).

Pre-flight preparation was completed for each flight day, see APPENDIX II. A total of sixty 120-second measurements were conducted at various grid points. Detailed information regarding each measurement is presented in Table 18 and Table 19.

Table 18: Testing flights (altitude = ½ building height)

Wind speed measured by Davis station	120 sec average				
	Point 1	Point 2	Point 3	Point 4	Point 5
2.85 m/s	1.38 m/s	1.92 m/s	1.86 m/s	1.51 m/s	1.61 m/s
2.5 m/s	1.48 m/s	1.83 m/s	1.74 m/s	2.02 m/s	2.3 m/s
3.92 m/s	1.7 m/s	1.58 m/s	1.76 m/s	2.37 m/s	2.95 m/s
1.51 m/s	0.79 m/s	0.86 m/s	1.17 m/s	1.21 m/s	1.37 m/s
1.37 m/s	1,07 m/s	1.0 m/s	0.92 m/s	1.22 m/s	1.09 m/s
1.85 m/s	1.27 m/s	1.58 m/s	1.6 m/s	1.55 m/s	1.47 m/s

Table 19: Testing flights (altitude = building height)

Wind speed measured by Davis station	120 sec average				
	Point 6	Point 7	Point 8	Point 9	Point 10
2.31 m/s	2.17 m/s	2.2 m/s	1.52 m/s	2.54 m/s	2.9 m/s
3.12 m/s	3.42 m/s	4.38 m/s	3.51 m/s	4.04 m/s	2.73 m/s
3.36 m/s	3.59 m/s	5.56 m/s	3.27 m/s	3.07 m/s	3.09 m/s
1.81 m/s	1.87 m/s	1.9 m/s	1.77 m/s	2.79 m/s	2.79 m/s
2.98 m/s	1.93 m/s	2.6 m/s	2 m/s	2.38 m/s	2.87 m/s
1.50 m/s	1,5 m/s	1.16 m/s	1.07 m/s	1.63 m/s	1.67 m/s

5.5.4 Data Alignment for Comparative Analysis

To facilitate a direct comparison between real-time measured data and numerical simulation outputs, it is necessary to normalize the data to a common reference height. In the ENVI-met numerical simulations, the initial wind speed is consistently set at an altitude of 10 meters above ground level (AGL).

However, our ground-based reference, the Davis meteorological station, was strategically positioned in an area free from obstruction and measured meteorological conditions at a height of 2 meters AGL, see Figure 51. Therefore, prior to any comparative analysis, it was imperative to extrapolate the reference wind speed values to the 10-meter flight altitude.

Figure 51: Position of Davis meteorological station

After considering various calculation methods (e.g., exponential and logarithmic wind profiles), the power-law method (PLM) was selected due to its demonstrated accuracy in similar applications. The PLM posits an exponential increase in wind speed with height [125]. The wind profile can be calculated using the following formula:

$$v_2 = v_1 \; x \; (h_2/h_1)^{\alpha} \qquad \text{Equation 26}$$

Where”

- v_1 and v_2 represent the wind speeds
- h_1 and h_2 are heights
- α is The power law exponent , also referred to as the wind shear exponent in some studies, varies with time, altitude, and location [125]. In engineering applications, the

value of α is typically determined by the terrain type and is estimated to range from 0.1 to 0.4 [126].

Table 20: Wind shear exponent in various are types

Area type	***α***
Smooth hard ground, calm water	0.1
Tall grass on level ground	0.15
High crops, hedges and shrubs	0.2
Wooden countryside, many trees	0.25
Small town with trees and shrubs	0.3
Large city with tall buildings	0.4

Based on the classification of wind shear exponents (see Table 20) for various area types [127], a value of α = 0.3 was selected for the AdMaS location, considering its urban characteristics.

Consequently, the wind speed values measured by the Davis ground station were extrapolated to the 10-meter flight altitude using the power-law method, enabling a direct comparison with the ENVI-met numerical simulations.

Table 21: Testing flights (altitude = ½ building height) and used PLM

Wind speed measured by Davis station (2 m AGL)	***120 sec average***					
	PLM (10 m AGL)	***Point 1***	***Point 2***	***Point 3***	***Point 4***	***Point 5***
2.85 m/s	4.62 m/s	1.38 m/s	1.92 m/s	1.86 m/s	1.51 m/s	1.61 m/s
2.5 m/s	4.05 m/s	1.48 m/s	1.83 m/s	1.74 m/s	2.02 m/s	2.3 m/s
3.92 m/s	6.35 m/s	1.7 m/s	1.58 m/s	1.76 m/s	2.37 m/s	2.95 m/s
1.51 m/s	2.45 m/s	0.79 m/s	0.86 m/s	1.17 m/s	1.21 m/s	1.37 m/s
1.37 m/s	2.22 m/s	1.07 m/s	1 m/s	0.92 m/s	1.22 m/s	1.09 m/s
1.85 m/s	3.0 m/s	1.27 m/s	1.58 m/s	1.6 m/s	1.55 m/s	1.47 m/s

Table 22: Testing flights (altitude = building height) and used PLM

Wind speed measured by Davis station (2 m AGL)	***120 sec average***					
	PLM (10 m AGL)	***Point 6***	***Point 7***	***Point 8***	***Point 9***	***Point 10***
2,31 m/s	3.74 m/s	2.17 m/s	2.2 m/s	1.52 m/s	2.54 m/s	2.9 m/s
3,12 m/s	5.05 m/s	3.42 m/s	4.38 m/s	3.51 m/s	4.04 m/s	2,73 m/s
3,36 m/s	5.45 m/s	3.59 m/s	5.56 m/s	3.27 m/s	3.07 m/s	3,09 m/s
1,81 m/s	2.93 m/s	1.87 m/s	1.9 m/s	1.77 m/s	2.79 m/s	2,79 m/s
2,98 m/s	4.83 m/s	1.93 m/s	2.6 m/s	2 m/s	2.38 m/s	2,87 m/s
1,85 m/s	3 m/s	1.5	1,6	1.07	1.63	1,67

5.5.5 Comparative Analysis of Wind Speed Real-Time Data

With the reference wind speed data now aligned for both real-time measurements and numerical simulations, a comparative analysis was conducted to quantify the decrease in wind speed at each measurement point relative to the reference value (V_{REF} = Reference Wind speed). Table 23 and Table 24 presents these values for each 120-second measurement across all 60 tests.

Table 23: Quantitative Assessment of Wind Speed Reduction in the Vicinity of Building H (altitude = ½ building height)

Reference Wind speed (10 m AGL)	***Point 1***	***Point 2***	***Point 3***	***Point 4***	***Point 5***
4.62 m/s	0.30 V_{REF}	0.42 V_{REF}	0.40 V_{REF}	0.33 V_{REF}	0.35 V_{REF}
4.05 m/s	0.37 V_{REF}	0.45 V_{REF}	0.43 V_{REF}	0.50 V_{REF}	0.57 V_{REF}
6.35 m/s	0.27 V_{REF}	0.25 V_{REF}	0.28 V_{REF}	0.37 V_{REF}	0.46 V_{REF}
2.45 m/s	0.32 V_{REF}	0.35 V_{REF}	0.48 V_{REF}	0.49 V_{REF}	0.56 V_{REF}
2.22 m/s	0.48 V_{REF}	0.45 V_{REF}	0.41 V_{REF}	0.55 V_{REF}	0.49 V_{REF}
3.00 m/s	0.42 V_{REF}	0.53 V_{REF}	0.53 V_{REF}	0.52 V_{REF}	0.49 V_{REF}
Average decrease	0.36 V_{REF}	0.41 V_{REF}	0.42 V_{REF}	0.46 V_{REF}	0.49 V_{REF}

Table 24: Quantitative Assessment of Wind Speed Reduction in the Vicinity of Building H (altitude = building height)

Reference Wind speed (10 m AGL)	***Point 6***	***Point 7***	***Point 8***	***Point 9***	***Point 10***
3.74 m/s	0.58 V_{REF}	0.59 V_{REF}	0.41 V_{REF}	0.68 V_{REF}	0.77 V_{REF}
5.05 m/s	0.68 V_{REF}	0.87 V_{REF}	0.69 V_{REF}	0.80 V_{REF}	0.54 V_{REF}
5.45 m/s	0.66 V_{REF}	1.02 V_{REF}	0.60 V_{REF}	0.56 V_{REF}	0.57 V_{REF}
2.93 m/s	0.64 V_{REF}	0.65 V_{REF}	0.60 V_{REF}	0.95 V_{REF}	0.95 V_{REF}
4.83 m/s	0.40 V_{REF}	0.54 V_{REF}	0.41 V_{REF}	0.49 V_{REF}	0.59 V_{REF}
2.42 m/s	0.62 V_{REF}	0.48 V_{REF}	0.44 V_{REF}	0.67 V_{REF}	0.69 V_{REF}
Average decrease	0.60 V_{REF}	0.69 V_{REF}	0.53 V_{REF}	0.69 V_{REF}	0.69 V_{REF}

At the conclusion of the table, average wind speed reduction values are provided for the 10 measurement points. This comparative analysis enables a quantitative assessment of the wind speed attenuation caused by the building's presence, offering valuable insights into the accuracy of the numerical simulations and the complex flow patterns in the built environment.

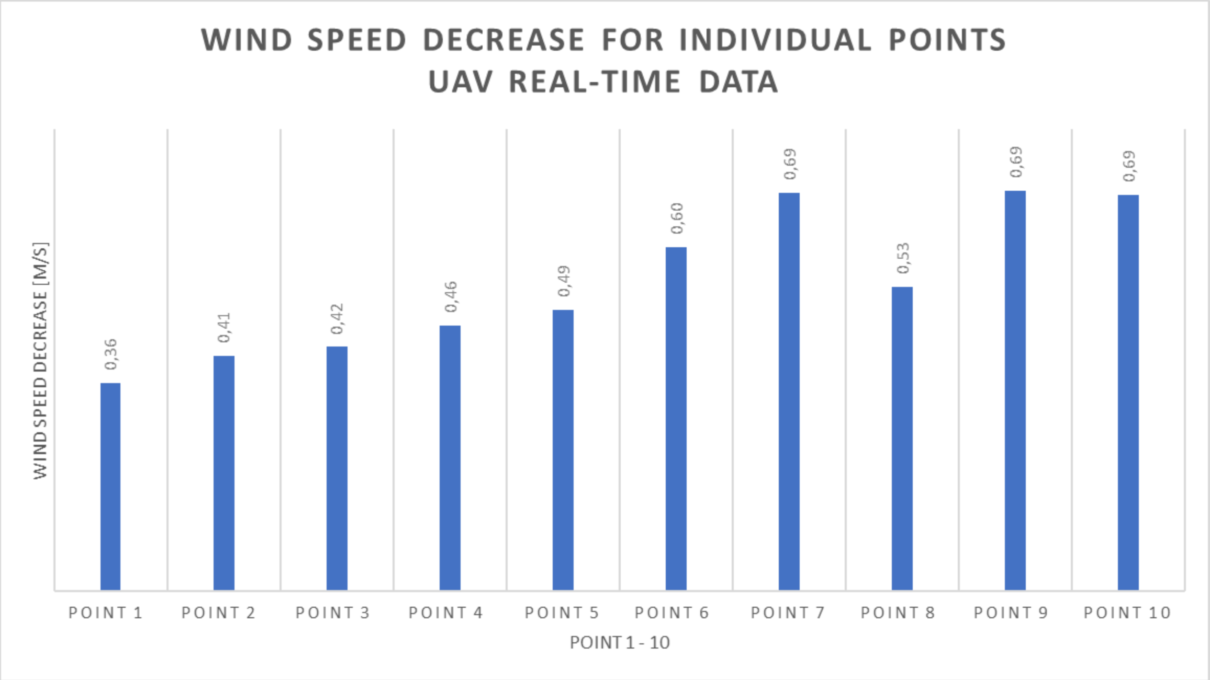

Table 25: Percentage Decrease in Wind Speed at Measurement Points: In-Situ Observations

5.5.6 Comparison with numerical simulation

5.5.6.1 Single Building Scenario

To investigate the impact of building height and wind speed on the near-field wind environment, a series of numerical simulations were conducted using the ENVI-met software. Four distinct building heights (5 m, 10 m, 15 m, and 20 m) were modelled, each subjected to five different wind speeds ranging from 2 m/s to 10 m/s, resulting in a total of 20 simulations (described in detail in section 5.3.1).

For each simulation output, a comparative analysis was performed between the initial wind speed and the wind speed measured behind the building at 10 specific points. These points were strategically chosen to capture the spatial variation of the wind field, with two altitudes (1/2 building height and building height) and five distances from the building (5 m, 10 m, 15 m, 20 m, and 25 m). The percentage decrease in wind speed at each point relative to the initial wind speed was calculated and is presented in Table 26.

Table 26: Decrease in Wind Speed, altitude = ½ building height (ENVI-met simulation, Single-building scenario)

Building height	**Starting Wind speed**	**Point 1**	**Point 2**	**Point 3**	**Point 4**	**Point 5**
5 m	2 m/s	0.15 V_{REF}	0.33 V_{REF}	0.50 V_{REF}	0.60 V_{REF}	0.65 V_{REF}
5 m	4 m/s	0.13 V_{REF}	0.25 V_{REF}	0.38 V_{REF}	0.45 V_{REF}	0.50 V_{REF}
5 m	6 m/s	0.12 V_{REF}	0.25 V_{REF}	0.30 V_{REF}	0.42 V_{REF}	0.48 V_{REF}
5 m	8 m/s	0.11 V_{REF}	0.21 V_{REF}	0.34 V_{REF}	0.43 V_{REF}	0.50 V_{REF}
5 m	10 m/s	0.10 V_{REF}	0.24 V_{REF}	0.32 V_{REF}	0.42 V_{REF}	0.49 V_{REF}
10 m	2 m/s	0.05 V_{REF}	0.30 V_{REF}	0.50 V_{REF}	0.55 V_{REF}	0.60 V_{REF}
10 m	4 m/s	0.08 V_{REF}	0.20 V_{REF}	0.30 V_{REF}	0.40 V_{REF}	0.45 V_{REF}
10 m	6 m/s	0.17 V_{REF}	0.27 V_{REF}	0.38 V_{REF}	0.43 V_{REF}	0.48 V_{REF}
10 m	8 m/s	0.10 V_{REF}	0.18 V_{REF}	0.29 V_{REF}	0.40 V_{REF}	0.45 V_{REF}
10 m	10 m/s	0.10 V_{REF}	0.19 V_{REF}	0.29 V_{REF}	0.41 V_{REF}	0.52 V_{REF}
15 m	2 m/s	0.10 V_{REF}	0.25 V_{REF}	0.50 V_{REF}	0.60 V_{REF}	0.73 V_{REF}
15 m	4 m/s	0.03 V_{REF}	0.20 V_{REF}	0.33 V_{REF}	0.40 V_{REF}	0.50 V_{REF}
15 m	6 m/s	0.05 V_{REF}	0.17 V_{REF}	0.23 V_{REF}	0.30 V_{REF}	0.43 V_{REF}
15 m	8 m/s	0.08 V_{REF}	0.18 V_{REF}	0.26 V_{REF}	0.44 V_{REF}	0.48 V_{REF}
15 m	10 m/s	0.08 V_{REF}	0.17 V_{REF}	0.26 V_{REF}	0.36 V_{REF}	0.45 V_{REF}
20 m	2 m/s	0.10 V_{REF}	0.23 V_{REF}	0.45 V_{REF}	0.55 V_{REF}	0.65 V_{REF}
20 m	4 m/s	0.08 V_{REF}	0.18 V_{REF}	0.28 V_{REF}	0.40 V_{REF}	0.50 V_{REF}
20 m	6 m/s	0.12 V_{REF}	0.22 V_{REF}	0.37 V_{REF}	0.47 V_{REF}	0.53 V_{REF}
20 m	8 m/s	0.10 V_{REF}	0.18 V_{REF}	0.29 V_{REF}	0.44 V_{REF}	0.48 V_{REF}
20 m	10 m/s	0.09 V_{REF}	0.19 V_{REF}	0.28 V_{REF}	0.45 V_{REF}	0.48 V_{REF}
Average		0.10 V_{REF}	0.22 V_{REF}	0.34 V_{REF}	0.45 V_{REF}	0.52 V_{REF}

Table 27: Percentage Decrease in Wind Speed, altitude = building height (ENVI-met simulation, Single-building scenario)

Building height	**Starting Wind speed**	**Point 6**	**Point 7**	**Point 8**	**Point 9**	**Point 10**
5 m	2 m/s	0.60 V_{REF}	0.60 V_{REF}	0.63 V_{REF}	0.65 V_{REF}	0.70 V_{REF}
5 m	4 m/s	0.40 V_{REF}	0.41 V_{REF}	0.43 V_{REF}	0.53 V_{REF}	0.58 V_{REF}
5 m	6 m/s	0.38 V_{REF}	0.42 V_{REF}	0.43 V_{REF}	0.50 V_{REF}	0.53 V_{REF}
5 m	8 m/s	0.39 V_{REF}	0.40 V_{REF}	0.43 V_{REF}	0.48 V_{REF}	0.53 V_{REF}
5 m	10 m/s	0.40 V_{REF}	0.44 V_{REF}	0.45 V_{REF}	0.49 V_{REF}	0.56 V_{REF}
10 m	2 m/s	0.50 V_{REF}	0.60 V_{REF}	0.65 V_{REF}	0.70 V_{REF}	0.75 V_{REF}
10 m	4 m/s	0.43 V_{REF}	0.50 V_{REF}	0.53 V_{REF}	0.55 V_{REF}	0.60 V_{REF}
10 m	6 m/s	0.50 V_{REF}	0.52 V_{REF}	0.53 V_{REF}	0.58 V_{REF}	0.67 V_{REF}
10 m	8 m/s	0.43 V_{REF}	0,4 V_{REF}	0.46 V_{REF}	0.48 V_{REF}	0.51 V_{REF}
10 m	10 m/s	0.46 V_{REF}	0.48 V_{REF}	0.50 V_{REF}	0.54 V_{REF}	0.62 V_{REF}
15 m	2 m/s	0.50 V_{REF}	0.60 V_{REF}	0.65 V_{REF}	0.75 V_{REF}	0.85 V_{REF}
15 m	4 m/s	0.50 V_{REF}	0.55 V_{REF}	0.58 V_{REF}	0.65 V_{REF}	0.73 V_{REF}
15 m	6 m/s	0.47 V_{REF}	0.50 V_{REF}	0.52 V_{REF}	0.58 V_{REF}	0,67 V_{REF}

Building height	Starting Wind speed	Point 6	Point 7	Point 8	Point 9	Point 10
15 m	8 m/s	0.48 V_{REF}	0.50 V_{REF}	0.54 V_{REF}	0.60 V_{REF}	0.64 V_{REF}
15 m	10 m/s	0.47 V_{REF}	0.50 V_{REF}	0.52 V_{REF}	0.57 V_{REF}	0.67 V_{REF}
20 m	2 m/s	0.60 V_{REF}	0.65 V_{REF}	0.70 V_{REF}	0.78 V_{REF}	0.85 V_{REF}
20 m	4 m/s	0.50 V_{REF}	0.55 V_{REF}	0.58 V_{REF}	0.63 V_{REF}	0.73 V_{REF}
20 m	6 m/s	0.47 V_{REF}	0.50 V_{REF}	0.53 V_{REF}	0.60 V_{REF}	0.70 V_{REF}
20 m	8 m/s	0.50 V_{REF}	0.53 V_{REF}	0.55 V_{REF}	0.60 V_{REF}	0.68 V_{REF}
20 m	10 m/s	0.50 V_{REF}	0.52 V_{REF}	0.55 V_{REF}	0.58 V_{REF}	5.65 V_{REF}
Average		0.47 V_{REF}	0.51 V_{REF}	0.54 V_{REF}	0.59 V_{REF}	0,66 V_{REF}

This systematic comparison allows for a quantitative assessment of the wind speed attenuation caused by the building's presence, providing valuable insights into the influence of building height and wind speed on the near-field flow patterns.

Furthermore, these simulation results are compared with the real-time data collected during the demonstration mission, as illustrated in Figure 52, to assess the accuracy and predictive capabilities of the numerical models.

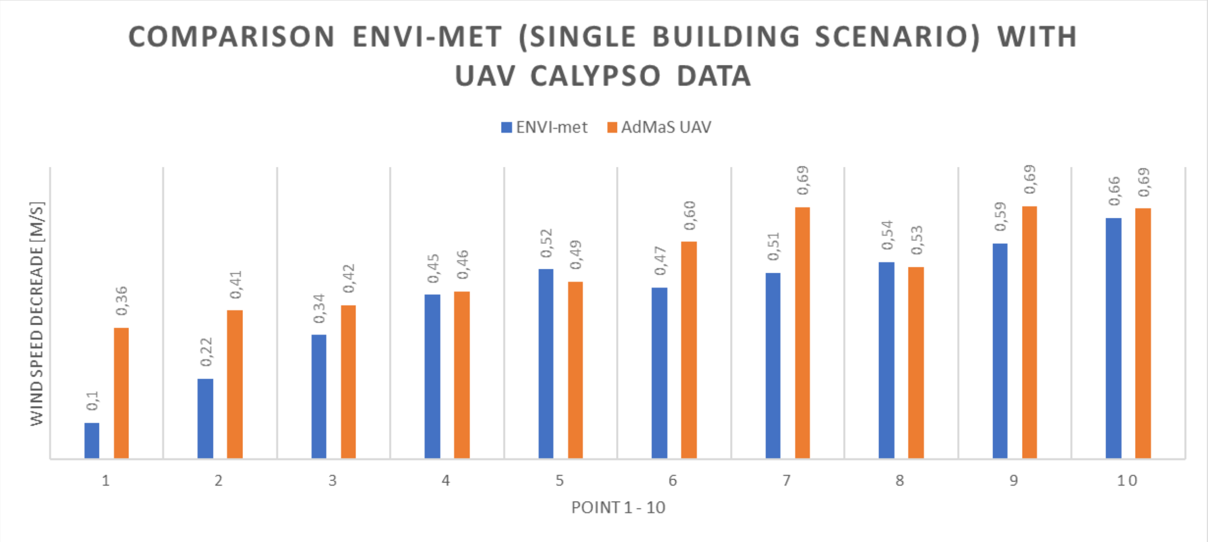

Figure 52: Comparison of wind speed decrease (ENVI-met Single building scenario compared to UAV real-time data)

5.5.6.2 AdMaS Scenario

Table 28: Decrease in Wind Speed, altitude = ½ building height (ENVI-met simulation, AdMaS scenario)

Starting Wind speed (10 m AGL)	*Point 1*	*Point 2*	*Point 3*	*Point 4*	*Point 5*
2 m/s	0.15 V_{REF}	0.23 V_{REF}	0.39 V_{REF}	0.50 V_{REF}	0,55 V_{REF}
4 m/s	0.10 V_{REF}	0.15 V_{REF}	0.25 V_{REF}	0.38 V_{REF}	0,50 V_{REF}
6 m/s	0.10 V_{REF}	0.14 V_{REF}	0.18 V_{REF}	0.32 V_{REF}	0,43 V_{REF}
Average decrease	0.12 V_{REF}	0.17 V_{REF}	0.27 V_{REF}	0.40 V_{REF}	0,49 V_{REF}

Table 29: Percentage Decrease in Wind Speed, altitude = building height (ENVI-met simulation, AdMaS scenario)

Starting Wind speed (10 m AGL)	***Point 6***	***Point 7***	***Point 8***	***Point 9***	***Point 10***
2 m/s	0.60 V_{REF}	06.8 V_{REF}	0.70 V_{REF}	0.78 V_{REF}	0.80 V_{REF}
4 m/s	0.53 V_{REF}	0.58 V_{REF}	0.58 V_{REF}	0.66 V_{REF}	0.70 V_{REF}
6 m/s	0.47 V_{REF}	0.55 V_{REF}	0.53 V_{REF}	0.58 V_{REF}	0.63 V_{REF}
Average decrease	0.53 V_{REF}	0.60 V_{REF}	0.60 V_{REF}	0.67 V_{REF}	0.71 V_{REF}

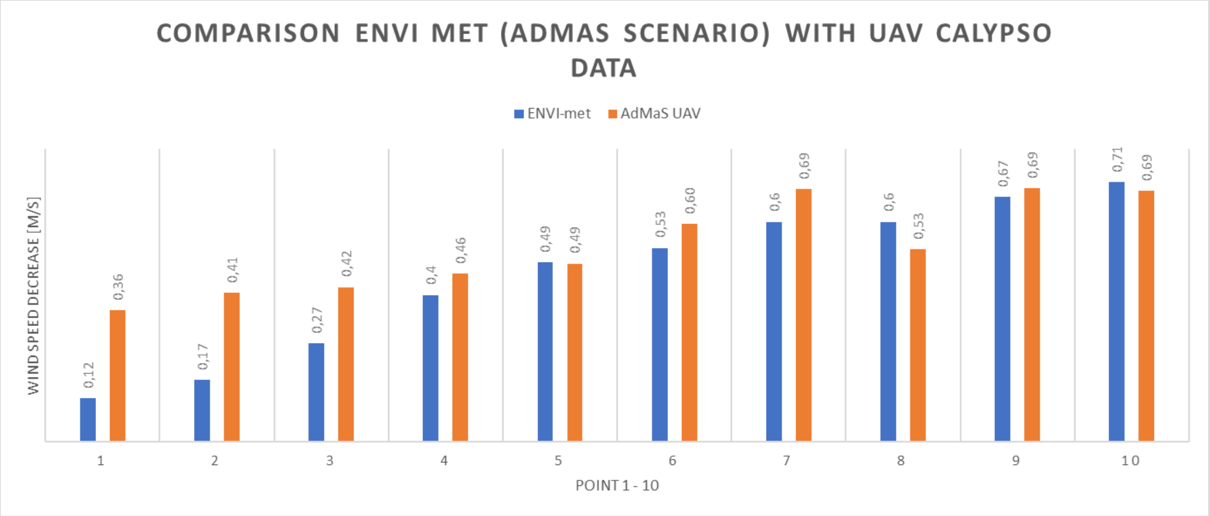

Figure 53: Comparison of wind speed decrease (ENVI-met AdMaS scenario compared to UAV real-time data)

5.5.7 Initial results

Table 30: Percentage deviation between Output of Numerical simulation ENVI-met AdMaS scenario and UAV real-time data

Point	***ENVI-met Numerical simulation (AdMaS scenario)***	***UAV real-time data (Calypso)***	***Percentage Deviation [%]***
1	0.12	0.36	66,7
2	0.17	0.41	58,3
3	0.27	0.42	36,1
4	0.4	0.46	13,0
5	0.49	0.49	0,6
6	0.53	0.60	11,0
7	0.6	0.69	13,0
8	0.6	0.53	13,9
9	0.67	0.69	3,3
10	0.71	0.69	3,5

The comparative analysis between ENVI-met simulations and real-time UAV data reveals a promising level of agreement, particularly when considering the limitations of the employed sensor technology. While the simulations generally tend to underestimate wind speeds compared to the in-situ measurements, this discrepancy is primarily observed at points where the measured wind speeds fell below the Calypso anemometer's threshold of 1 m/s.

For all measurement points where wind speeds exceeded this threshold, the deviations between simulated and measured values remained consistently below 13.9%. This remarkable agreement underscores the effectiveness of the ENVI-met simulations in capturing the overall wind field dynamics in the AdMaS scenario, especially for wind speeds within the reliable measurement range of the Calypso anemometer.

The observed discrepancies at low wind speeds highlight the importance of sensor selection and data interpretation in experimental validation of numerical models. While the Calypso anemometer proved valuable for assessing wind speeds above its threshold, future research could further enhance the accuracy and resolution of turbulence characterization by employing higher-precision anemometers capable of capturing the full spectrum of wind dynamics, particularly in regions of complex flow interactions.

Overall, the results of this comparative analysis provide compelling evidence for the reliability and predictive capabilities of ENVI-met simulations in assessing wind flow patterns and turbulence within the built environment. The observed agreement between simulations and real-time measurements, even with the constraints of a low-cost sensor, underscores the potential of this approach for informing UAV operations and urban planning strategies aimed at mitigating turbulence-related risks.

5.6 EDR formula

The selection of an appropriate method for estimating the Eddy Dissipation Rate (EDR) is pivotal in turbulence characterization, particularly in the context of UAV-based measurements. Following a comprehensive review of various EDR calculation possibilities (described in chapter 4.3.), the structure function method emerged as the most suitable choice for this investigation, considering the specific constraints and objectives of the study. The structure function method, grounded in Kolmogorov's turbulence theory, offers several advantages that align well with the requirements of UAV-based turbulence measurements. The method directly utilizes the time series of velocity fluctuations, readily obtainable from the sonic anemometer onboard the UAV. This eliminates the need for complex instrumentation or additional data processing steps, making it well-suited for implementation on smaller UAV platforms with limited payload and computational capabilities.

The structure function method is relatively insensitive to the sampling rate of the anemometer, making it adaptable to the 1 Hz sampling rate of the low-cost Calypso sensor used in this study. This robustness contrasts with other methods, such as those based on spectral analysis, which often require higher sampling rates to accurately capture the full range of turbulent fluctuations. As highlighted in [124] the inertial dissipation method, upon which the structure function approach is based, has been successfully applied to estimate EDR from sonic anemometer data, even at lower frequencies. The structure function method is firmly rooted in the well-established theoretical framework of Kolmogorov's turbulence theory, providing a solid physical basis for interpreting the results. The reliance on the second-order structure function, which directly relates to the turbulent kinetic energy dissipation, ensures a sound theoretical underpinning for the EDR estimation.

The applicability of the structure function method for EDR estimation using sonic anemometer data has been demonstrated in previous study [124]. While focused on a high-frequency (20 Hz) sonic anemometer [124] mounted on a static platform, their findings support the validity of the inertial dissipation method across different sampling rates.

This study extends the application of this method to a low-cost, 1 Hz anemometer integrated onto a dynamic UAV platform, showcasing its versatility and potential for broader applications.

The structure function method was selected for EDR calculation in this study due to its direct reliance on velocity fluctuation measurements, robustness to sensor limitations, strong theoretical foundation, and demonstrated applicability in previous research. While acknowledging the differences in sensor specifications and measurement platforms compared to prior work, this approach represents a practical and effective solution for estimating turbulence using affordable and readily available instrumentation on smaller UAVs.

5.6.1 EDR calculation

The eddy dissipation rate (EDR) can be determined based on Kolmogorov's theory of turbulence, which postulates a specific relationship between EDR and spatial separation within the inertial subrange for isotropic turbulence.

The EDR estimation method (EDR) in this study utilizes the second-order structure function (SF) and incorporates Taylor's frozen hypothesis to express EDR as a function of temporal separation.

$$\mathrm{EDR} = \left(\frac{1}{U}\right)^{1/3} \left[\frac{D_u(\tau)\tau^{-2/3}}{C_K}\right]^{1/2}$$

Equation 26

Where:

- U is the mean streamwise wind speed
- $D_u(\tau)$ is the second-order structure function
- τ is the temporal separation (1.0 and 2.0 seconds)
- Ck is the Kolmogorov constant, a crucial parameter in this calculation, set to 0.52 s^-1, consistent with values used in previous research

The second-order structure function ($D_u(\tau)$) is calculated as follows:

$$Du(\tau)=\langle[u(t+\tau) - u(t)]2\rangle$$

Where:

- u represents the instantaneous streamwise component of the wind velocity
- t represents time
- τ represents the temporal separation (between 1.0 and 2.0 seconds)
- The angle brackets 〈 〉 denote the ensemble average, which signifies averaging over multiple realizations or time intervals.

The inertial subrange was defined as the range of temporal separations 1.0 and 2.0 seconds, and a 120-second window was employed for the calculation of the structure function.

5.6.2 EDR results from AdMaS data

Table 31: Summary of all 60 tests and the result of EDR calculation

No.	Average Wind speed (120 s)	EDR	Velocity fluctuation MIN	Velocity fluctuation MAX	Velocity fluctuation SPECTRUM	ICAO
1	1.38	0.289	-0.77	0.63	1.4	MODERATE
2	1.92	0.263	-1.22	1.28	2.5	MODERATE
3	1.86	0.301	-1.06	1.44	2.5	MODERATE
4	1.51	0.48	-0.91	1.59	2.5	SEVERE
5	1.61	0.476	-1	1.7	2.7	SEVERE
6	2.17	0.042	-0.37	0.03	0.4	NULL
7	2.2	0.133	-0.9	0.9	1.8	LIGHT
8	1.52	0.160	-0.62	0.68	1.3	LIGHT
9	2.54	0.102	-0.34	0.56	0.9	LIGHT
10	2.9	0.038	-0.2	0.2	0.4	NUL
11	1.48	0.343	-0.97	1.13	2.1	MODERATE
12	1.83	0.367	-1.13	1.47	2.6	MODERATE
13	1.74	0.41	-1.04	1.86	2.9	MODERATE
14	2.02	0.387	-0.92	1.28	2.2	MODERATE
15	2.3	0.316	-1.6	1.3	2.9	MODERATE
16	3.42	0.345	-2.62	1.38	4	MODERATE
17	4.38	0.276	-1.68	1.22	2.9	MODERATE
18	3.51	0.292	-1.71	1.19	2.9	MODERATE
19	4.04	0.216	-1.74	1.66	3.4	MODERATE
20	2.73	0.206	-1.13	0.97	2.1	MODERATE
21	1.7	0.247	-0.8	1	1.8	MODERATE

22	1.58	0.353	-1.08	1.52	2.6	MODERATE
23	1.76	0.406	-1.16	2.04	3.2	MODERATE
24	2.37	0.426	-1.77	1.63	3.4	MODERATE
25	2.95	0.478	-2.25	1.76	4	SEVERE
26	3.59	0.338	-1.79	1.41	3.2	MODERATE
27	5.56	0.328	-1.56	1.64	3.2	MODERATE
28	3.27	0.421	-2.07	-1.63	3.7	MODERATE
29	3.07	0.315	-1.57	1.23	2.8	MODERATE
30	3.09	0.394	-2.19	3.51	5.7	MODERATE
31	0.79	0.465	-0.86	1.24	2.1	SEVERE
32	0.86	0.45	-1.46	1.54	3	SEVERE
33	1.17	0.403	-1.23	1.07	2.3	MODERATE
34	1.21	0.398	-1.14	0.96	2.1	MODERATE
35	1.37	0.345	-1.29	1.11	2.4	MODERATE
36	1.87	0.565	-1.87	1.93	3.8	SEVERE
37	1.9	0.327	-1.1	1.1	2.2	MODERATE
38	1.77	0.468	-1.17	1.13	2.3	SEVERE
39	2.79	0.389	-1.59	1.31	2.9	MODERATE
40	2.79	0.225	-0.59	0.71	1.3	MODERATE
41	1.93	0.447	-1.33	0.67	2	MODERATE
42	2.6	0.426	-2.6	1.3	3.9	MODERATE
43	2	0.507	-1.2	1.7	2.9	SEVERE
44	2.38	0.409	-1.28	1.52	2.8	MODERATE
45	2.87	0.387	-2.17	1.34	3.5	MODERATE
46	1.07	0.189	-0.57	0.63	1.2	LIGHT
47	1	0.214	-0.5	0.6	1.1	MODERATE
48	0.92	0.3	-0.92	0.68	1.6	MODERATE
49	1.22	0.176	-0.72	0.48	1.2	LIGHT
50	1.09	0.175	-0.59	0.51	1.1	LIGHT
51	1.5	0.149	-0.6	0.9	1.5	LIGHT
52	1.16	0.147	-0.46	0.54	1	LIGHT
53	1.07	0.179	-0.47	0.63	1.1	LIGHT
54	1.63	0.167	-0.73	0.47	1.2	LIGHT
55	1.67	0.14	-0.47	0.43	0.9	LIGHT
56	1.27	0.164	-0.37	0.43	0.8	LIGHT
57	1.58	0.175	-0.58	0.62	1.2	LIGHT
58	1.6	0.151	-0.5	0.5	1	LIGHT
59	1.55	0.137	-0.45	0.65	1.1	LIGHT
60	1.47	0.167	-0.77	0.83	1.6	LIGHT

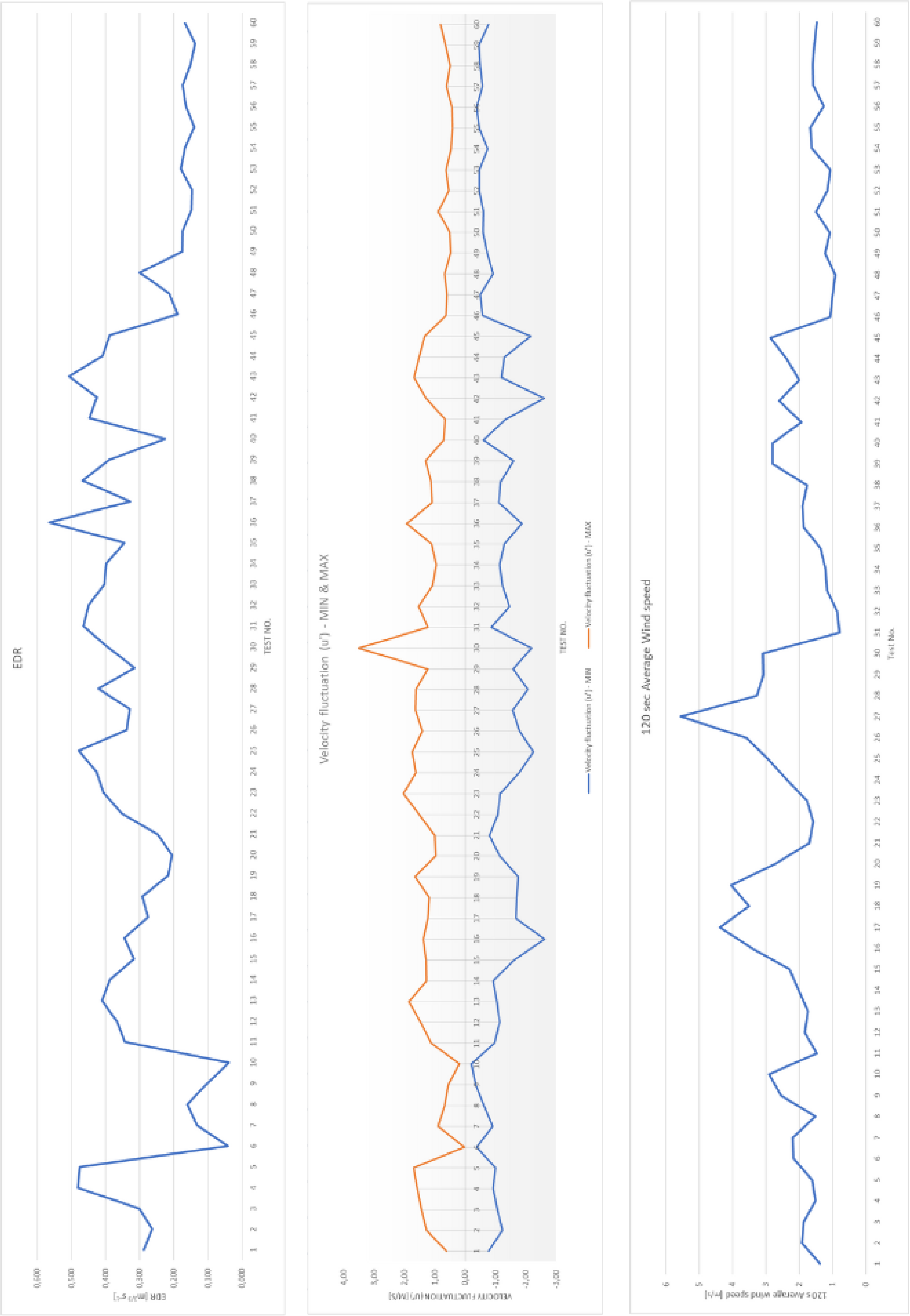

Figure 54: EDR results compared to Velocity fluctuations

The presented figure illustrates the relationships between Eddy Dissipation Rate (EDR), average wind speed, and velocity fluctuation spectrum across 60 hovering tests. Each test, conducted for 120 seconds, captured real-time wind data using a low-cost sonic anemometer integrated onto an unmanned aerial vehicle (UAV). The EDR values were calculated using a condensed structure function method adapted for the 1 Hz sampling rate of the sensor.

Key Observations:

- **EDR and Wind Speed:** The first graph reveals a lack of direct correlation between EDR and average wind speed. This suggests that the intensity of turbulence is not solely determined by the magnitude of the wind speed but is influenced by other factors.
- **EDR and Velocity Fluctuation:** The second graph demonstrates a clear dependency between EDR and velocity fluctuation spectrum. Low fluctuation values correspond to minimal EDR, often categorized as 'zero' according to ICAO standards. Conversely, significant velocity fluctuations are associated with a rapid increase in EDR.
- **Implications for UAV Operations:** These observations highlight the potential of utilizing a low-cost sonic anemometer on UAVs to assess turbulence in real-time, aligning with the ICAO categorization framework. However, to realize the full potential of this approach, widespread adoption of in-situ EDR measurement and data sharing among UAV operators is crucial, similar to the practices employed in commercial aviation.

5.6.3 Initial result

The data shared contains the results of 60 hovering modes, each lasting 120 seconds. For each mode, average wind speed, EDR, minimum and maximum velocity fluctuations, velocity fluctuation spectrum, and the corresponding ICAO turbulence categorization were analysed.

This study successfully demonstrates the feasibility of estimating EDR using a basic sensor on a UAV platform through a condensed calculation method. The findings challenge the conventional notion that wind speed alone dictates turbulence intensity, emphasizing the role of velocity fluctuations in turbulence characterization. This research paves the way for a paradigm shift in UAV turbulence awareness, advocating for a collaborative approach where real-time turbulence data is shared among UAVs, thus enabling safer and more efficient operations in dynamic environments.

6 SUMMARY OF RESULTS

6.1 NUMERICAL SIMULATION

The initial phase of numerical simulations, conducted using Star CCM+ software, successfully identified the locations and magnitudes of turbulent vortices generated in the vicinity of a single building. However, the software encountered limitations, including frequent errors and a suboptimal user experience. The primary impetus for transitioning to ENVI-met stemmed from the limitations in Star CCM+'s domain capabilities. While it could handle simulations for a single building, it was unable to accommodate the larger and more complex AdMaS campus environment, which was essential for the second phase of the research.

Furthermore, the specific research objectives did not necessitate a highly detailed mesh resolution (in centimetres). The primary goal was to determine a safe distance for UAV operation near buildings, for which a 1-meter grid resolution in ENVI-met was deemed sufficient. The decision to switch to ENVI-met was further supported by recommendations from colleagues and the observation of its successful application in similar research contexts. The software's user-friendly interface and ability to handle larger-scale simulations without errors ultimately made it the more suitable choice for this investigation.

The first scenario (Single building) of main numerical simulations, conducted using ENVI-met software, successfully identified the locations and magnitudes of downstream wake and vertical updrafts zone generated in the vicinity of a single building. The analysis revealed a clear dependency between building height, wind speed, and the extent of the downstream wake and vertical updraft zones, which pose potential hazards for UAS operations. The simulations demonstrated that taller buildings and higher wind speeds result in larger and more pronounced wake and updraft zones. Empirical formulas (Equations calculated downstream wake and vertical updrafts) were derived to predict the size of these dangerous zones based on building height and wind speed, exhibiting high accuracy with deviations consistently below 5% and 6.1%, respectively. The establishment of these predictive formulas represents a significant contribution to UAS safety, providing a quantitative tool for assessing potential turbulence hazards in the vicinity of buildings.

The subsequent phase (AdMaS scenario) of numerical simulations, utilizing the ENVI-met software, focused on modelling the complex urban environment of the AdMaS research centre. This scenario aimed to validate the empirical formulas derived from the single-building simulations and to generate a baseline model for comparison with real-time turbulence data. The ENVI-met simulations successfully captured the intricate wind flow patterns and turbulence distribution within the AdMaS campus, accounting for the interactions between multiple buildings, vegetation, and other terrain features. The comparison between simulated and predicted values for the downstream wake and vertical updraft distances near Building H showed a favourable overall agreement [53], further validating the applicability of the empirical formulas in real-world scenarios [54].

The minor observed discrepancies, particularly in the vertical updraft distance at certain wind speeds, can be attributed to two primary factors:

a) The inherent complexities of modeling turbulence in urban environments, which necessitate continuous refinement of predictive models.
b) The limitations of the measurement setup, including the Calypso anemometer's sensitivity threshold at low wind speeds and the variability in flight altitude (± 1 m) during the building-height level flights. The latter was due to the pilot's visual estimation challenges in maintaining a precise altitude while navigating in close proximity to the building.

6.2 DEMONSTRATION MISSION AdMaS

The Calypso ultrasonic anemometer, chosen for its affordability and ease of integration, underwent rigorous wind tunnel testing to assess its accuracy and precision. The results confirmed its suitability for measuring horizontal wind speeds above 3 m/s, a critical range for safe UAS operations. The validation process ensured the reliability of the sensor data used in subsequent turbulence analysis.

The Calypso anemometer was seamlessly integrated onto the DJI M100 UAS platform, enabling in-situ wind measurements during flight. The demonstration mission at the AdMaS center involved a series of 60 meticulously planned hover tests at various altitudes and distances from Building H. These tests, conducted under diverse wind conditions with prevailing northerly winds and speeds ranging from 1.51 to 3.92 m/s, provided a rich dataset for turbulence characterization and model validation.

The Davis Vantage Pro2 meteorological station, deployed at the AdMaS center, served as a ground-based reference for validating the UAV's wind measurements. The station's high-precision meteorological data, including wind speed, temperature, humidity, and other relevant parameters, enabled a direct comparison with the UAV's onboard measurements. The observed high degree of concordance between the two datasets further established the reliability of the UAV-based measurements and the overall experimental setup.

6.3 EDR calculation

After a thorough evaluation of various EDR calculation methods, the structure function method was selected due to its direct reliance on velocity fluctuation measurements, robustness to the low sampling rate of the Calypso anemometer, and strong theoretical foundation in Kolmogorov's turbulence theory.
The structure function method was adapted to accommodate the 1 Hz sampling rate of the Calypso sensor by adjusting the range of temporal separation and extending the analysis time window. This adaptation ensured the accurate estimation of EDR from the UAV's in-situ measurements.

The calculated EDR values from the AdMaS mission data revealed a lack of direct correlation between EDR and average wind speed, highlighting the complex interplay of factors influencing turbulence intensity. A clear dependency was observed between EDR and velocity fluctuation spectrum, with higher fluctuations leading to increased EDR. This observation underscores the importance of considering both mean wind speed and its fluctuations when assessing turbulence levels.

6.4 Definition of Thesis Objectives

This subchapter contains a clear definition of all the objectives of the dissertation that were determined in chapter 3 “AIM AND OBJECTIVES “.

Table 32: Objectives of the dissertation.

No.	Thesis objective	Discussed in the chapter
1.	Description of the issue of meteorological forecasting for civil aviation.	2.1
2.	Review of requirements and shortcomings of meteorological services for future operation of unmanned aerial vehicles (UAVs).	2.2
3.	Processing of an analysis in the form of a questionnaire to verify the shortcomings of current meteorological services for unmanned operations in the Central European region.	2.2
4.	Based on previous research and own analysis, identify the shortcomings of current meteorological forecasts for future operation of unmanned aerial vehicles.	2.2
5.	Test flights to compare basic meteorological parameters of hyperlocal meteorological forecasts with directly measured data (using a quadcopter).	2.3
6.	Selection of the segment of interest from the summary list of weaknesses of current meteorological forecasts.	2.2
7.	Processing a review of possible tools to eliminate the identified shortcomings.	4.4, 5.2
8.	Identification and selection of a turbulence detection method.	4.3
9.	Process numerical simulations of turbulence in a built-up urban environment with an integrated unmanned aerial vehicle and subsequent interpretation of the obtained results and their use in creating a concept for a demonstration mission.	5.1, 5.3
10.	Create a scenario for test flights to determine the relationship between eddy dissipation rate and the impact on the control of an unmanned aerial vehicle.	5.5
11.	Definition of limits to ensure safe unmanned operation	6

7 CONCLUSION

This dissertation presents a multifaceted approach to advance the operational estimation of Eddy Dissipation Rate (EDR) using Unmanned Aerial Systems (UASs) and to define dangerous zones in low-altitude urban environments. The research journey began with a comprehensive investigation into the existing meteorological services for UAV operations, revealing critical gaps in the provision of accurate and timely weather information, particularly concerning wind and turbulence. A survey of UAV operators further underscored these shortcomings, highlighting the need for improved meteorological data to ensure safe and efficient UAV operations in the increasingly complex urban airspace.

Driven by these findings, the research embarked on a multi-pronged approach to address the identified challenges. Initial explorations into indirect measurement techniques, while promising in theory, faced limitations due to restricted access to critical flight data on modern UAVs. This led to the adoption of a direct measurement approach, utilizing a low-cost sonic anemometer integrated onto a UAV platform. The accuracy and precision of this sensor were rigorously validated through wind tunnel testing, establishing its suitability for in-situ turbulence assessment.

In parallel, numerical simulations were conducted using ENVI-met software to model wind flow patterns and turbulence distribution around buildings. These simulations served to validate empirically derived formulas for predicting hazardous zones near buildings and provided a baseline for comparison with real-time turbulence data collected during UAV flights. The subsequent AdMaS demonstration mission, conducted in a real-world urban setting, further validated the numerical models and the adapted EDR calculation methodology, showcasing the robustness and predictive capabilities of the developed tools.

The successful validation of the Calypso "Ultrasonic Portable Mini" anemometer, coupled with the adaptation of the structure function method for EDR calculation at a 1 Hz sampling rate, establishes a novel and cost-effective approach for in-situ turbulence assessment on UAS platforms. This methodology addresses the critical need for accessible turbulence measurement solutions for smaller UAS operators, who often face limitations in payload and budget that preclude the use of expensive, high-frequency sensors. The demonstrated accuracy of the Calypso anemometer for wind speeds above its threshold, coupled with the robustness of the structure function method, highlights the potential for widespread adoption of this approach in the UAV industry.

The empirically derived formulas for estimating downstream wake distances and building edge updrafts, rigorously validated through detailed numerical simulations and real-time UAV data collected during the AdMaS demonstration mission, represent a significant advancement in UAS safety guidelines. These formulas empower UAS operators with a quantitative tool for assessing potential turbulence hazards in the vicinity of buildings, enabling informed decision-making regarding flight paths and altitudes. The strong agreement between the predicted and measured values, even in the complex urban environment of the AdMaS centre, underscores the efficacy and practical applicability of these formulas.

The AdMaS demonstration mission, conducted in a real-world urban setting, served as a pivotal step in validating the numerical models and the adapted EDR calculation methodology. The comparison of real-time turbulence data with simulated results not only confirmed the accuracy of the models but also provided valuable insights into the intricate flow patterns and turbulence dynamics near buildings. The observed discrepancies at low wind speeds, attributed to both sensor limitations and the inherent complexities of modelling turbulence in urban canyons, highlight the need for continued research and development in this field. However, the overall agreement between the simulations and measurements, particularly for wind speeds above the sensor threshold, reinforces the robustness and predictive capabilities of the developed models.

The analysis of EDR values calculated from the UAV measurements revealed a lack of direct correlation between EDR and average wind speed, underscoring the multi-faceted nature of turbulence. The observed dependency between EDR and velocity fluctuation spectrum further emphasizes the importance of considering both mean wind speed and its fluctuations when assessing turbulence levels. This finding challenges the conventional reliance on wind speed alone as a turbulence indicator and advocates for a more nuanced approach that incorporates the dynamic nature of wind flow.

Beyond the immediate validation goals, this research lays a strong foundation for enhancing the safety and operational efficiency of UASs within the increasingly complex urban airspace. The successful implementation of a low-cost, UAV-based turbulence estimation system, coupled with the development of predictive models for hazardous zones, has the potential to increase safety level of UAS operations. By enabling real-time turbulence awareness and informed decision-making, this research contributes to the safe and seamless integration of UAVs into the airspace of the future, unlocking their full potential for a wide range of applications.

Future investigations will focus on expanding field experiments to diverse urban settings, incorporating additional meteorological sensors for comprehensive data acquisition, and integrating our findings into actionable tools and decision support systems for UAS operators. By addressing the critical gap in meteorological information for UASs operating at low altitudes, this research has the potential to significantly improve the safety, reliability, and overall capabilities of UASs in various applications, while also fostering their seamless integration into the complex airspace of the future.

Bibliography

[1] Ahmed, F., Mohanta, J.C., Keshari, A. et al., "Recent Advances in Unmanned Aerial Vehicles: A Review", Arab J Sci Eng 47, 7963–7984 (2022). https://doi.org/10.1007/s13369-022-06738-0

[2] SESAR Joint Undertaking, "European drones outlook study," (2016). European_Drones_Outlook_Study_2016.pdf (sesarju.eu)

[3] M. Mazur, A. Wisniewski, and J. McMillan, "Clarity from above: PwC global report on the commercial applications of drone technology," (2016). clarity-from-above-pwc.pdf

[4] V. Alarcon, M. Garcia, F. Alarcon, A. Viguria, A. Martinez, D. Janisch, J. J. Acevedo, I. Maza, and A. Ollero, "Procedures for the integration of drones into the airspace based on u-space services," Aerospace, vol. 7, no. 9, p. 128, Sep. 2020. http://dx.doi.org/10.3390/aerospace7090128

[5] H. Shakhatreh, A. H. Sawalmeh, A. Al-Fuqaha, Z. Dou, E. Almaita, I. Khalil, N. S. Othman, A. Khreishah, and M. Guizani, "Unmanned aerial vehicles (uavs): a survey on civil applications and key research challenges," IEEE Access, vol. 7, p. 48572–48634, 2019. http://dx.doi.org/10.1109/ACCESS.2019.2909530

[6] M. Hatfield, C. Cahill, P. Webley, J. Garron, and R. Beltran, "Integration of unmanned aircraft systems into the national airspace system-efforts by the University of Alaska to support the FAA/NASA UAS traffic management program," Remote Sensing, vol. 12, no. 19, p. 3112, Sep. 2020. http://dx.doi.org/10.3390/rs12193112

[7] L. B. Cornman and W. N. Chan, "Summary of a workshop on integrating weather into unmanned aerial system traffic management," Bulletin of the American Meteorological Society, vol. 98, no. 10, p. ES257–ES259, Oct. 2017. http://dx.doi.org/10.1175/BAMS-D-16-0284.1

[8] Gao, Mozhou & Hugenholtz, Chris & Fox, Thomas & Kucharczyk, Maja & Barchyn, Thomas & Nesbit, Paul, "Weather constraints on global drone flyability", Scientific Reports, vol. 11. (2021). http://dx.doi.org/10.1038/s41598-021-91325-w

[9] G. Simó, J. Cuxart, M. A. Jiménez, D. Martínez-Villagrasa, R. Picos, A. López-Grifol, B. Martí, "Observed atmospheric and surface variability on heterogeneous terrain at the hectometer scale and related advective transports," Journal of Geophysical Research: Atmospheres, vol. 124, no. 16, p. 9407–9422, Aug. 2019. http://dx.doi.org/10.1029/2018JD030164

[10] Shelekhov, A. Afanasiev, E. Shelekhova, A. Kobzev, A. Tel'minov, A. Molchunov, and O. Poplevina, "Low-altitude sensing of urban atmospheric turbulence with UAV," Drones, vol. 6, no. 3, p. 61, Feb. 2022. http://dx.doi.org/10.3390/drones6030061

[11] S. Campbell, D. Clark, and J. Evans, "Preliminary weather information gap analysis for uas operations," Project Report ATC-437 (2017). Preliminary Weather Information Gap Analysis for UAS Operations (mit.edu)

[12] Annex 3 - Meteorological Service for International Air Navigation (17th ed.), International Civil Aviation Organization (July 2010). https://www.icao.int/airnavigation/IMP/Documents/Annex%203%20-%2075.pdf

[13] Letecký předpis Meteorologie L-3, Číslo změny 80, Úřad pro civilní letectví (12.08.2021).

https://aim.rlp.cz/predpisy/predpisy/dokumenty/L/L-3/data/print/L-3_cely.pdf

[14] S. Campbell, D. Clark, J. Evans, "Preliminary UAS Weather Research Roadmap", Project Report ATC-438, MIT Lincoln Laboratory (2017). Preliminary UAS Weather Research Roadmap (mit.edu)

[15] M. Doole, J. Ellerbroek, J. Hoekstra, A. Mennella, M. Onate, „Drone Information Service Requirements for U-Space", In 8th SESAR Innovation Days (2018). SIDs_2018_paper_34.pdf (sesarju.eu)

[16] R. Balážová, J. Hlinka, A. Belbachir and J. Svoboda, "Hyperlocal Weather Information for Drone Operations," 2024 New Trends in Civil Aviation (NTCA), Prague, Czech Republic (2024). http://dx.doi.org/10.23919/NTCA60572.2024.10517813

[17] Meteomatics, Meteorological data provider, The Global Leader in Weather Intelligence | Meteomatics

[18] CORDIS - EU research results, Horizon 2020, U-space for UAM, Grant agreement ID: 101017643, https://doi.org/10.3030/101017643

[19] J. T. Pasquier, J. Rausch, A. Stauch, and M. Fengler, "EURO1k: A high-resolution european weather model developed by meteomatics," (2023). http://dx.doi.org/10.5194/egusphere-egu23-16670

[20] J. Lauer and M. Fengler, "Meteodrones - Meteorological Planetary Boundary Layer Measurements by Vertical Drone Soundings," in EGU General Assembly Conference Abstracts, ser. EGU General Assembly Conference Abstracts, Apr. 2017, p. 2983. Meteodrones - Meteorological Planetary Boundary Layer Measurements by Vertical Drone Soundings - NASA/ADS (harvard.edu)

[21] S. Wier, "Interpolating between grids of meteorological data for afps," in Proc. 11th Int. Conf. on Interactive Information and Processing Systems for Meteorology, Oceanography, and Hydrology, Dallas, TX, Amer. Meteor. Soc., 1995, pp. 255–259.

[22] E. J. Dumas, "Small unmanned aircraft system (sUAS) measurements at the Oliver Springs airport," (2021). https://repository.library.noaa.gov/view/noaa/33875

[23] B. Guay, M. Fengler, and L. Hammerschmidt, "Improving nowcasts and forecasts via operational use of meteomatics meteodrones," (May 2023). http://dx.doi.org/10.5194/egusphere-egu23-8632

[24] D. G. Chechin, A. Y. Artamonov, N. E. Bodunkov, D. N. Zhivoglotov, D. V. Zaytseva, M. Y. Kalyagin, D. D. Kouznetsov, A. A. Kounashouk, A. M. Shevchenko, and A. A. Shestakova, "Experience of studying the turbulent structure of the atmospheric boundary layer using an unmanned aerial vehicle," Izvestiya, Atmospheric and Oceanic Physics, vol. 57, no. 5, p. 526–532, (Sep. 2021). http://dx.doi.org/10.1134/S0001433821050042

[25] J. Reuder and M. O. Jonassen, "First results of turbulence measurements in a wind park with the small unmanned meteorological observer SUMO," Energy Procedia, vol. 24, p. 176–185, 2012. http://dx.doi.org/10.1016/j.egypro.2012.06.099

[26] A. Rautenberg, J. Allgeier, S. Jung, and J. Bange, "Calibration procedure and accuracy of wind and turbulence measurements with five-hole probes on fixed-wing unmanned aircraft in the atmospheric boundary layer and wind turbine wakes," Atmosphere, vol. 10, no. 3, p. 124, (Mar. 2019). http://dx.doi.org/10.3390/atmos10030124

[27] H. Luce, L. Kantha, H. Hashiguchi, and D. Lawrence, “Estimation of turbulence parameters in the lower troposphere from ShUREX (2016–2017) UAV data,” Atmosphere, vol. 10, no. 7, p. 384, Jul. 2019. http://dx.doi.org/10.3390/atmos10070384

[28] B. Witte, R. Singler, and S. Bailey, “Development of an unmanned aerial vehicle for the measurement of turbulence in the atmospheric boundary layer,” Atmosphere, vol. 8, no. 10, p. 195, Oct. 2017. http://dx.doi.org/10.3390/atmos8100195

[29] NOAA, National Weather Service, Turbulence categorisation. turbulence.pdf (weather.gov)

[30] Williams, P. D., „Increased light, moderate, and severe clear-air turbulence in response to climate change“, Adv. Atmos. Sci., 34(5), 576–586 (2017). http://dx.doi.org/10.1007/s00376-017-6268-2

[31] A. Kolmogorov, “The Local Structure of Turbulence in Incompressible Viscous Fluid for Very Large Reynolds' Numbers”, Akademiia Nauk SSSR Doklady, vol. 30, pp. 301–305, (1941c). kolmogorov_1941.pdf (gibbs.science)

[32] Haverdings, H., and P. W. Chan, „Quick access recorder data analysis for windshear and turbulence studies“, J. Aircr., 47, 1443–1446 (2010). http://dx.doi.org/10.2514/1.46954

[33] R. Sharman, L. B. Cornman, G. Meymaris, J. Pearson, and T. Farrar, „Description and derived climatologies of automated in situ eddy-dissipation-rate reports of atmospheric turbulence“, J. Appl. Meteor. Climatol., 53, 1416–1432 (2014). http://dx.doi.org/10.1175/JAMC-D-13-0329.1

[34] L. Cornman, „Airborne In Situ Measurements of Turbulence“, Aviation Turbulence, pp. 97-120, (2016). http://dx.doi.org/10.1007/978-3-319-23630-8_5

[35] J. Pearson, R. Sharman, „Prediction of Energy Dissipation Rates for Aviation Turbulence. Part II: Nowcasting Convective and Nonconvective Turbulence“. Journal of Applied Meteorology and Climatology (2017). http://dx.doi.org/56. 10.1175/JAMC-D-16-0312.1

[36] J. H. Kim, R. D. Sharman, M. Strahan, J. W. Scheck, C. Bartholomew, J. C. Cheung, P. Buchanan, and N. Gait, „Improvements in nonconvective aviation turbulence prediction for the world area forecast system“, B. Am. Meteorol. Soc., 99, 2295–2311 (2018). https://doi.org/10.1175/BAMS-D-17-0117.1

[37] S. B. Trier, R. D. Sharman, and T. P. Lane, „Influences of Moist Convection on a Cold-Season Outbreak of Clear-Air Turbulence (CAT)“, Mon. Wea. Rev., 140, 2477–2496 (2012). https://doi.org/10.1175/MWR-D-11-00353.1

[38] Trier, S. B. and Sharman, R. D.: Trapped gravity waves and their association with turbulence in a large thunderstorm anvil during PECAN, Mon. Weather Rev., 146, 3031–3052 (2018). https://doi.org/10.1175/MWR-D-18-0152.1

[39] S. H. Kim, H. Y. Chun, J. H. Kim, R. D. Sharman, and M. Strahan, „Retrieval of eddy dissipation rate from derived equivalent vertical gust included in Aircraft Meteorological Data Relay (AMDAR)“, Atmos. Meas. Tech., 13, 1373–1385 (2020). https://doi.org/10.5194/amt-13-1373-2020

[40] Federal Aviation Administration website, Federal Aviation Administration (faa.gov)

[41] International Air Transport Association (IATA) website, IATA - Home

[42] B. W. Zeff, D. D. Lanterman, R. McAllister, R. Roy, E. J. Kostelich, D. P. Lathrop, „Measuring intense rotation and dissipation in turbulent flows“, Nature (2003) Jan 9;421(6919):146-9. https://doi.org/10.1038/nature01334

[43] Lundquist, J. K., and Coauthors, 2017: Assessing State-of-the-Art Capabilities for Probing the Atmospheric Boundary Layer: The XPIA Field Campaign. Bull. Amer. Meteor. Soc., 98, 289–314. https://doi.org/10.1175/BAMS-D-15-00151.1

[44] J. Reuder, L. Båserud, S. Kral, V. Kumer, J. W. Wagenaar, A. Knauer, „Proof of Concept for Wind Turbine Wake Investigations with the RPAS SUMO“, Energy Procedia, Volume 94, 2016, Pages 452-461, ISSN 1876-6102. https://doi.org/10.1016/j.egypro.2016.09.215

[45] B. D. Reineman, L. Lenain, N. M. Statom, and W. K. Melville, (2013) „Development and Testing of Instrumentation for UAV-Based Flux Measurements within Terrestrial and Marine Atmospheric Boundary Layers“, J. Atmos. Oceanic Technol., 30, 1295–1319. https://doi.org/10.1175/JTECH-D-12-00176.1

[46] B. D. Reineman, L. Lenain, and W. K. Melville, (2016) „The Use of Ship-Launched Fixed-Wing UAVs for Measuring the Marine Atmospheric Boundary Layer and Ocean Surface Processes“, J. Atmos. Oceanic Technol., 33, 2029–2052. https://doi.org/10.1175/JTECH-D-15-0019.1

[47] A. Rautenberg, J. Allgeier, S. Jung, J. Bange, „Calibration Procedure and Accuracy of Wind and Turbulence Measurements with Five-Hole Probes on Fixed-Wing Unmanned Aircraft in the Atmospheric Boundary Layer and Wind Turbine Wakes“, Atmosphere (2019), 10, 124. https://doi.org/10.3390/atmos10030124

[48] L. Båserud, J. Reuder, M.O. Jonassen, S.T. Kral, M. B. Paskyabi, M. Lothon, „Proof of concept for turbulence measurements with the RPAS SUMO during the BLLAST campaign“, Atmos. Meas. Tech. 2016, 9, 4901–4913. https://amt.copernicus.org/articles/9/4901/2016/

[49] A.P. Shelekhov, A. L. Afanasiev, E. A. Shelekhova, et al. „Using Small Unmanned Aerial Vehicles for Turbulence Measurements in the Atmosphere“, Izv. Atmos. Ocean. Phys. 57, 533–545 (2021). https://doi.org/10.1134/S0001433821050133

[50] H. Luce, L. Kantha, H. Hashiguchi, D. Lawrence, „Estimation of Turbulence Parameters in the Lower Troposphere from ShUREX (2016–2017) UAV Data“, Atmosphere (2019), 10, 384. https://doi.org/10.3390/atmos10070384

[51] J. O. Hinze (1975) Turbulence. McGraw-Hill, New York,

[52] L. P. Wang, S. Chen, J. G. Brasseur, J. C. Wyngaard, „Examination of hypotheses in the Kolmogorov refined turbulence theory through high-resolution simulations Part 1. Velocity field“, *Journal of Fluid Mechanics*. 1996;309:113-156. https://doi.org/10.1017/S0022112096001589

[53] G. I. Taylor, „The Spectrum of Turbulence“ (1938), Proc. R. Soc. Lond. A164476–490. http://doi.org/10.1098/rspa.1938.0032

[54] K. Sharp, R. Adrian, (2001), „PIV study of small-scale flow structure around a Rushton turbine“, AIChE J. 47, 766-778.

[55] K. Sharp, K.C. Kim, R. Adrian, (2000), „Dissipation estimation around a Rushton turbine using particle image velocimetry, Laser Techniques Applied to Fluid Mechanics“, Springer, pp. 337-354.

[56] R. A. Antonia, J. Kim, L.W. Browne, 2006. „Some characteristics of small-scale turbulence in a turbulent duct flow“, J. Fluid Mech. 233, 369-388.

[57] H. J. Hussein, S. P. Capp, W. K. George, „Velocity measurements in a high-Reynolds-number, momentum-conserving, axisymmetric, turbulent jet“, *Journal of Fluid Mechanics* (1994), 258:31-75. http://doi.org/10.1017/S002211209400323X

[58] D. Xu, J. Chen, „Accurate estimate of turbulent dissipation rate using PIV data, Experimental Thermal and Fluid Science“, Volume 44 (2013), Pages 662-672. https://doi.org/10.1016/j.expthermflusci.2012.09.006

[59] A. Ducci, M. Yianneskis, „Turbulence kinetic energy transport processes in the impeller stream of stirred vessels“, Chemical Engineering Science, Volume 61, Issue 9, Pages 2780-2790, (2006). https://doi.org/10.1016/j.ces.2005.09.020

[60] J. Sheng, H. Meng, R.O. Fox, „A large eddy PIV method for turbulence dissipation rate estimation“, Chemical Engineering Science, Volume 55, Issue 20, Pages 4423-4434 (2000). https://doi.org/10.1016/S0009-2509(00)00039-7

[61] A. Gabriele, A.W. Nienow, M.J.H. Simmons, „Use of angle resolved PIV to estimate local specific energy dissipation rates for up- and down-pumping pitched blade agitators in a stirred tank“, Chemical Engineering Science, Volume 64, Issue 1, Pages 126-143 (2009). https://doi.org/10.1016/j.ces.2008.09.018

[62] J. Meyers, P. Sagaut, “Is plane-channel flow a friendly case for the testing of large-eddy simulation subgrid-scale models?”, *Phys. Fluids* 19, 048105 (2007). https://doi.org/10.1063/1.2722422

[63] G. Bertens, D. van der Voort, H. Bocanegra Evans, W. van de Water, „Large-eddy estimate of the turbulent dissipation rate using PIV“, *Experiments in Fluids*, *56*, 89-1/9 (2015). https://doi.org/10.1007/s00348-015-1945-3

[64] G. K. Batchelor, „The theory of homogeneous turbulence“, Cambridge Monographs on Mechanics and Applied Mathematics. Cambridge University Press (1953), Pp. xi, 197; 28 Figs. 25s. Q.J.R. Meteorol. Soc., 79: 457-458. https://doi.org/10.1002/qj.49707934126

[65] H. Mouri, A. Hori, Y. Kawashima, K. Hashimoto, „Large-scale length that determines the mean rate of energy dissipation in turbulence“, American Physical Society, Phys. Rev. E (2012), Vol. 86. https://doi.org/10.1103/PhysRevE.86.026309

[66] J. Vassilicos, „Dissipation in Turbulent Flows“, Annual Review of Fluid Mechanics (2014), Vol. 47. https://doi.org/10.1146/annurev-fluid-010814-014637

[67] A. Kolmogorov, „Dissipation of energy in locally isotropic turbulence“ (1941a) *Dokl. Akad. Nauk. SSSR* 32:16–18.

[68] A. Kolmogorov, “ On degeneration (decay) of isotropic turbulence in an incompressible viscous fluid“ (1941b), *Dokl. Akad. Nauk, SSSR* 31:538–40.

[69] A. J. Puga, J. C. LaRue JC, „Normalized dissipation rate in a moderate Taylor Reynolds number flow“, *Journal of Fluid Mechanics* (2017). https://doi.org/10.1017/jfm.2017.47

[70] H. Tennekes, J. L. Lumley, „A First Course in Turbulence“, Cambridge, MIT Press (1972).

[71] R. Antonia, B. Pearson, „Reynolds Number Dependence of Velocity Structure Functions in a Turbulent Pipe Flow“, *Flow, Turbulence and Combustion* 64, 95–117 (2000). https://doi.org/10.1023/A:1009900120828

[72] W. J. T. Bos, R. and Rubinstein, “Dissipation in unsteady turbulence”, Physical Review Fluids, vol. 2, no. 2, Art. no. 022601, APS (2017). https://doi.org/10.1103/PhysRevFluids.2.022601

[73] W. J. T. Bos, L. Shao, J. P. Bertoglio, „Spectral imbalance and the normalized dissipation rate of turbulence“, Physics of Fluids, Vol. 19, no. 4 (2007). https://doi.org/10.1063/1.2714079

[74] B. R. Pearson, J. Cleve, M. Greiner, K. R. Sreenivasan, „Intermittency exponent of the turbulent energy cascade“, American Physical Society, Phys. Rev. E, Volume 69, Pages 6 (2004). https://doi.org/10.1103/PhysRevE.69.066316

[75] P.C. Valente, J. C. Vassilicos, J. C, „Universal Dissipation Scaling for Nonequilibrium Turbulence“, American Physical Society, Phys. Rev. Lett., Vol. 108, Issue 21, Pages 5 (2012). https://doi.org/10.1103/PhysRevLett.108.214503

[76] R. J. Hearst RJ, Lavoie P. Decay of turbulence generated by a square-fractal-element grid. *Journal of Fluid Mechanics*. 2014;741:567-584. doi:10.1017/jfm.2013.684

[77] J. C. Isaza, R. Salazar, Z. Warhaft, „On grid-generated turbulence in the near- and far field regions“. J. Fluid Mech (2014). 753, 402–426. https://doi.org/10.1017/jfm.2014.375

[78] K. Nagata, Y. Sakai, T. Inaba, H. Suzuki, O. Terashima, H. Suzuki, „Turbulence structure and turbulence kinetic energy transport in multiscale/fractal-generated turbulence“, *Physics of Fluids* (2013), 065102. https://doi.org/10.1063/1.4811402

[79] K. R. Sreenivasan, B. Dhruva, „Is there scaling in high-reynolds-number turbulence?“ *Progress of Theoretical Physics Supplement*, (130), 103-120, (1998). https://doi.org/10.1143/PTPS.130.103¨

[80] W. D. McComb, A. Berera, S. R. Yoffe, M. F. Linkmann, „Energy transfer and dissipation in forced isotropic turbulence“, American Physical Society, Phys. Rev. E, Vol. 91, Issue 4, (2015). https://doi.org/10.1103/PhysRevE.91.043013

[81] G. I. Taylor, „The Spectrum of Turbulence“, Proc. R. Soc. London (1938), A164476–490. https://doi.org/10.1098/rspa.1938.0032

[82] J. Costes, J.P. Couderc „Study by laser Doppler anemometry of turbulent flow induced by a Rushton turbine in a stirred tank: Influence of the Size of the Units: I. Mean Flow and Turbulence“, Chemical Engineering Science(1988) 43, 2751-2764. https://doi.org/10.1016/0009-2509(88)80018-6

[83] R. V. Calabrese, C.M. Stoots, “Flow in Impeller Region of a Stirred Tank”, Chem. Eng. Prog., 85, 43-50, May 1989.

[84] S. M. Kresta, P.E. Wood, „The flow field produced by a pitched blade turbine: Characterization of the turbulence and estimation of the dissipation rate“,Chemical Engineering Science 48(10), 1761-1774 (1993). https://doi.org/10.1016/0009-2509(93)80346-R

[85] H. Wu, G. K. Patterson, “Laser-Doppler measurements of turbulent-flow parameters in a stirred mixer”, *Chemical Engineering Science* 44 (1989): 2207-2221. https://doi.org/10.1016/0009-2509(89)85155-3

[86] H. Wu, G. K. Patterson, M. Van Doorn, „Distribution of turbulence energy dissipation rates in a Rushton turbine stirred mixer“, *Experiments in Fluids* 8, 153–160 (1989). https://doi.org/10.1007/BF00195789

[87] G. Zhou, S. M. Kresta, „Impact of tank geometry on the maximum turbulence energy dissipation rate for impellers“, AIChE J. (1996), 42: 2476 – 2490. https://doi.org/10.1002/aic.690420908

[88] M. Schäfer, M. Höfken, F. Durst, "Detailed LDV Measurements for Visualization of the Flow Field Within a Stirred-Tank Reactor Equipped with a Rushton Turbine", Chemical Engineering Research and Design, vol. 75, no. 8, pp. 729–736, (1997). https://doi.org/10.1205/026387697524399

[89] K. R. Sreenivasan, „On the universality of the Kolmogorov constant", *Physics of Fluids* (1995); 7 (11): 2778–2784. https://doi.org/10.1063/1.868656

[90] J. de Jong, L. Cao, S. H. Woodward, J. P. L. C. Salazar, L. R. Collins, H. Meng, "Dissipation rate estimation from PIV in zero-mean isotropic turbulence", Experiments in Fluids, vol. 46, no. 3, Springer, pp. 499–515, 2009. https://doi.org/10.1007/s00348-008-0576-3

[91] S. B. Pope, "Turbulent Flows", Cambridge University Press (2000), ISBN 0 521 59125 2. Turbulent Flows (elmoukrie.com)

[92] S. Liu, C. Meneveau, J. Katz, „On the properties of similarity subgrid-scale models as deduced from measurements in a turbulent jet", *Journal of Fluid Mechanics*, (1994), 275:83-119. https://doi.org/10.1017/S0022112094002296

[93] W. Hwang, J. K. and Eaton, "Creating homogeneous and isotropic turbulence without a mean flow", Experiments in Fluids, vol. 36, no. 3, Springer, pp. 444–454, (2004). https://doi.org/10.1007/s00348-003-0742-6

[94] R. S. Azad, S. Z. Kassab, „New method of obtaining dissipation", Experiments in Fluids 7, 81–87 (1989). https://doi.org/10.1007/BF00207299

[95] R. Escudié, A. Liné, "Experimental analysis of hydrodynamics in a radially agitated tank," Aiche Journal 49 (2002): 585-603. https://doi.org/10.1002/aic.690490306

[96] F. Khan, et al, "Angle-resolved stereo-PIV measurements close to a down-pumping pitched-blade turbine," *Chemical Engineering Science* 61 (2006): 2799-2806. https://doi.org/10.1016/j.ces.2005.10.067

[97] P. C. Kalverla, G. Duine, G. Steeneveld, T. Hedde, „Evaluation of the Weather Research and Forecasting Model in the Durance Valley Complex Terrain during the KASCADE Field Campaign", *J. Appl. Meteor. Climatol. (2016)*, **55**, 861–882, https://doi.org/10.1175/JAMC-D-15-0258.1

[98] M. Lehner, C. D. Whiteman, S. W. Hoch, D. Jensen, E. R. Pardyjak, L. S. Leo, S. Di Sabatino, H. J. S. Fernando, "A Case Study of the Nocturnal Boundary Layer Evolution on a Slope at the Foot of a Desert Mountain", *Journal of Applied Meteorology and Climatology* 54.4 (2015): 732-751. https://doi.org/10.1175/JAMC-D-14-0223.1

[99] A. an den Kroonenberg, T. Martin, M. Buschmann, J. Bange, J., P. Vörsmann, „Measuring the Wind Vector Using the Autonomous Mini Aerial Vehicle M2AV", *Journal of Atmospheric and Oceanic Technology (2018)*, *25*(11), 1969-1982. https://doi.org/10.1175/2008JTECHA1114.1

[100] J. Reuder et al., "The Small Unmanned Meteorological Observer SUMO: A new tool for atmospheric boundary layer research", *Meteorologische Zeitschrift* 18 (2009): 141-147. https://doi.org/10.1088/1755-1315/1/1/012014

[101] S. Martin, J. Bange, F. Beyrich, „Meteorological profiling of the lower troposphere using the research UAV - M^{2}AV Carolo", Atmos. Meas. Tech. (2011), 4, 705–716. https://doi.org/10.5194/amt-4-705-2011

[102] R. T. Palomaki, N. T. Rose, M. van den Bossche, T. J. Sherman, S. F. J. De Wekker, S. F. J. , „Wind Estimation in the Lower Atmosphere Using Multirotor

Aircraft“. Journal of Atmospheric and Oceanic Technology (2017), 34(5), 1183-1191. https://doi.org/10.1175/JTECH-D-16-0177.1

[103] B. Arain, F. Kendoul, "Real-time wind speed estimation and compensation for improved flight," in *IEEE Transactions on Aerospace and Electronic Systems*, vol. 50, no. 2, pp. 1599-1606 (2014). https://doi.org/10.1109/TAES.2014.120236

[104] P. Abichandani, D. Lobo, G. Ford, D. Bucci and M. Kam, "Wind Measurement and Simulation Techniques in Multi-Rotor Small Unmanned Aerial Vehicles," in *IEEE Access*, vol. 8, pp. 54910-54927 (2020). https://doi.org/10.1109/ACCESS.2020.2977693

[105] G. de Boer, S. Borenstein, R. Calmer, C. Cox, M. Rhodes, C. Choate, J. Hamilton, J. Osborn, D. Lawrence, B. Argrow, J. Intrieri, „Measurements from the University of Colorado RAAVEN Uncrewed Aircraft System during ATOMIC“, Earth Syst. Sci. Data (2022), 14, 19–31, https://doi.org/10.5194/essd-14-19-2022

[106] S. Prudden, A. Fisher, M. Marino, A. Mohamed, S. Watkins, G. Wild, “Measuring wind with Small Unmanned Aircraft Systems”, Journal of Wind Engineering and Industrial Aerodynamics (2018), Volume 176,Pages 197-210, ISSN 0167-6105. https://doi.org/10.1016/j.jweia.2018.03.029

[107] P. Abichandani, D. Lobo, G. Ford, D. Bucci and M. Kam, "Wind Measurement and Simulation Techniques in Multi-Rotor Small Unmanned Aerial Vehicles," in *IEEE Access*, vol. 8, pp. 54910-54927, 2020. https://doi.org/10.1109/ACCESS.2020.2977693

[108] Unites States Patent, Kapartis, Patent number: 5 877 416, Date of patent: Mar. 2, 1999, Assignee: FT Technologies Limited. 1498423803573252529-05877416 (diliev.com)

[109] K. A. Adkins, C. J. Swinford, P.D. Wambolt, G. Bease, G., „Development of a sensor suite for atmospheric boundary layer measurement with a small multirotor unmanned aerial system“, *International Journal of Aviation, Aeronautics (2020), and Aerospace, 7*(1). https://doi.org/10.15394/ijaaa.2020.1433

[110] T. Shimura, M. Inoue, H. Tsujimoto, K. Sasaki, M. Iguchi, „Estimation of Wind Vector Profile Using a Hexarotor Unmanned Aerial Vehicle and Its Application to Meteorological Observation up to 1000 m above Surface“, *Journal of Atmospheric and Oceanic Technology (2018)*, *35*(8), 1621-1631. https://doi.org/10.1175/JTECH-D-17-0186.1

[111] FT Technologies, Website: Acu-Res® Technology - FT Technologies

[112] M. L. Aitken, M. E. Rhodes, J. K. Lundquist,“ Performance of a Wind-Profiling Lidar in the Region of Wind Turbine Rotor Disks“, Journal of Atmospheric and Oceanic Technology (2012), 29(3), 347-355. https://doi.org/10.1175/JTECH-D-11-00033.1

[113] Campbell Scientific, CSAT3B, website: CSAT3: 3-D Sonic Anemometer (campbellsci.com)

[114] J. E. Cermak, J. D. Horn (1968), „Tower shadow effect“, J. Geophys. Res., 73(6), 1869–1876. https://doi.org/10.1029/JB073i006p01869

[115] C. Russell, al. “Wind Tunnel and Hover Performance Test Results for Multicopter UAS Vehicles.” (2016). rotorcraft.arc.nasa.gov/Publications/files/Russell_1180_Final_TM_022218.pdf

[116] M. Bruse, H. Fleer, "Simulating surface–plant–air interactions inside urban environments with a three dimensional numerical model", Environmental Modelling & Software, Volume 13, Issues 3–4, 1998, Pages 373-384, ISSN 1364-8152. https://doi.org/10.1016/S1364-8152(98)00042-5

[117] Simon, H.; Heusinger, J.; Sinsel, T.; Weber, S.; Bruse, M., "Implementation of a Lagrangian Stochastic Particle Trajectory Model (LaStTraM) to Simulate Concentration and Flux Footprints Using the Microclimate Model ENVI-Met", Atmosphere (2021), 12,977. https://doi.org/10.3390/atmos12080977

[118] Fabbri, K.; Costanzo, V. Drone-assisted infrared thermography for calibration of outdoor microclimate simulation models. Sustain. Cities Soc. 2020, 52, 101855. https://doi.org/10.1016/j.scs.2019.101855

[119] J. Patrikar, B. Moon, S. Scherer, (2020). "Wind and the City: Utilizing UAV-Based In-Situ Measurements for Estimating Urban Wind Fields", 1254-1260. https://doi.org/10.1109/IROS45743.2020.9340812

[120] D. Galway, J. Etele, G. Fusina, (2011), "Modeling of Urban Wind Field Effects on Unmanned Rotorcraft Flight". Journal of Aircraft. 48. 1613-1620. https://doi.org/10.2514/1.C031325

[121] S. Giersch, O. E. Guernaoui, S. Raasch, M. Sauer, M. Palomar, "Atmospheric flow simulation strategies to assess turbulent wind conditions for safe drone operations in urban environments", Journal of Wind Engineering and Industrial Aerodynamics, Volume 229, 2022, 105136, ISSN 0167-6105, https://doi.org/10.1016/j.jweia.2022.105136

[122] A. Mohamed, M. Marino, S. Watkins, J. Jaworski, A. Jones, "Gusts Encountered by Flying Vehicles in Proximity to Buildings", Drones 2023, 7, 22. https://doi.org/10.3390/drones7010022

[123] R. Balážová, S. Ferrari, J. Hlinka, A. Santus A., "Turbulence estimation by eddy dissipation rate at low-altitudes using UAV in-situ data" (2024), ENGINEERING MECHANICS 2024, pages 42 – 45. https://doi.org/10.21495/em2024-042

[124] J. Kim, R. D. harman, "Characteristics of Energy Dissipation Rate Observed from the High-Frequency Sonic Anemometer" at Boseong, South Korea. Atmosphere 2021, 12, 837. https://doi.org/10.3390/atmos12070837

[125] G. Hellmann, „Über die Bewegung der Luft in den untersten Schichten der Atmosphare", Kgl. Akademie der Wissenschaften, Reimer, 1914.

[126] Liu, J., Gao, C. Y., Ren, J., Gao, Z., Liang, H., and Wang, L.: Wind resource potential assessment using a long term tower measurement approach: A case study of Beijing in China. Journal of cleaner production, 174, 917-926, 2018.

[127]
N. Aghbalou, A. Charki, S.R. Elazzouzi, K. Reklaoui, "A probabilistic assessment approach for wind turbine-site matching", International Journal of Electrical Power & Energy Systems, Volume 103, 2018, Pages 497-510, ISSN 0142-0615. https://doi.org/10.1016/j.ijepes.2018.06.018

List Of Figures

Figure 1: Consortium of testing flights in Rzeszow 20
Figure 2: Drone in the box by DroneHub used for testing. 21
Figure 3: Honeywell SC-Modem (black box with fan) and sensors case included two meteorological sensors (white box on drone leg). 21
Figure 4: Reference points (highlighted in yellow) and flight path of the Beyond Visual Line of Sight mode testing flights. 23
Figure 5: EDR reporting coverage with limited airline participation, source: [41] 31
Figure 6: Comprehensive EDR reporting coverage, source: [41] 31
Figure 7: Pitot-static tube principle 50
Figure 8: Cobra probe, Source: [106] 51
Figure 9: Working principle of ToF Ultrasonic anemometer [Source: DOI: 10.1109/ACCESS.2020.2977693] 51
Figure 10: Acu-Res Working principle [Source: 111] 52
Figure 11: Basic simulation geometry including integrated quadcopter 57
Figure 12: Detailed view of the integrated unmanned aerial vehicle. 57
Figure 13: STAR-CCM+ Mesh Scene 58
Figure 14: Set of input physical models 58
Figure 15: Detailed shot capturing the ground effect (wind speed 10 m/s, wind direction 270°) 59
Figure 16: Eddy current dissipation rate (wind speed 10 m/s, wind direction 270°) 60
Figure 17: A close-up shot showing the eddy currents around two consecutive obstacles (wind speed 10 m/s and wind direction 270°) 60
Figure 18: Indoor hover test – 17 test modes and their corresponding wind speeds 62
Figure 19: Indoor hover test – Siemens propeller wind generator 62
Figure 20: Indoor hover test - Parameters monitored to understand UAV behaviour 64
Figure 21: Approved locations for UAV operation within the BUT campus 65
Figure 22: UAV flight trajectory (red colour) within BUT Campus 66
Figure 23: Basic analysis of UAV manoeuvrability and stability during testing flight 67
Figure 24: Preliminary concept of hover test with Davis meteorological station 68
Figure 25: example of the velocity field in a vertical section in the centre of a single building, obtained as output of numerical simulation for a 10 m x 10 m x 20 m building with a 10 m/s wind speed; below, a zoom close to the building to highlight the dangerous 73
Figure 26: Graphical representation demonstrating the correlation between building height, wind velocity, and the extent of the hazardous zone – downstream wake zone. 74
Figure 27: Graphical representation demonstrating the correlation between building height, wind velocity, and the extent of the hazardous zone – vertical updraft zone. 76
Figure 28: Meteomatics historical data, coordinates information (49°14'06.6"N 16°34'18.1"E) 77
Figure 29: Summary of Meteomatics historical data 78
Figure 30: Wind rose April 2020 – 2023 (Time window from 09:00 a.m. to 03:00 p.m.) 78

Figure 31: Wind rose (2011 - 2022) [source: ČHMÚ] 80
Figure 32: Max wind speed 2000 – 2022 (April average) 80
Figure 33: Average temperature (April average) 81
Figure 34: Relative humidity (April average) 81
Figure 35: Barometric pressure (April average) 82
Figure 36: AdMaS centre and surroundings 83
Figure 37: Medlanecky hill profile 83
Figure 38:2D DTM AdMaS Centre 84
Figure 39:3D DTM AdMaS Centre 85
Figure 40: Visualization of the 3d simulated domain 86
Figure 41: wind velocity field in a horizontal plane close to the terrain level (9,5 m above the ground) at 12:00, extracted as an output of the ENVI-met numerical simulation of AdMaS centre with starting wind speed 4 m/s; wind comes from above. 87
Figure 42: wind velocity field in a vertical plane taken in the middle of the building H width at 12:00, extracted as an output of the ENVI-met numerical simulation of AdMaS centre with starting wind speed 4 m/s; wind comes from the right. 87
Figure 43: Calypso sonic anemometer located in the wind tunnel during verification tests. . 90
Figure 44: Dependency between time (horizontal axis) and wind speed (vertical axis) clearly shows low measurement precision below 3 m/s, but sufficient precision above. 91
Figure 45: the DJI M100 UAS fitted with two Calypso anemometers during the initial flight tests. 92
Figure 46: ground-based reference, meteorological station Davis Vantage Pro2 during UAS test flight. 93
Figure 47: The comparison of the data from the ground-based reference and the anemometer onboard UAS in flight. 93
Figure 48: Brno - AdMaS Centre 94
Figure 49: AdMaS measurement grid of points 95
Figure 50: Photos from demonstration mission AdMaS 95
Figure 51: Position of Davis meteorological station 97
Figure 52: Comparison of wind speed decrease (ENVI-met Single building scenario compared to UAV real-time data) 102
Figure 53: Comparison of wind speed decrease (ENVI-met AdMaS scenario compared to UAV real-time data) 103
Figure 54: EDR results compared to Velocity fluctuations 108

List Of Tables

Table 1: Prioritized ranking of Specific Weather Information Gaps [source: MIT Lincoln Laboratory, ATC-437, page 72] 15
Table 2: List of Weather Research Recommendations to Address Information Gaps [source: MIT Lincoln Laboratory, ATC-438, page 15] 16
Table 3: Temperature deviations (Baro sensor) 25
Table 4: Temperature deviations (OW_Therm sensor) 25
Table 5: Barometric pressure deviations (Baro sensor) 25
Table 6: Types of Atmospheric Turbulence 27
Table 7: Summary of current usage of EDR algorithms 33
Table 8: Advantages and disadvantages of different techniques for measuring wind characteristics 53
Table 9: Brief summary of UAV mission using ultrasonic anemometer 54
Table 10: Accuracy of various ultrasonic anemometers 55
Table 11: Solver Settings of the Case Study Processed in STAR-CCM+ Software 59
Table 12: Summary of all testing domains (ENVI-met, Single building scenario) 72
Table 13: Average values of basic parameters (Meteomatics data) 79
Table 14: ČHMÚ historical data 79
Table 15: Comparison of calculated (via eq. 1 and 2) and measured (on the numerical simulations of the AdMaS centre) danger zone sizes 87
Table 16: Results of the sonic anemometer accuracy verification tests, using a wind tunnel venturi tube as reference. 90
Table 17: List of testing points 96
Table 18: Testing flights (altitude = ½ building height) 96
Table 19: Testing flights (altitude = building height) 96
Table 20: Wind shear exponent in various are types 98
Table 21: Testing flights (altitude = ½ building height) and used PLM 98
Table 22: Testing flights (altitude = building height) and used PLM 98
Table 23: Quantitative Assessment of Wind Speed Reduction in the Vicinity of Building H (altitude = ½ building height) 99
Table 24: Quantitative Assessment of Wind Speed Reduction in the Vicinity of Building H (altitude = building height) 99
Table 25: Percentage Decrease in Wind Speed at Measurement Points: In-Situ Observations 100
Table 26: Decrease in Wind Speed, altitude = ½ building height (ENVI-met simulation, Single-building scenario) 101
Table 27: Percentage Decrease in Wind Speed, altitude = building height (ENVI-met simulation, Single-building scenario) 101
Table 28: Decrease in Wind Speed, altitude = ½ building height (ENVI-met simulation, AdMaS scenario) 102
Table 29: Percentage Decrease in Wind Speed, altitude = building height (ENVI-met simulation, AdMaS scenario) 103

Table 30: Percentage deviation between Output of Numerical simulation ENVI-met AdMaS scenario and UAV real-time data 103
Table 31: Summary of all 60 tests and the result of EDR calculation 106
Table 32: Objectives of the dissertation. 112

ACRONYMS

ACMS	Aircraft Condition Monitoring System
AGL	Above Ground Level
AIM	Air Information Management
AIRMET	Airmen's Meteorological Information
AMDAR	Air Defence Maritime
AWRP	Aviation Weather Research Program
BH	Building height
BUT	Brno University of Technology
BVLOS	Beyond Visual Line of Sight
CAA	Civil Aviation Authority
CAT	Clear Air Turbulence
CBLT	Convective Boundary Layer Turbulence
CFD	computational fluid dynamics
ČHMU	Český hydrometeorologický ústav
DEVG	Derived Equivalent Vertical Gust
DHS	Department of Homeland Security
DNS	direct numerical simulations
DOD	Department of Defence
DW	downstream wake
EC	European Commission
ECMWF-if	European Centre for Medium-Range Weather Forecasts - Integrated Forecasting System
EDR	Eddy Dissipation Rate
EFB	Electronic Flight Bag
FAA	Federal Aviation Administration
GAMET	General Area Meteorological Forecast
GPS	Global Positioning System
GTG	Global Turbulence Guidance
GTGN	Global Turbulence Guidance Nowcast
IATA	International Air Transport Association
ICAO	International Civil Aviation Organization
ITSAT	Inmarsat T-SAT
L	Length
LB	Left Back
LF	Left Front
LLT	Low-Level Terrain-Induced Turbulence
LKAA	ICAO code for Karlovy Vary Airport
LTE	Long-Term Evolution
MAVLink	Micro Air Vehicle Link
METAR	Meteorological Aerodrome Report
MHPP	Multi-hole pressure probes
MIT	Massachusetts Institute of Technology
MQTT	Message Queuing Telemetry Transport

NOAA	National Oceanic and Atmospheric Administration
NAS	National Airspace System
NASA	National Aeronautics and Space Administration
NY	New York
NCAR	National Centre for Atmospheric Research
NTDA	NCAR Turbulence Detection Algorithm
NWS	National Weather Service
OLM	Odbor letecké meteorologie
PIREPs	Pilot Reports
RB	Right Back
Re	Reynolds number
RF	Right Front
RPM	Revolutions Per Minute
RTCA	Radio Technical Commission for Aeronautics
Rx	Receiver
SHMU	Slovenský hydrometeorologický ústav
SIGMET	Significant Meteorological Information
SUMO	Small Unmanned Meteorological Observer
TAF	Terminal Aerodrome Forecast
TKE	turbulence kinetic energy
TOF	Time-of-Flight
Tx	Transducer
UAS	Unmanned Aerial System
UAV	Unmanned aerial vehicle
UK	United Kingdom
USA	United States of America
UTC	Coordinated Universal Time
VLL	Very Low Levels
VOC	Voice of the Customer
V_{REF}	Reference Wind Speed
VU	Vertical updrafts
VUT	Vysoké učení technické v Brně
WMO	World Meteorological Organization
WTIC	Weather Technology in the Cockpit

APPENDIX

APPENDIX I. AdMaS Meteorological data
APPENDIX II. AdMaS Preflight preparation
APPENDIX III. ENVI-met Output
APPENDIX IV. Voice of the Customer
APPENDIX V. Publications